Nuclear Instruments and Methods in Physics Research A 386 (1997) 348–396

ELSEVIER

NUCLEAR INSTRUMENTS & METHODS IN PHYSICS RESEARCH Section A

The tracking, calorimeter and muon detectors of the H1 experiment at HERA

H1 Collaboration

I. Abt[h], T. Ahmed[d], S. Aid[n], V. Andreev[z], B. Andrieu[ac], R.-D. Appuhn[ℓ], C. Arnault[ab], M. Arpagaus[ak], A. Babaev[y], H. Bärwolff[aj], J. Bán[r], E. Banas[g,ℓ], P. Baranov[z], E. Barrelet[ad], W. Bartel[ℓ], M. Barth[e], U. Bassler[ad], F. Basti[ag], D.E. Baynham[f], J.-M. Baze[j], G.A. Beck[u], H.P. Beck[aℓ], D. Bederede[j], H.-J. Behrend[ℓ], C. Beigbeder[ab], A. Belousov[z], Ch. Berger[a], H. Bergstein[a], R. Bernard[j], G. Bernardi[ad], R. Bernet[ak], R. Bernier[ab], U. Berthon[ac], G. Bertrand-Coremans[e], M. Besançon[j], R. Beyer[ℓ], J.-C. Biasci[ab], P. Biddulph[w], V. Bidoli[ag], E. Binder[ℓ], P. Binko[ℓ], J.-C. Bizot[ab], V. Blobel[n], F. Blouzon[ad], H. Blume[aa], K. Borras[i], V. Boudry[ac], C. Bourdarios[ab], F. Brasse[ℓ], W. Braunschweig[a], D. Breton[ab], H. Brettel[aa], V. Brisson[ab], D. Bruncko[r], C. Brune[p], U. Buchner[i], L. Büngener[n], J. Bürger[ℓ], F.W. Büsser[n], A. Buniatian[ℓ,1], S. Burke[t], P. Burmeister[ℓ], A. Busata[ac], G. Buschhorn[aa], A.J. Campbell[k], T. Carli[aa], F. Charles[ad], M. Charlet[ℓ], R. Chase[ab], D. Clarke[f], A.B. Clegg[s], M. Colombo[i], V. Commichau[b], J.F. Connolly[f], U. Cornett[ℓ], J.A. Coughlan[f], A. Courau[ab], M.-C. Cousinou[x], Ch. Coutures[j], A. Coville[aa], G. Cozzika[j,*], D.A. Cragg[f], L. Criegee[ℓ], H.I. Cronström[v], N.H. Cunliffe[f], J. Cvach[ac], A. Cyz[g], S. Dagoret[ad], J.B. Dainton[t], M. Danilov[y], A.W.E. Dann[w], D. Darvill[b], W.D. Dau[q], J. David[ad], M. David[j], R.J. Day[f], E. Deffur[ℓ], B. Delcourt[ab], L. Del Buono[ad], F. Descamps[ad], M. Devel[ab], J. P. Dewulf[e], A. De Roeck[ℓ], P. Dingus[ac], K. Djidi[j], C. Dollfus[aℓ], J.D. Dowell[d], H.B. Dreis[b], A. Drescher[i], U. Dretzler[i], J. Duboc[ad], A. Ducorps[ab], D. Düllmann[n], O. Dünger[n], H. Duhm[m,†], B. Dulny[aa], F. Dupont[ab], R. Ebbinghaus[i], M. Eberle[m], J. Ebert[ai], T.R. Ebert[t], G. Eckerlin[ℓ], B.W.H. Edwards[f], V. Efremenko[y], S. Egli[aℓ], S. Eichenberger[aℓ], R. Eichler[ak], F. Eisele[o], E. Eisenhandler[u], N.N. Ellis[d], R.J. Ellison[w], E. Elsen[ℓ], A. Epifantsev[y], M. Erdmann[o], W. Erdmann[ak], G. Ernst[i], E. Evrard[e], G. Falley[ℓ], L. Favart[e], A. Fedotov[y], D. Feeken[n], R. Felst[ℓ], J. Feltesse[j], Z.Y. Feng[ad], I.F. Fensome[d], J. Fent[aa], J. Ferencei[ℓ], F. Ferrarotto[ag], K. Finke[ℓ], K. Flamm[ℓ], W. Flauger[ℓ,†], M. Fleischer[ℓ], M. Flieser[aa], P.S. Flower[f], G. Flügge[b], A. Fomenko[z], B. Fominykh[y], M. Forbush[h], J. Formánek[af], J.M. Foster[w], G. Franke[ℓ], E. Fretwurst[m], W. Fröchtenicht[aa], P. Fuhrmann[a], E. Gabathuler[t], K. Gabathuler[ah], K. Gadow[ℓ], K. Gamerdinger[aa], J. Garvey[d], J. Gayler[ℓ], E. Gažo[ℓ], A. Gellrich[n], M. Gennis[ℓ], U. Gensch[aj], H. Genzel[a], R. Gerhards[ℓ], K. Geske[n], I. Giesgen[b], D. Gillespie[t], W. Glasgow[f], L. Godfrey[h], J. Godlewski[g], U. Goerlach[ℓ], L. Goerlich[g], N. Gogitidze[z], M. Goldberg[ad], A.M. Goodall[t], I. Gorelov[y], P. Goritchev[y], L. Gosset[j], C. Grab[ak], H. Grässler[b], R. Grässler[b], T. Greenshaw[t], C. Gregory[ac], H. Greif[aa], M. Grewe[i], G. Grindhammer[aa], A. Gruber[aa], C. Gruber[q], S. Günther[aj], J. Haack[aj], M. Haguenauer[ac], D. Haidt[ℓ], L. Hajduk[g], D. Hammer[ℓ], O. Hamon[ad], M. Hampel[a],

PII S0168-9002(96)00894-7

D. Handschuh[ℓ], K. Hangarter[b], E.M. Hanlon[s], M. Hapke[ℓ], U. Harder[aj], J. Harjes[ℓ], P. Hartz[i], P.E. Hatton[f], R. Haydar[ab], W.J. Haynes[f], J. Heatherington[u], V. Hedberg[v], C.R. Hedgecock[f], G. Heinzelmann[n], R.C.W. Henderson[s], H. Henschel[aj], R. Herma[a], I. Herynek[ae], W. Hildesheim[m,ad], P. Hill[ℓ], D.L. Hill[f], C.D. Hilton[w], J. Hladký[ae], K.C. Hoeger[w], R.B. Hopes[f], R. Horisberger[ah], A. Hrisoho[ab], J. Huber[aa], Ph. Huet[e], H. Hufnagel[o], N. Huot[ad], J.-F. Huppert[ad], M. Ibbotson[w], D. Imbault[ad], H. Itterbeck[a], M.-A. Jabiol[j], A. Jacholkowska[ab], C. Jacobsson[v], M. Jaffré[ab], J. Janoth[p], T. Jansen[ℓ], P. Jean[ab], J. Jeanjean[ab], L. Jönsson[v], K. Johannsen[n], D.P. Johnson[e], L. Johnson[s], P. Jovanovic[d], H. Jung[b], P.I.P. Kalmus[u], D. Kant[u], G. Kantel[ℓ], S. Karstensen[f,ℓ], S. Kasarian[ℓ], R. Kaschowitz[b], P. Kasselmann[m], U. Kathage[q], H.H. Kaufmann[aj], G. Kemmerling[b], I.R. Kenyon[d], S. Kermiche[x], C. Keuker[a], C. Kiesling[aa], M. Klein[aj], C. Kleinwort[n], G. Knies[ℓ], W. Ko[h], T. Kobler[aa], J. Koch[m], T. Köhler[a], J. Köhne[aa], M. Kolander[i], H. Kolanoski[c], F. Kole[h], J. Koll[ℓ], S.D. Kolya[w], B. Koppitz[n], V. Korbel[ℓ], M. Korn[i], P. Kostka[aj], S.K. Kotelnikov[z], M.W. Krasny[g,ad], H. Krehbiel[ℓ], F. Krivan[r], D. Krücker[b], U. Krüger[ℓ], U. Krüner-Marquis[ℓ], M. Kubantsev[y], J.P. Kubenka[aa], T. Külper[ℓ], H.-J. Küsel[ℓ], H. Küster[b], M. Kuhlen[aa], T. Kurča[r], J. Kurzhöfer[i], B. Kuznik[ai], B. Laforge[j], F. Lamarche[ac], R. Lander[h], M.P.J. Landon[u], W. Lange[ℓ], W. Lange[aj], R. Langkau[m], P. Lanius[aa], J.-F. Laporte[j], L. Laptin[y], H. Laskus[aa], A. Lebedev[z], M. Lemler[g,ℓ], U. Lenhardt[i], A. Leuschner[ℓ], C. Leverenz[ℓ], S. Levonian[ℓ,z], D. Lewin[ℓ], Ch. Ley[b], A. Lindner[i], G. Lindström[m], F. Linsel[ℓ], J. Lipinski[n], B. Liss[ℓ], P. Loch[ℓ], A.B. Lodge[f], H. Lohmander[v], G.C. Lopez[u], J.-P. Lottin[j], V. Lubimov[y], K. Ludwig[ℓ], D. Lüers[aa,†], N. Lugetski[y], B. Lundberg[v], K. Maeshima[h], N. Magnussen[ai], E. Malinovski[z], S. Mani[h], P. Marage[e], J. Marks[x], R. Marshall[w], J. Martens[ai], F. Martin[ad], G. Martin[ab], R. Martin[t], H.-U. Martyn[a], J. Martyniak[g], V. Masbender[ℓ], S. Masson[b], A. Mavroidis[u], S.J. Maxfield[t], S.J. McMahon[t], A. Mehta[w], K. Meier[p], J. Meissner[aj], D. Mercer[w], T. Merz[ℓ], C.A. Meyer[a,ℓ], H. Meyer[ai], J. Meyer[ℓ], S. Mikocki[g,ab], J.L. Mills[f], V. Milone[ag,†], J. Möck[aa], E. Monnier[ad], B. Montés[ac], F. Moreau[ac], J. Moreels[e], B. Morgan[u], J.V. Morris[f], J.M. Morton[t], K. Müller[a,ℓ], P. Murín[r], S.A. Murray[w], V. Nagovizin[y], B. Naroska[n], Th. Naumann[aj], P. Nayman[ad], A. Nepeipivo[y], P. Newman[d], D. Newman-Coburn[u], D. Newton[s], D. Neyret[ad], H.K. Nguyen[ad], F. Niebergall[n], C. Niebuhr[ℓ], R. Nisius[a], T. Novák[ae], H. Nováková[ae], G. Nowak[g], G.W. Noyes[f], M. Nyberg[v], H. Oberlack[aa], U. Obrock[i], J.E. Olsson[ℓ], J. Olszowska[g,ℓ], S. Orenstein[ac], F. Ould-Saada[n], P. Pailler[j], S. Palanque[j], E. Panaro[ℓ], A. Panitch[e], J.-Y. Parey[ac], C. Pascaud[ab], G.D. Patel[t], A. Patoux[j], C. Paulot[ab], U. Pein[m], E. Peppel[ℓ], E. Perez[j], P. Perrodo[ac], A. Perus[ab], S. Peters[aa], J.-P. Pharabod[ac], H.T. Phillips[d], J.P. Phillips[w], Ch. Pichler[m], A. Pieuchot[x], W. Pimpl[aa], D. Pitzl[ak], A. Porrovecchio[ag], S. Prell[ℓ], R. Prosi[ℓ], H. Quehl[ℓ], G. Rädel[ℓ], F. Raupach[a], K. Rauschnabel[i], A. Reboux[ab], P. Reimer[ae], G. Reinmuth[ab], S. Reinshagen[ℓ], P. Ribarics[aa], V. Riech[m], J. Riedlberger[ak], H. Riege[n], S. Riess[n], M. Rietz[b], S.M. Robertson[d], P. Robmann[a,ℓ], P. Röpnack[ℓ], R. Roosen[e], K. Rosenbauer[a], A. Rostovtsev[y], C. Royon[j], A. Rudge[h], K. Rüter[aa], M. Rudowicz[aa], M. Ruffer[m], S. Rusakov[z], V. Rusinov[y], K. Rybicki[g], J. Sacton[e], N. Sahlmann[b], E. Sanchez[aa], D.P.C. Sankey[f], M. Savitski[ℓ,y], P. Schacht[aa], S. Schiek[n], N. Schirm[m], S. Schleif[p], P. Schleper[o], W. von Schlippe[u], C. Schmidt[ℓ], D. Schmidt[ai], G. Schmidt[n], W. Schmitz[b], H. Schmücker[aa], V. Schröder[ℓ],

J. Schütt[n], E. Schuhmann[aa], M. Schulz[ℓ], A. Schwind[aj], W. Scobel[m], U. Seehausen[n], F. Sefkow[ℓ], R. Sell[ℓ], M. Seman[r], A. Semenov[y], P. Shatalov[y], V. Shekelyan[y], I. Sheviakov[z], H. Shooshtari[ag], L.N. Shtarkov[z], G. Siegmon[q], U. Siewert[q], Y. Sirois[ac], A. Sirous[ℓ], I.O. Skillicorn[k], P. Škvařil[ae], P. Smirnov[z], J.R. Smith[h], L. Smolik[ℓ], D. Sole[f], Y. Soloviev[z], J. Špalek[r], H. Spitzer[n], R. von Staa[n], J. Staeck[b], P. Staroba[ae], J. Šťastný[ae], M. Steenbock[n], P. Štefan[r], P. Steffen[ℓ], R. Steinberg[b], H. Steiner[ad], B. Stella[ag], K. Stephens[w], J. Stier[ℓ], J. Stiewe[p], U. Stösslein[aj], J. Strachota[ℓ], U. Straumann[aℓ], A. Strowbridge[f], W. Struczinski[b], J.P. Sutton[d], Z. Szkutnik[ℓ], G. Tappern[f], S. Tapprogge[p], R.E. Taylor[ab,am], V. Tchernyshov[y], V. Tchudakov[y], C. Thiebaux[ac], K. Thiele[ℓ], G. Thompson[u], R.J. Thompson[w], I. Tichomirov[y], C. Trenkel[q], W. Tribanek[aa], K. Tröger[ℓ], P. Truöl[aℓ], M. Turiot[ad], J. Turnau[g], J. Tutas[o], L. Urban[aa], M. Urban[ac], A. Usik[z], Š. Valkár[af], A. Valkárová[af], C. Vallée[x], G. Van Beek[e], M. Vanderkelen[e], L. Van Lancker[e], P. Van Mechelen[e], A. Vartapetian[ℓ,1], Y. Vazdik[z], M. Vecko[ae], P. Verrecchia[j], R. Vick[n], G. Villet[j], E. Vogel[a], K. Wacker[i], M. Wagener[ah], I.W. Walker[s], A. Walther[i], G. Weber[n], D. Wegener[i], A. Wegner[aa], P. Weissbach[aa], H. P.Wellisch[aa], L. West[d], D. White[f], S. Willard[h], M. Winde[aj], G.-G. Winter[ℓ], Th. Wolff[ak], L.A. Womersley[t], A.E. Wright[w], E. Wünsch[ℓ], N. Wulff[ℓ], B.E. Wyborn[f], T.P. Yiou[ad], J. Žáček[af], D. Zarbock[m], P. Závada[ae], C. Zeitnitz[m], Z. Zhang[ab], H. Ziaeepour[ab], M. Zimmer[ℓ], W. Zimmermann[ℓ], F. Zomer[ab], K. Zuber[p]

[a] *I. Physikalisches Institut der RWTH, Aachen, Germany*[2]
[b] *III. Physikalisches Institut der RWTH, Aachen, Germany*[2]
[c] *Institut für Physik, Humboldt-Universität, Berlin, Germany*[2]
[d] *School of Physics and Space Research, University of Birmingham, Birmingham, UK*[3]
[e] *Inter-University Institute for High Energies ULB-VUB, Brussels, Universitaire Instelling Antwerpen, Wilrijk, Belgium*[4]
[f] *Rutherford Appleton Laboratory, Chilton, Didcot, UK*[3]
[g] *Institute for Nuclear Physics, Cracow, Poland*[5]
[h] *Physics Department and IIRPA, University of California, Davis, CA, USA*[6]
[i] *Institut für Physik, Universität Dortmund, Dortmund, Germany*[2]
[j] *CEA, DSM/DAPNIA, CE-Saclay, Gif-sur-Yvette, France*
[k] *Department of Physics and Astronomy, University of Glasgow, Glasgow, UK*[3]
[ℓ] *DESY, Hamburg, Germany*[2]
[m] *I. Institut für Experimentalphysik, Universität Hamburg, Hamburg, Germany*[2]
[n] *II. Institut für Experimentalphysik, Universität Hamburg, Hamburg, Germany*[2]
[o] *Physikalisches Institut, Universität Heidelberg, Heidelberg, Germany*[2]
[p] *Institut für Hochenergiephysik, Universität Heidelberg, Heidelberg, Germany*[2]
[q] *Institut für Reine und Angewandte Kernphysik, Universität Kiel, Kiel, Germany*[2]
[r] *Institute of Experimental Physics, Slovak Academy of Sciences, Košice, Slovak Republic*[7]
[s] *School of Physics and Chemistry, University of Lancaster, Lancaster, UK*[3]
[t] *Department of Physics, University of Liverpool, Liverpool, UK*[3]
[u] *Queen Mary and Westfield College, London, UK*[3]
[v] *Physics Department, University of Lund, Lund, Sweden*[8]
[w] *Physics Department, University of Manchester, Manchester, UK*[3]
[x] *CPPM, Université d'Aix-Marseille II, IN2P3-CNRS, Marseille, France*
[y] *Institute for Theoretical and Experimental Physics, Moscow, Russian Federation*
[z] *Lebedev Physical Institute, Moscow, Russian Federation*[7]
[aa] *Max-Planck-Institut für Physik, München, Germany*[2]
[ab] *LAL, Université de Paris-Sud, IN2P3-CNRS, Orsay, France*
[ac] *LPNHE, Ecole Polytechnique, IN2P3-CNRS, Palaiseau, France*
[ad] *LPNHE, Universités Paris VI and VII, IN2P3-CNRS, Paris, France*
[ae] *Institute of Physics, Czech Academy of Sciences, Praha, Czech Republic*[7,9]
[af] *Nuclear Center, Charles University, Praha, Czech Republic*[7,9]
[ag] *INFN Roma and Dipartimento di Fisica, Universita "La Sapienza", Roma, Italy*
[ah] *Paul Scherrer Institut, Villigen, Switzerland*
[ai] *Fachbereich Physik, Bergische Universität Gesamthochschule Wuppertal, Wuppertal, Germany*[2]
[aj] *DESY, Institut für Hochenergiephysik, Zeuthen, Germany*[2]
[ak] *Institut für Teilchenphysik, ETH, Zürich, Switzerland*[10]

[af] Physik-Institut der Universität Zürich, Zürich, Switzerland [10]
[am] Stanford Linear Accelerator Center, Stanford, CA, USA

Received 1 July 1996

Abstract

Technical aspects of the three major components of the H1 detector at the electron–proton storage ring HERA are described. This paper covers the detector status up to the end of 1994 when a major upgrading of some of its elements was undertaken. A description of the other elements of the detector and some performance figures from luminosity runs at HERA during 1993 and 1994 are given in a paper previously published in this journal.

1. Introduction

This paper describes the three major detector components of the H1 experiment:

- the central and forward tracking systems,
- the liquid argon and warm calorimeters,
- the muon detector consisting of the iron instrumentation and forward muon chambers.

A complete overview of the detector as well as descriptions of the magnets, luminosity system, trigger, slow control, data acquisition, off-line data handling and simulation can be found in a paper recently published in this journal (see Ref. [1]) or in Ref. [2] where both papers are combined. A survey of the detector parameters is given in Table 1 and, for the sake of convenience, the main elements of the detector are shown again in Fig. 1. This figure also shows the reference frame adopted in this experiment.

In the papers quoted above some performance results obtained during the first years of HERA operations can be found and the upgrade programme undertaken during the 1994–95 shutdown is outlined.

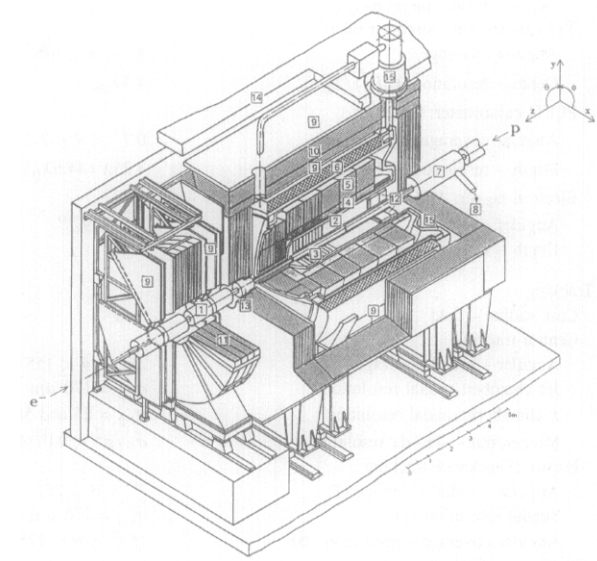

Fig. 1. Schematic layout of the H1 detector.

2. Tracking

The tracking system of H1 provides simultaneous track triggering, reconstruction and particle identification for the event topology particular to HERA electron proton collisions. It has been designed to reconstruct jets with high particle densities and to measure the momentum and angles of charged particles to a precision of $\sigma_p/p^2 \approx 3 \times 10^{-3}\,\mathrm{GeV}^{-1}$ and $\sigma_\theta \approx 1$ mrad.

Because of the asymmetry between the electron and proton beam energies many charged particles are produced at small angles θ to the incident proton (forward) direction. To maintain good efficiency for triggering and reconstruction over the whole solid angle, we divide the tracking system between the central and forward regions (see Fig. 2).

* Corresponding author. Tel.: +33 1 6908 2583, fax: +33 1 6908 6428, e-mail: cozzika@hep.saclay.cea.fr

† Deceased.

[1] Visitor from Yerevan Physics Institute, Armenia.

[2] Supported by the Bundesministerium für Bildung, Wissenschaft, Forschung und Technologie, FRG under contract numbers 6AC17P, 6AC47P, 6DO57I, 6HH17P, 6HH27I, 6HD17I, 6HD27I, 6KI17P, 6MP17I, and 6WT87P.

[3] Supported by the UK Particle Physics and Astronomy Research Council, and formerly by the UK Science and Engineering Research Council.

[4] Supported by FNRS-NFWO, IISN-IIKW.

[5] Supported by the Polish State Committee for Scientific Research, grant nos. SPUB/P3/202/94 and 2 PO3B 237 08, and Stiftung fuer Deutsch-Polnische Zusammenarbeit, project no. 506/92.

[6] Supported in part by USDOE grant DE F603 91ER40674.

[7] Supported by the Deutsche Forschungsgemeinschaft.

[8] Supported by the Swedish Natural Science Research Council.

[9] Supported by GA ČR, grant no. 202/93/2423, GA AV ČR, grant no. 19095 and GA UK, grant no. 342.

[10] Supported by the Swiss National Science Foundation.

Table 1
Summary of H1 detector parameters. Alternatively, design and test beam figures are given in brackets [ ]. Energies are given in GeV.

Calorimetry		
Main calorimeter: liquid argon (LAr)	electromagnetic part	hadronic part
Granularity	10 to 100 cm^2	50 to 2000 cm^2
Depth (number of channels)	20 to $30X_0$ (30784)	4.7 to $7\lambda_{abs}$ (13568)
Resolution $\sigma(E_{e,h})/E_{e,h}$	$\approx 11\%/\sqrt{E_e} \oplus 1\%$	$\approx 50\%/\sqrt{E_h} \oplus 2\%$
Stability of electronic calibration	$\leq$ 0.2% over one month	
LAr purity (decrease of signal)	$\leq$ 0.2% over one year	
Noise per channel	10 to 30 MeV	
Angular coverage – dead channels	$4^\circ < \theta < 154^\circ$	< 0.3%
Backward calorimeter: Pb-scintillator		
Angular coverage – granularity	$151^\circ < \theta < 176^\circ$	16 × 16 cm^2
Depth – resolution $\sigma(E_e)/E_e$	$21.7X_0$ (1 λ_{abs})	$10\%/\sqrt{E_e} \oplus 1.7[1]\%$
Tail catcher: iron–streamer tubes		
Angular coverage	$4^\circ < \theta < 176^\circ$	
Depth – resolution $\sigma(E_h)/E_h$	$4.5\lambda_{abs}$	$100\%/\sqrt{E_h}$
PLUG calorimeter: Cu–Si		
Angular coverage – granularity	$0.7^\circ < \theta < 3.3^\circ$	5 × 5 cm^2
Depth – resolution $\sigma(E_h)/E_h$	4.25λ ($44.6X_0$)	$\approx 150\%/\sqrt{E_h}$
Electron tagger: Tl(Cl/Br)		
Angular coverage – granularity	$\theta > 179.7^\circ$	2.2 × 2.2 cm^2
Depth – resolution $\sigma(E_e)/E_e$	$25X_0$	$\approx 10\%/\sqrt{E_e} \oplus 1\%$
Tracking		
Coil: radius – field	3 m	B = 1.15 T, $\Delta B/B \leq 2\%$
Central tracking		
Angular – radial coverage	$25^\circ < \theta < 155^\circ$	$150 < r < 850$ mm
Jet chamber: spatial resolution	$\sigma_{r\phi}$ = 170 μm	σ_z = 22.0 mm
z-chambers: spatial resolution	$\sigma_{r\phi}$ = 25 and 58 mm	$\sigma_z \approx 350$ μm
Momentum – dE/dx resolution	$\sigma_p/p^2 < 0.01[0.003]$ GeV^{-1}	$\sigma(dE)/dE = 10[6]\%$
Forward/backward tracking		
Angular – radial coverage (f)	$7^\circ < \theta < 25^\circ$	$120 < r < 800$ mm
Spatial resolution (f)	$\sigma_{r\phi}$ = 170 μm (σ_r = 29 mm)	$\sigma_{x,y}$ = 210 μm
Angular coverage – resolution (b)	$155^\circ < \theta < 175^\circ$	$\sigma_{x,y}$ = 1 mm
Trigger proportional chambers		
Angular coverage – channels	$7^\circ < \theta < 175^\circ$	3936
Muon detection		
Instrumented iron		
Angular coverage – total area	$4^\circ < \theta < 171^\circ$	4000 m^2
Number of channels	wires: 103700, strips: 28700, pads: 4000	
Spatial resolution	σ_{wire} = 3–4 mm	σ_{strip} = 10–15 mm
Angular – momentum resolution barrel	$\sigma_\theta(\sigma_\phi)$ = 15(10) mrad	$[\sigma_p/p \approx 0.35]$
Forward muon toroid		
Angular coverage – resolution	$3^\circ < \theta < 17^\circ$	$[0.25 < \sigma_p/p < 0.32]$
Overall size (x, y, z) – weight	12 × 15 × 10 m^3	2800 t

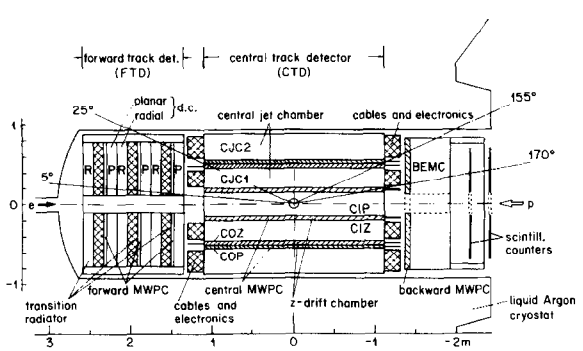

Fig. 2. The H1 tracking system (r–z view).

Two mechanically distinct tracking detectors have been constructed, the central (CTD) and forward (FTD) tracking devices respectively. Each is optimized for tracking and triggering in its angular region.

Track reconstruction in the central region (see Fig. 3) is based on two large concentric drift chambers, CJC1 and CJC2. The chambers have wires strung parallel to the beam axes (z-direction) with the drift cells inclined with respect to the radial direction. We have measured a space point resolution of 170 μm in the drift coordinate ($r\phi$ plane) and can, by comparing signals read out at both wire ends, achieve a resolution of one percent of the wire length in z. From the signals recorded in these chambers the transverse

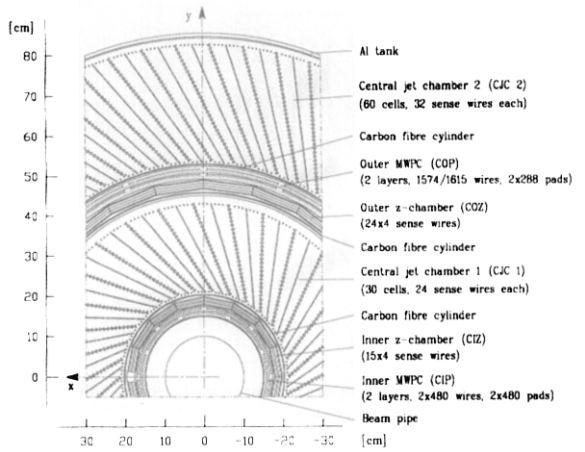

Fig. 3. Central tracking system, section perpendicular to the beam.

track momentum is determined and in addition the specific energy loss dE/dx is used to improve particle identification.

Two thin drift chambers, the central inner (CIZ) and central outer (COZ) z-chambers measure the z coordinates with better accuracy than charge division and complement the measurement of charged track momenta in the central chambers. The CIZ chamber fits inside CJC1, and the COZ chamber fits in between CJC1 and CJC2. These two chambers deliver track elements with typically 300 μm resolution in z and 1 to 2% of 2π in ϕ. This requires a drift direction parallel to, and sense wires perpendicular to the beam axis.

Triggering over the full solid angle is based on multiwire proportional chambers with pad readout in the central and forward region and wire readout in the backward direction. They provide a fast first level (L1) trigger decision which can be used to distinguish between successive beam crossings. Furthermore, in the central and forward region, combinations of pads hit in the central inner proportional chamber (CIP), the central outer proportional chamber (COP) and the forward proportional chambers (FWPC) are used to trigger on tracks coming from a nominal interaction vertex. First level track triggers are also derived from the central drift chambers.

Each of the central chambers has an independent gas volume and separate electrostatic shielding. They were built and tested separately, and then assembled and locked to one mechanical unit. The detector walls are thin to reduce photon conversion, and in particular its effect on identification of primary electrons. Neighboring volumes share a thin (1.5 mm) cylinder of carbon fiber reinforced epoxy with a 50 μm aluminium coating on each side. The complete system of central tracking detectors is housed in a single aluminium cylinder of 4 mm wall thickness. The assembly also provides a precise alignment of the chambers relative to the outside support.

Charged tracks produced at polar angles θ close to the beam axis (forward $\theta < 30°$, backward $\theta > 150°$) no longer traverse the full bending ($r\phi$) plane radius of the solenoid magnetic field. Consequently in the CTD both track pattern recognition and accuracy of track reconstruction deteriorate as the measured track length and the number of precision space points decrease. A way of rectifying this loss is to compensate for the reductions in track length and the number of points in the central region by means of a higher radial density of accurate space points obtained using wires strung in the bending plane closely spaced in z. This is provided by the forward tracking detector which consists of an integrated assembly of three nearly identical supermodules. Each supermodule includes, in increasing z: three different orientations of planar wire drift chambers designed to provide accurate θ measurements, a multiwire proportional chamber (FWPC) for fast triggering, a passive transition radiator and a radial wire drift chamber which provides accurate $r\phi$ (drift coordinate) information, moderate radius measurement by charge division and limited particle identification by measuring the transition radiation produced immediately upstream.

The FTD and CTD are linked together, aligned and surveyed prior to installation into the calorimeter cryostat.

The description of the individual components of the tracking detector below is followed by sections which describe the features common to all drift chambers, namely the readout and pulse shape analysis and the gas systems used for all chambers.

2.1. Central jet chambers: CJC1 and CJC2

2.1.1. Design criteria

The design of CJC1 and CJC2 [3,4] follows that of the jet chamber used in the JADE experiment at PETRA [5]. The wire pattern characteristic for a jet chamber is a plane of anode sense wires parallel to the beam line with two adjacent cathode planes shaping the drift field. In the CJCs the latter planes are also made of wires.

A jet chamber cell extends azimuthally from the sense wire plane to both adjacent cathode wire planes, and radially over the full radial span of CJC1 or CJC2 each with no further subdivision, as shown in Fig. 3. This minimizes the disturbing influence of field shaping wires at the inner and outer radii.

The jet cells are tilted by about 30° such that in the presence of the magnetic field the ionization electrons drift approximately perpendicular to stiff, high momentum tracks originating from the center. This not only gives optimum track resolution, but also leads to additional advantages. The usual drift chamber ambiguity is easily resolved by connecting track segments of different cells. The wrong mirror track segments do not match, as demonstrated in Fig. 4. They also do not point to the event vertex and therefore obstruct only small parts of a real track in the opposite half cell. Each stiff track crosses the sense wire plane at least once in CJC1 and in CJC2. From the fine match at the crossing, the passing time of a particle can be determined to an accuracy σ of $\sim$ 0.5 ns. This allows an easy separation of tracks coming from a different bunch crossing. The drifting electrons from

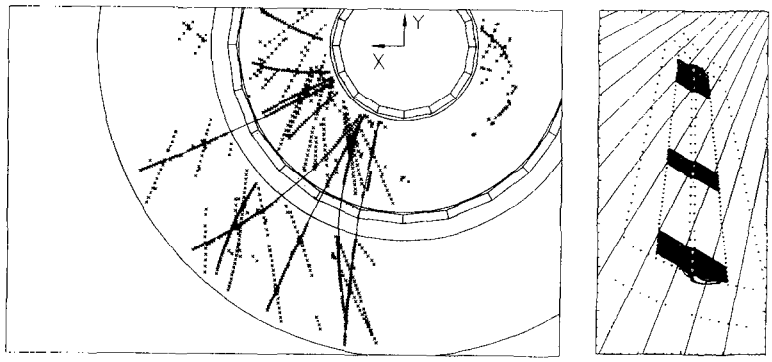

Fig. 4. Left: Electron–proton scattering event as seen in the CJC showing tracks found by the pattern recognition program and mirror tracks. Right: Simulation of a CJC cell indicating the drift regions of the senses wires, drift lines and isochrones. The straight lines represent infinite momentum tracks from the beam axis.

stiff tracks arrive at neighboring sense wires with a time shift of about 100 ns, and therefore produce only negligible disturbance by cross-talk. Every track traverses several regions of uniform driftfield inside the cells. Systematic errors of drift time measurement, which are known to arise in the nonuniform fields near the cathode and sense wire planes, reverse sign at the crossing, and therefore cancel in good approximation.

Adjacent sense wires are separated by two potential wires (see Figs. 3 and 4). This reduces both the surface field and the cross-talk by nearly a factor of 2 as compared to a single potential wire. Most important, it allows to adjust drift field and gas amplification nearly independently. The actual positions of the sense wires are staggered off the nominal sense wire plane by ± 150 μm, such that adjacent wires are pulled by the electric field to definite positions on opposite sides of the plane.

A cell is azimuthally limited by two cathode wire planes, and at the inner and outer radius by the field wires. The cathode wires are set to a voltage proportional to the distance from the sense wire plane in order to create an uniform drift field and hence a constant drift velocity over almost all the cell. The voltages for the cathode wires are supplied by a resistor network (cathode chain) on the adapter cards connected to the cathode wires. The field wires shape the field at the inner and outer end of the cell such that the deviations from a uniform drift field are minimal. The sense wires are connected to a positive voltage and are AC coupled to the amplifiers. The potential wires are set to ground. To prevent ageing of the chambers due to high electric surface fields, the diameters of the potential, cathode and field wires were chosen conservatively large: 127, 180 and 500 μm. This limits the surface field to ≤ 2 kV/mm. The anodes are 20 μm (25 μm at the cell ends) gold plated tungsten wires with 3% rhenium, having a resistivity of 300 Ω/m.

The electrostatics of the cells have been studied in detail by computer simulations. Fig. 4 shows drift lines and isochrones in CJC1 for a Lorentz angle of 30°. In most of the drift region the electric field is constant to better than 1%. At the first and the last sense wires the wire geometry produces local distortions of the field which, however, do not exceed 2%. This introduces only negligible variations of the drift velocity, in particular around the maximum of the drift velocity.

The parameters of the jet chamber are listed in Table 2. All sense wires are read out at both ends and yield via charge division a z-measurement.

2.1.2. Mechanics

The volume of each jet chamber is defined by two endwalls perpendicular to the beam line and an inner and outer cylinder concentric to the beamline. The volume has to be gas tight and to support small overpressure with respect to the atmosphere.

The bulk material of the endwalls was chosen to be 10 mm glass fiber reinforced epoxy [6], combining excellent insulation with good mechanical properties. The fact that there are two jet chambers allowed relatively thin endwalls, because the support lengths between inner and outer cylinders are small and thus the bending under the summed wire tension could be kept below 1 mm.

To facilitate installation, insulation and HV testing of all connections, the signal- and HV leads are integrated into the endwall structure by means of multilayer printed circuit (PC) boards. One board (2 mm thick) covers one drift cell. Of its four layers, one provides a nearly complete electric shield of the chamber, while the others make the contacts between the wire feedthroughs and the (signal and HV) connector sockets. A second PC board inside the chamber, 0.8 mm thick, carries strips for shaping the end fields.

Optimum precision of the wire positions is achieved by first gluing 3 mm thick massive brass pins into pre-bored holes in the endwalls, and then drilling precision holes into the brass. The precision of the sense wire positions, ± 15 μm within one cell is determined by small excentric holes in the brass. Details of the wire supports can be found in Ref. [3].

The endwalls are kept apart by four cylinders. For the inner and the outer cylinder of CJC1 and the inner cylinder of CJC2 carbon fiber reinforced epoxy (1.5 mm thick) has been chosen because of its excellent mechanical stability

Table 2
Central jet and z-chamber parameters.

	Unit	CJC1	CJC2	CIZ	COZ
Active length Δz	mm	2200		1800	2160
Active zone starts at z	mm	−1125		−1080	−1105
Total length Δz [a]	mm	2500		2467	2590
Mechanical length Δz	mm	2230		2254	2230
Inner radius R_i	mm	203	530	173.5	460
Outer radius R_o	mm	451	844	200	485
Active radial length	mm	224	296	20	24
Number of cells (rings)		30	60	15	24
Number of sense wires per cell (ring)		24	32	4	4
Number of potential wires per cell (ring)		50	66	3	6
Number of field wires per cell		10	10		
Number of cathode wires per cell		49	65		
Sense wire distance	mm	10.16		5.6(7.0)	6.0
Maximum drift distance at R_i	mm	22.9	28.5	61.25	45
Maximum drift distance at R_o	mm	44.5	43.1		
Sense wire tension	N	0.65		0.2	0.9
Mean wire length	mm	2200		1120	2970
Drift velocity [b]	mm/μs	≈ 50		52	48.5
$\sigma_{r\phi}$	mm	0.170		28	58
σ_z	mm	22		0.26	0.20
Double hit resolution	mm	2		4.6	3.5

[a] Including preamplifiers.
[b] For the gas mixtures given in Table 7.

(Young's modulus $\epsilon = 80\,\mathrm{kN/mm^2}$) and very long radiation length ($X_0 = 230$ mm). The chamber volume forms a Faraday cage in order to be screened against external electromagnetic noise. Since the conductivity of the carbon fibers is not sufficient in all directions, an aluminium coating of the inner and outer surface was mandatory. The thickness of 50 μm of the Al surface liner was a compromise between electromagnetic screening down to low frequencies (skin depth at 20 MHz in Al is ≈ 20 μm) and minimum material. The outer cylinder of CJC2 is made of aluminium (4 mm thick) and is the main support vessel for all tracking detectors. It has feet which slide on rails positioned on the inner warm wall of the liquid argon cryostat and which are the mechanical link to the rest of the H1 detector. At both ends the Al cylinder has thicker flanges ($\Delta r = 12$ mm), which are machined to 0.1 mm tolerances in order to house the endwalls precisely. At final assembly the stability and shape of the Al cylinder is guaranteed by the insertion of the endwalls.

2.1.3. Calibration and performance

The accurate measurement of the track parameters is limited by the intrinsic resolutions, namely $\sigma_{r\phi} \approx 150$ μm for drift time measurements with a gas mixture of Ar–CO_2–CH_4 (89.5 : 9.5 : 1.0), $\sigma_z \approx 1\%$ of the wirelength for the charge division measurements (limited by pulseheight and noise), and $\sigma_{dE/dx} \approx 6\%$. With this gas the drift velocity at nominal HV is 50 mm/μs.

A large variety of constants is involved to determine the coordinates of a hit from the timing (t) and pulse-integral (Q) of a drift chamber signal (see Section 2.4.5 for (Q, t) analysis). We distinguish overall and wire dependent constants.

The overall constants – event timing, average drift velocity and average Lorentz angle – are sufficient to determine the track parameters with moderate accuracy, e.g. $\sigma_{r\phi} \approx 350$ μm. They are determined and continuously monitored by fitting them as additional parameters to long, high momentum tracks (see Section 2.1.4). The use of an average effective wire length and gain gives resolutions of $\sigma_z \approx 5$ cm and $\sigma_{dE/dx} \approx 17\%$.

The wire dependent constants – timing, signal propagation, absolute gain, relative gain and position of both wire ends – have been determined in two steps. The first step consists of the evaluation of data where the 4 odd/even wires of an 8-channel amplifier card on both chamber ends are pulsed separately and simultaneously. This gives the relative timing of the 4-wire groups, the timing difference, and the relative gain at the two wire ends. The start values for the effective wire length are determined, apart from an overall factor. In the second step the residuals of hits for reconstructed and fitted tracks are evaluated to obtain the absolute values of the individual wire constants. This improves the resolution to $\sigma_{r\phi} = 170$ μm, $\sigma_z = 2.2(3.3)$ cm for protons (pions) and $\sigma_{dE/dx} = 10\%$ (see Figs. 5 and 6 and Table 2).

The resolution achieved in the z-coordinate depends on the deposited ionization (Fig. 5). Data from e–p collisions were analysed [7]. The dependence of the specific ionization on the particle momentum is show in Fig. 6. There are

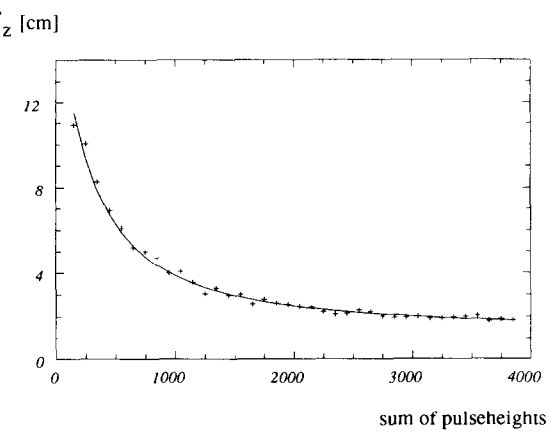

Fig. 5. Dependence of the CJC z-resolution on the amount of ionization. A minimum ionizing particle deposits typically 1000 counts.

clearly visible bands for pions, proton and deuterons, where the latter two particle species are mainly produced by protons colliding with the residual gas in the beam pipe.

2.1.4. Track reconstruction

Track parametrization Tracks of charged particles are characterized by the five helix parameters: the signed curvature ($\kappa = \pm r^{-1}$, positive if the direction ϕ coincides with a counter-clockwise propagation along the circle), the signed closest distance from the z-axis in the (x, y)-plane d_{ca}, positive if the vector to the point of closest approach and the trajectory direction form a right-handed system), azimuth and polar angle (ϕ and θ), and the z-position (z_0) at the point of closest approach. The first three parameters are determined by a circle fit to the data in the xy-projection using the non-iterative algorithm of Karimäki [8]. The circle equation is expressed in polar coordinates (r, φ) as

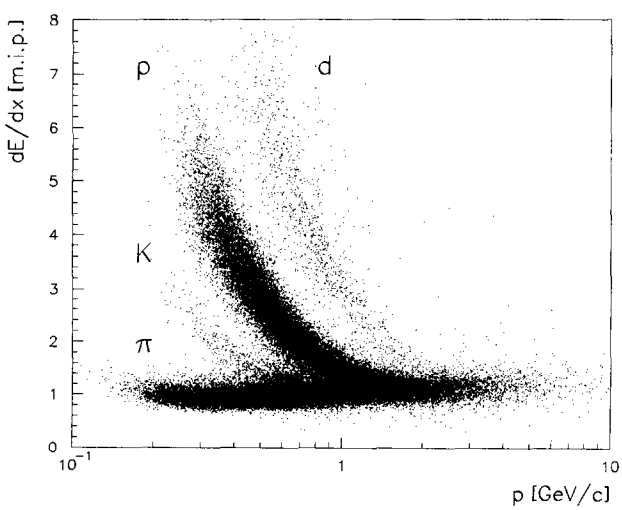

Fig. 6. Specific ionization versus particle momentum measured in the CJC in HERA runs.

$$\tfrac{1}{2}\kappa\left(r^2 + d_{ca}^2\right) + (1 - \kappa d_{ca})\, r \sin(\phi - \varphi) - d_{ca} = 0.$$

For a track traversing both rings of the CJC a single parametrization for both rings is usually sufficiently accurate. Due to multiple scattering in the material between the two rings (2% X_0) for some tracks two separate sets of parameters are determined, which are constrained to join in a point between the two rings under an angle compatible with the mean multiple scattering angle.

The other two parameters are determined by a linear least-squares fit of $z_i = z_0 + S_i^{xy}(\mathrm{d}z/\mathrm{d}S)$, where S_i^{xy} is the track length for the point z_i in the xy-projection, with $S^{xy} = 0$ at d_{ca}. The slope parameter $(\mathrm{d}z/\mathrm{d}S)$ determined by the fit is converted to the angle θ by $\theta = \arctan(1/(\mathrm{d}z/\mathrm{d}S))$.

The track finding is followed by further modules to determine the xy-vertex for a given run, and to perform track fits to the primary and secondary vertices. The track parameters in this stage are κ, ϕ and θ, together with the xyz-coordinates of the vertex and the error matrix.

Track finding Two versions are used for the track finding and fitting. A fast version, efficient for tracks originating from the primary vertex with a momentum > 100 MeV/c, is used on the fourth trigger level filter farm (see Section 5.5 of Ref. [1]) for background rejection and fast classification of events. It is roughly a factor 10 faster than the standard version, which is efficient for all kinds of tracks and is used within the normal reconstruction.

The first phase of track finding, the search for short track elements (curvature negligible), is done independently in the angular cells with 24 (CJC1) and 32 (CJC2) radial wires. Within angular sectors track-element finding does not depend on parameters like the Lorentz angle or the drift velocity. However accurate values of these parameters are necessary when hits from more than one angular cell are combined. Track finding is based almost exclusively on drift time data in the xy-plane and includes removal of outliers, which would distort the circle fit. Only in a later stage the measured z-values are used; here it is again necessary to remove outliers before the data are fitted.

For the fast track finding it is sufficient to determine the bunch crossing time t_0 for an event from the threshold in the drift time histogram. The first step involves the search for track elements defined by three hits within angular cells found on three wires with a wire distance of two. The algorithm starts by trying all pairs of hits at wires $n \pm 2$ (n = wire index). Possible values of drift distances $\bar{d}^n$ at the wire n are calculated by $(d_i^{n-2} + d_k^{n+2})/2$ and/or $|d_i^{n-2} - d_k^{n+2}|/2$ (i, k = hit indices) and stored in a list, if the direction of the pair does not deviate too much from the radial direction. Very dense regions with many hits are not analysed. This list is then compared with the measured values d_j^n and for small differences $|d_j^n - \bar{d}^n|$ the indices of the hits at the three wires are stored as a possible track element. From these hit triplets the curvature κ and the angle ϕ_m can already be determined with sufficient accuracy assuming $d_{ca} \equiv 0$. The

parameter ϕ_m is the track angle at the mean radius r_m of the CJC1 and the CJC2, respectively. No attempt is made at this stage to resolve the drift sign ambiguity; triplets with a large value of $|\kappa|$ are rejected, otherwise both solutions are kept. A z-value and a value for dE/dx are assigned to the triplets from the median of the three single-hit values and later used to determine the z-slope and -intercept z_0 and the mean dE/dx value of the track.

Tracks from the origin cluster in the plane of the two parameters κ and ϕ_m of the triplets, with a width of typically only one degree for ϕ_m. These clusters are sufficiently separated, that after finding them a first track definition is achieved. The coordinates of triplets within the clusters are then used in a circle fit, now allowing $d_{ca} \neq 0$, and by a z-fit. Track candidates with large $|d_{ca}|$ and $|\kappa|$ values are rejected.

The track candidates are then checked in the order of decreasing number of triplets (decreasing significance) rejecting tracks with several triplets already used before for an accepted track. Drift sign ambiguities are normally resolved at this stage, since most tracks traverse several cells and the correct solution has a much larger number of triplets than the wrong one. The fast track finding is in general efficient enough to allow sensitive recognition of background or classification of physics events.

The standard track finding starts from the results of the fast track finding and first improves the time reference value t_0 for an event by fits to the drift length values of long tracks. For a given track the values of the circle parameters are used to calculate the expected drift length for all possible wires. The difference between the measured and the expected drift length is then calculated for all hits, taking into account the sign of the drift length. To these differences an expression is fitted, which in addition to a parabolic dependence on the track length (to allow for a small inaccuracy in the track parameters) parameterizes the effect of a t_0 difference (which depends on the sign of the drift length) and of a small difference of the drift velocity. This fit yields an accurate value for t_0 and allows in addition to detect changes of the drift velocity. At the same time the method improves the definition of tracks, since often the range of the hits found is extended. Another circle fit is performed to all long tracks traversing more than one cell (drift sign ambiguity resolved). If the χ^2 value of the track fit (after removing single bad hits eventually) is acceptable the complete set of track parameters is stored already at this stage, the hits assigned to the track are flagged and not used in the following steps.

The first phase of standard track finding again searches for track elements defined by three hits, but now on adjacent wires. All possible wires are considered, except for very dense regions. Triples with common hits are connected by pointers and when all hits of an angular cell are analysed, chains of hits are extracted. These chains of hits are then checked by a fit to the drift times for effects like kinks; eventually long chains of hits are split into two shorter chains. For long chains the staggering of wires sometimes allows already to resolve the drift sign ambiguity; otherwise both solutions are kept. Chains accepted at this stage are stored as track elements with parameters from the fit.

Short track elements are merged to larger ones first within the same or neighboring angular cells, then within one ring and lastly from both CJC1 and CJC2. The merging algorithm starts with a comparison of pairs of track elements with similar helix parameters. If the distance between them is not so large that they could belong to the same track, a χ^2-fit in the xy-plane is performed. The list of all acceptable pairs is sorted in the order of an increasing "distance", assigned to each pair. The distance is constructed from the χ^2-value and other parameters (e.g. the length of the track element). The list of pairs is then checked sequentially, starting with the "close" pairs. Two elements from a pair are combined to a new (longer) track element, if acceptable. If in this sequence one element of a pair has already been used in the construction of a new element, the fit to the modified element(s) is repeated and rejected eventually. By this process longer and more accurate track elements are formed, starting with the simple and clear cases, thus avoiding with high probability a wrong combination of short track elements.

For the final improvement of the track finding efficiency and precision the expected drift length is calculated for all possible wires and for all track elements ordered by their length. Hits at the expected wires which are not already used by another track are collected. The differences between measured and expected drift length are analysed to reject incompatible hits. Tracks found are allowed to contain rather large gaps of several wires, since parts of tracks may be invisible, especially within jets, due to the limited double track resolution. The fits for the track parameters are repeated using all acceptable hits.

Very short track candidates are rejected, unless they start with the first few wires of a ring. The energy loss dE/dx for a given track is determined from the mean of single-hit values $1/\sqrt{k_i} = 1/\sqrt{(dE/dx)_i}$, excluding hits which are close to another track. An analysis based on a likelihood method has improved the dE/dx to below 10% (see Ref. [9]).

Vertex determination The e–p-interaction vertex region in the xy-plane extends over a few hundred μm with a rather stable mean position for a sequence of runs. The mean vertex coordinates (x_v, y_v) are determined using long high momentum tracks with a small value of d_{ca} from a few hundred events and minimizing the sum of squares of the distance of the tracks to the vertex.

The known (x_v, y_v) position of the run vertex can be used as a constraint to improve the parameters of tracks originating from this vertex, if the effect of multiple scattering in the beam pipe and the CJC wall for low-momentum tracks is taken into account. Since the standard deviation of the curvature value is roughly inversely proportional to the track length squared, the track precision is significantly improved by this vertex fit in the xy-plane. A z-value of the primary

interaction vertex in an event is determined from all tracks fitting to the xy-vertex. The polar angle θ for these tracks is changed accordingly.

Within the standard reconstruction program a search is made for neutral particles decaying into a pair of oppositely charged particles with tracks in the CJC; in addition to K^0_S, Λ and $\bar{\Lambda}$ particles also e^+e^--pairs from conversion are found by this module. Candidate pairs are determined using simple geometrical cuts. For each candidate pair a fit is performed applying geometrical (common secondary vertex of the charged particles) and kinematic constraints. Use is made of the known position of the primary vertex. Momentum balance perpendicular to the direction of the neutral particle is used as kinematic constraint, but no masses are assumed. For a very small opening angle of the pair the transverse momenta in the xy-plane are both constrained to zero, to improve the stability of the fit for e^+e^--pairs. Pairs with an acceptable χ^2-probability are stored.

At later stages of the analysis alternative methods for reconstructing secondary vertices are also employed (see Refs. [10,11] and Fig. 33 of Ref. [1]). Kalman filtering techniques have also been shown to be useful [12].

2.2. Central z-chambers

The central inner and outer z-chambers (CIZ, COZ) surround the inner half of the jet chamber and complement the measurement of charged track momenta in the latter chamber. These two chambers deliver track elements with typically 300 μm resolution in z, which can be linked to those obtained from the jet chamber for the final accuracy on both the longitudinal as well as the transverse momentum components. The polar angles covered by CIZ and COZ are $16° < \theta < 169°$ and $25° < \theta < 156°$, respectively. Since the CIZ uses the inner carbon fiber wall of the CJC for closing its gas volume, and the COZ uses the outer carbon fiber cylinder for its basic structural element, the thickness of both chambers could be kept small, namely 0.6% X_0 for CIZ and 0.7% X_0 for COZ in the active zones and 1.2% and 1.5%, respectively averaging over the cell wall material. Furthermore the total amount of dead zones in azimuth imposed by readout channels and wire supports is only 7.7% and 5.3% of 2π respectively. The basic parameters of both chambers are given in Table 2 and the gas mixtures used are given in Table 7. A first level, background rejecting trigger [13] combines CIZ and COZ hits to trigger on straight tracks pointing to the interaction region (see Section 5.3.1 of Ref. [1]).

2.2.1. CIZ

For CIZ a laminar construction technique similar to that described below for CIP was used, starting from a steel mandril with an inner diameter of 347 mm. Successive layers include 25 μm Kapton with a 2.5 μm Al coating for electrical shielding, a 6 mm thick Rohacell [14] cylinder with its outer surface machined and polished to produce 16 flat surfaces forming a regular polygon in cross section (see

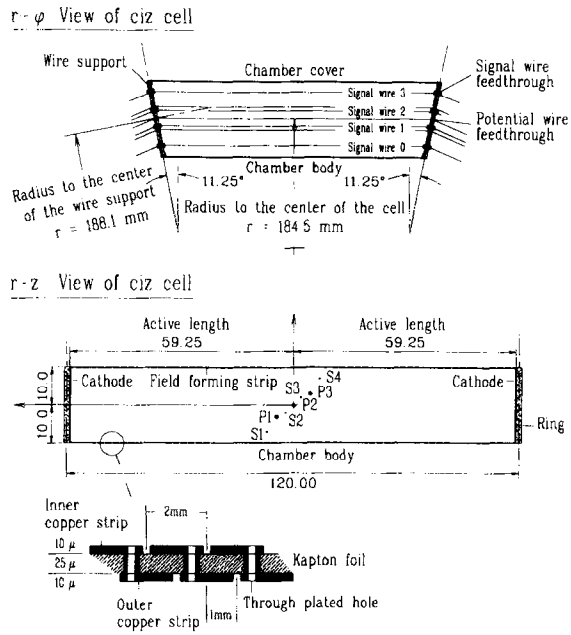

Fig. 7. Longitudinal and transverse cross section through a cell of the CIZ. S: signal wires, P: potential wires, the z-coordinates are given relative to the center of the cell [mm].

Fig. 3), and a 25 μm Kapton foil with 10 μm Cu field forming strips on both sides. The 15 independent cells are separated by printed circuit boards, 1.6 mm thick with 5 μm Cu on each side serving as cathode planes. The cells are closed electrically with another Kapton foil identical to that on the bottom of the cell, here backed by 1 mm Rohacell. The end flanges of the CIZ are sealed against the CJC end plates with O-rings. Further constructional details, e.g. on the specially designed wire feedthroughs, can be found in Refs. [15–17].

Fig. 7 shows the geometry of the drift cell. The sense wire planes are tilted by 45° with respect to the normal to the chamber axis, with the first nine cells in the backward direction tilted backward and the last six in the forward direction tilted forward, i.e. following the direction of the tracks crossing the respective cells. As explained in Ref. [15] this tilt produces a distortion of the equipotential lines resulting in a non-uniform distribution of the charge collected on the four wires and an equivalent tilt of the isochrones. This unusual wire arrangement solves the left–right ambiguity automatically without a need for wire staggering and furthermore eliminates the dependence of the resolution on the crossing angle. The wires are soldered to both side walls of a 23 mm wide cable channel at $\phi = 0°$. Here the signal wires are connected to line drivers and the potential wires to HV cables. The line drivers provide the impedance matching to the preamplifiers mounted on the end plate. A high resistivity alloy (Elgiloy [18], 3 kΩ/m) was selected as sense wire material ($\oslash$ 20 μm) to improve the measurement of the ϕ coordinate along the wire by charge division. The potential wires are made from Au ($\oslash$ 120 μm). To save space the HV cables to the electrodes and cathodes are buried in the Ro-

hacell chamber body and the miniaturized 10 MΩ resistors (1.25 mm × 2 mm × 0.5 mm), which supply the field forming strips are embedded in the printed circuit board chamber partitions. The structure of the field shaping electrodes is indicated in Fig. 7. For the gas mixture listed in Table 7 the chamber is operated with a cathode voltage of 4500 V, a potential wire voltage of 2250 V and a field gradient of 53 V/mm.

Since the CIZ is the drift chamber closest to the interaction point, a dedicated current monitoring system (see Ref. [19] for details) was included into each potential wire supply line. It allows to measure the currents in the nA range. These wires control the gas amplification in the chamber. In this way the activity introduced by interaction products or stray beam can be monitored. Typically we found 10 nA current increase per ring for a luminosity of 20 $mb^{-1}s^{-1}$. This corresponds to an accumulated charge of 10 Cb/m per wire for an integrated luminosity of 100 pb^{-1}.

Apart from a narrow strip near the cell walls the chamber efficiency was measured to 98% in test beams at PSI [16]. From test beam data the resolution was found to be σ_z = 320 μm independent of the drift distance and the crossing angle in the range $10° < \theta < 110°$. These results could be confirmed with cosmics ray data, where central jet chamber tracks were extrapolated into the z-chambers and then linked to the corresponding track elements. The average deviation from a straight line fit (in the r–z plane) is σ_z = 260 μm for CIZ internal track elements and 400 μm for linked tracks. For the ϕ-projection a resolution of 2.4% of the wire length was measured. Double pulses can be resolved, if their separation exceeds 90 ns, which converts into 4.6 mm spatial separation in z [16].

2.2.2. COZ

This chamber was also built on a Rohacell body with the cross section of a regular 24-edge polygon (Fig. 3), but resting on a cylinder of carbon fiber reinforced plastics. The Kapton foils with field shaping copper strips were glued to the Rohacell surfaces. Guided by a mechanical positioning device the wire supporting rods (G10 with Cu strips, double sided) were placed and soldered to the Kapton foil. Between these rods planar cathodes were introduced made of G10/Cu with holes to enable the gas flow through the chamber. The top cover of the drift cell structure consists of a Kapton–Rohacell sandwich which is fixed at the cathodes. The chamber has a cylindrical shape due to its G10-Cu gas cover held by the endflanges. Further details can be found in Refs. [17,20].

Fig. 8 shows a schematic view of the COZ. The dead zones for the wire readout are distributed in azimuth which allows a corresponding distribution of the preamplifiers at the end flanges and minimizes the dead area of the chamber. The anode signals are transmitted by twin readout lines (signal-ground signal, length 20 to 120 cm) from the wire ends to the preamplifiers on both chamber ends.

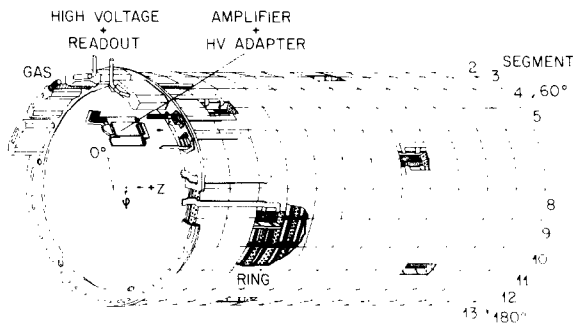

Fig. 8. Schematic view of the COZ.

Each drift cell is 24 mm high, the maximum drift length is 46 mm which limits the drift time to about 1 μs. Each cell has four sense wires (Stablohm [18], ⌀ 48 μm, 0.6 kΩ/m) in the symmetry plane of the cell and three pairs of potential wires (CuBe, ⌀ 127 μm). The wire feedthroughs in the supporting rods are kept in their nominal position to about 30 μm (σ). No wire stagger is implemented. Mirror tracks can be removed in the analysis since they do not point to the vertex.

The COZ is typically operated with a cathode voltage of 3000 V, a potential wire voltage of 2250 V and a field gradient of 82 V/mm. For the gas mixture listed in Table 7 this gives a drift velocity of 48.5 mm/μs, as determined from tracks crossing the sense wire plane and the cathode plane, respectively.

Inefficiencies along the cell walls and other performance parameters were studied in test beams (3 GeV electrons at DESY and low energy pions and electrons at PSI, see Refs. [21,20]). Apart from a small region near the sense wire feedthroughs the efficiency was determined to be 98% over the full drift cell. For a 90° crossing angle the resolution measured at HERA is about 200 μm, deteriorating to 500 μm for low crossing angles. The azimuthal angle is determined by charge division to an averaged accuracy of 7.2°, i.e. 2% of the wire length. Double pulses can be resolved if their separation is larger than 70 ns which corresponds to 3.5 mm distance. For a discussion of the optimum method to resolve double tracks and a comparison of different algorithms for (Q, t) analysis we refer to Refs. [20–22].

2.3. Forward tracking detector

The forward tracking system is designed to provide an accurate measurement of charged particles in the forward direction (momentum resolution $\sigma_p/p^2 < 0.003$ GeV^{-1} and track angular resolution $\sigma_{\theta,\phi} < 1$ mrad), track information on individual particles within jets, electron identification by means of transition radiation detection and a fast forward ray track trigger. Details about track finding and fitting can be found in Ref. [23].

The layout of the FTD is illustrated in Figs. 9 and 10. Key parameters are listed in Table 3. The drift chambers have different wire geometries – the planar ones contain parallel

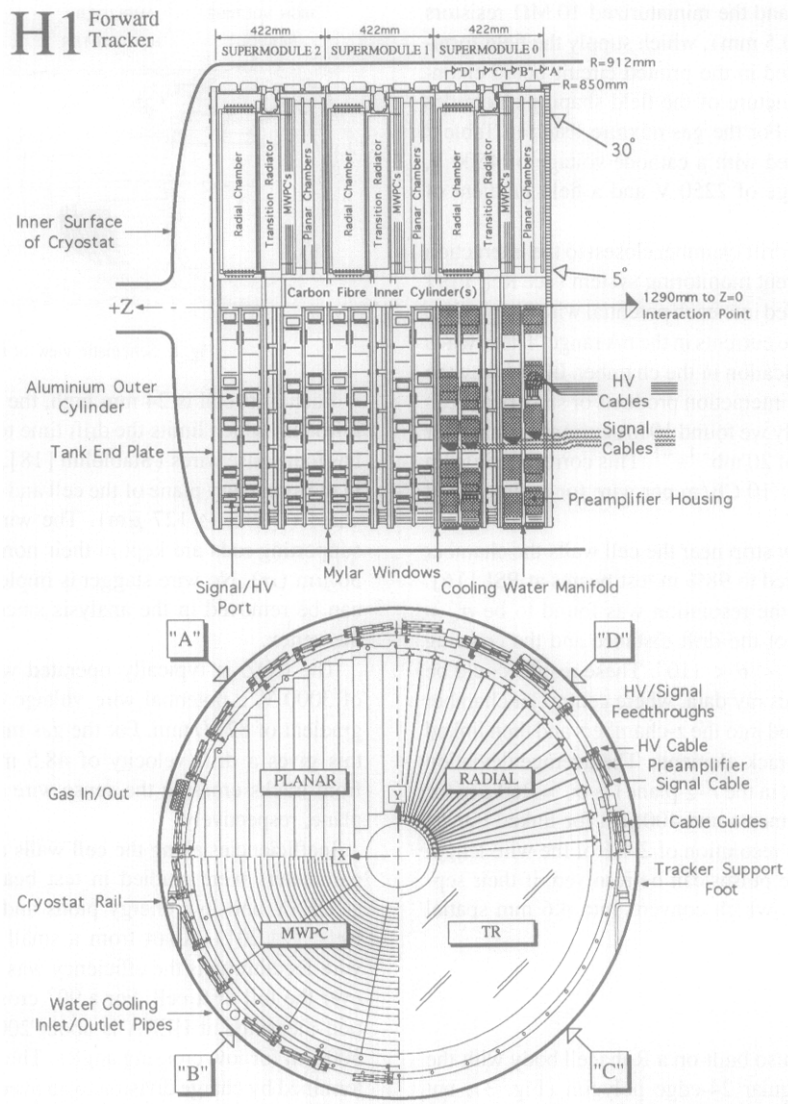

Fig. 9. Forward tracker overview. Top: cross section in the r, z-plane showing the three supermodules. Bottom: cross section in the r, ϕ-plane showing the basic cell structure of each supermodule component in one quadrant (A: planar chamber, B: FWPC, C: TR, D: radial chamber).

wires whereas the radial ones have wires radiating outwards from the beam pipe – all wires being strung perpendicular to the beam direction. The planar module consists of three drift chambers, each four wires deep in z and rotated at 60° to each other in azimuth. It is located closest to the central tracker in each supermodule, since its homogeneous spatial precision in x and y is most suitable for linking to tracks in the center. For practical reasons the FWPC (Section 2.5.1) is mounted directly behind the planar drift chambers in order to share the same gas mixture and maximize the geometrical trigger efficiency of the FTD. After the FWPC the particles traverse a transition radiator consisting of 400 polypropylene foils contained in its own gas volume. The transition radiation photons pass through a thin mylar window and are detected in the radial chamber which produces up to 12 accurate space points from ionization drift timing and charge division. To improve double track resolution the second and third radial modules are rotated by 3.75° and 2.5° ($\frac{1}{2}$ and $\frac{1}{3}$ of a wedge) relative to the first. The interleaving of planar and radial chambers provides the optimum lever arm for momentum measurement.

The individual chambers were assembled and tested separately. The components for a single supermodule were installed into a three section tank consisting of aluminium outer cylinders ($\varnothing_{max}$ = 1700 mm) and glass free carbon fiber inner cylinders ($\varnothing_{min}$ = 243 mm, 4 mm thick, lined with Al foil), each tank section forming an independent gas volume and electrically isolated environment. Each chamber is bolted to the rigid central U-shaped outer cylinder using a set of precision dowels for alignment. Assembly was carried out on high quality surface tables with dimensional tolerances kept to < 30 μm throughout the build sequence. After

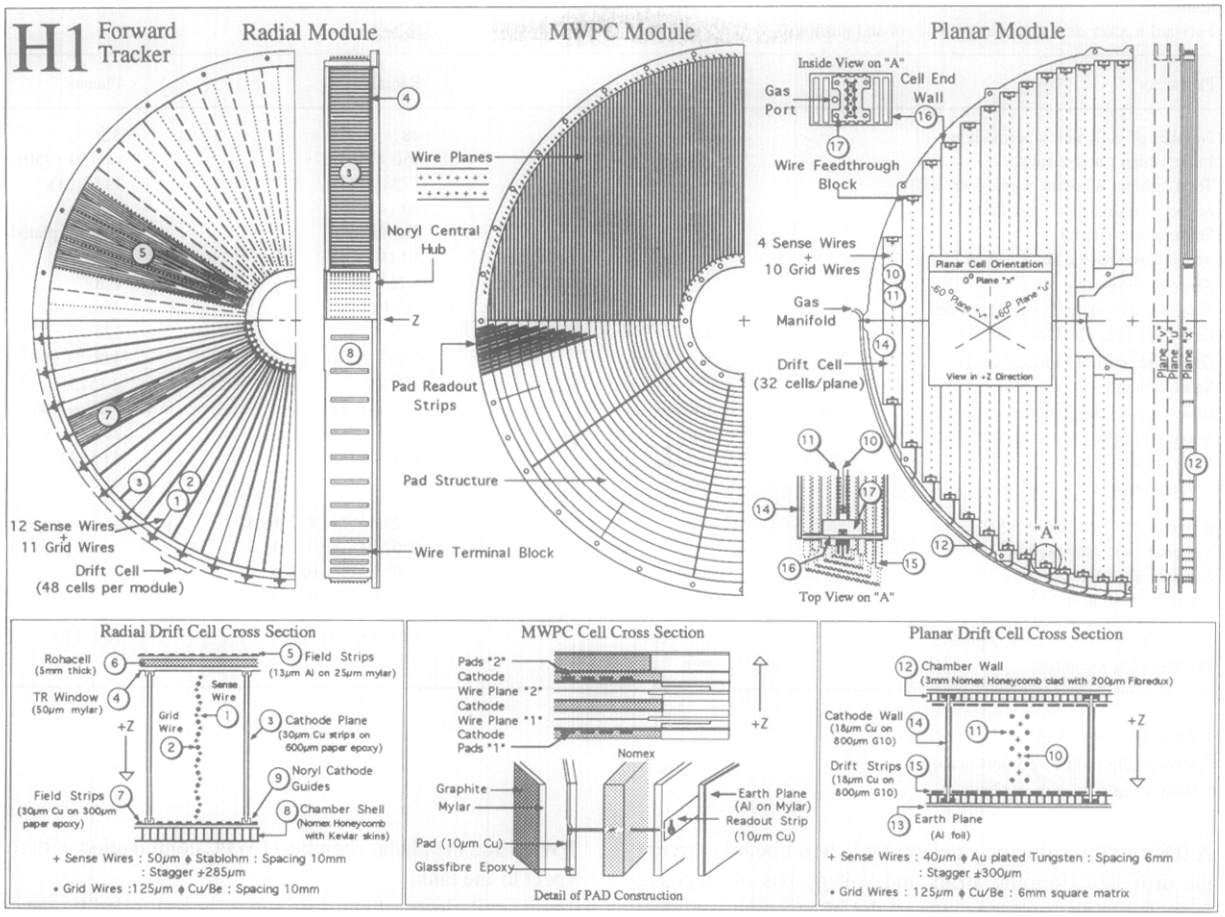

Fig. 10. Details of the forward tracker construction. Top: cross section in the r, z-plane and in the r, ϕ-plane showing the overall orientation of cells, wires and pads for each supermodule component. Bottom: details of cell construction.

commissioning each supermodule on a cosmic ray test facility the three supermodules were then bolted together, separated by thin gas tight Kapton windows, and the end faces closed with stiff plates made from a sandwich of 1.2 mm thick Al alloy and 17.6 mm thick Nomex honeycomb [24]. The final alignment of the whole FTD was measured using cosmic rays after installation into the H1 experiment. Water at constant temperature ($\pm 1°C$) is circulated around each tank section through copper pipes in order to maintain dimensional stability and provide cooling for the preamplifiers. As well as maintaining the relative alignment of the tracker elements and support for the various services – water, gas, cables, preamplifiers, position monitors etc., the tank provides an electromagnetically sealed environment and serves as the common ground for the chambers. The HV and signal cables access the tracker volume via the outer cylinder using hermetically sealed feedthroughs where they are grounded. The HV cables are also filtered before entering the tank.

Three different gas mixtures are used, two working gases for the chambers and one purge gas for the transition radiation (TR) volumes. Gas is fed into each supermodule volume via the U-shaped channels in the outer cylinder, two feed pipes and one pipe for local pressure sensing, a total of nine pipes per supermodule. Gas tightness is maintained by rubber O-ring seals at the outer and inner flanges. The gas is supplied at atmospheric pressure from three computer controlled closed loop gas circuits (see Section 2.6) which maintain gas purity and provide the accurate pressure control, ± 10 μbar required in order to prevent damage to the fragile TR windows. During HERA operation the oxygen level in all volumes has been kept to < 50 ppm.

The whole tracker is mounted on four insulated feet and rests on the cryostat rails in stress-free condition. It is electrically isolated from the central tracker and the cryostat.

2.3.1. *Planar drift chambers*

Each chamber is constructed as a self-supporting module containing 32 drift cells of identical rectangular cross section with wire lengths between 460 and 1410 mm as shown in Fig. 10. The chamber walls are formed from two circular discs with an outer diameter of 1.57 m and a central aperture of 280 mm diameter. They are composed of a low mass composite of Fibredux skinned Nomex honeycomb 3.4 mm thick, manufactured to be parallel and flat to within 100 μm.

Table 3
Forward tracker drift chamber parameters and positions.

Parameter	Unit	Radials	Planars
Number of cells per supermodule		48	32
Inner (outer) active radius	mm	150 (750)	≈ 150 (750)
Total number of sense wires (per cell)		1728 (12)	1152 (4)
Sense wire diameter (resistance)	μm (Ω)	50 (450)	40
Sense wire material		Stablohm[a]	W (Au plated)
Sense wire spacing Δz (stagger)	mm	10 (0.28)	6 (0.30)
Sense wire tension	N	1.75[b]	1.20[b]
Total number of grid wires (per cell)		1584 (11)	2880 (10)
Grid wire [Cu-Be(2%)] diameter	μm	125	125
Grid wire tension (surface field)	N (kV/cm)	2.80[b] (170)	4.00[b] 135)
Sense voltage	V	+2228	+1575
Bulk (grid) field gradient	kV/cm	1.2 (−6.9)	1.0 (−5.0)
Maximum drift distance (B = 0 T)	mm	50	28
Drift velocity (B = 0/1.14 T)	mm/μs	$\sqrt{3}$ × 37/37	43.5/42
Lorentz angle (B = 1.14 T)	deg	45	41.8
z planar (x), module 0/1/2[c]	mm	1324.4/1746.4/2168.4	
z planar (u), module 0/1/2 [c]	mm	1367.0/1789.0/2211.0	
z planar (v), module 0/1/2 [c]	mm	1409.6/1831.6/2253.6	
z radial, module 0/1/2 [c]	mm	1593.0/2015.0/2437.0	
$\sigma_{r\phi}(\sigma_r)/\sigma_{x,y}$ from track segments	μm (cm)	180–200 (3)	150–170
Double track resolution	mm	2	2

[a] Alloy from Ref. [18].
[b] 60% of the limit of proportionality.
[c] Position of first wire in plane.

A 0.8 mm thick double sided printed circuit board carrying the drift field forming strips and voltage bus on opposite faces is bonded onto one side of the honeycomb laminate. the drift cells are defined by parallel sets of copper clad PCBs, 0.8 mm thick by 32 mm high, mounted perpendicularly and bonded at 57 mm intervals into precisely machined slots in the honeycomb panels, resulting in a multiple box section structure of high mechanical strength and rigidity. The vertical PCBs constitute the cathode planes and define the maximum drift distance as 28.1 mm (for B = 0). Each cell contains four sense wires uniformly spaced in z and staggered alternately 300 μm each side of the median plane of the cell. Each sense wire is surrounded by four grid wires Cu–Be arranged on a 6 mm square matrix. Significant benefits arise from the double grid design including reduced cross talk, lower wire tensions, improved cell isochronicity, and reduced grid wire surface fields. All wires are crimped under tension in pins which are held in position by means of high precision extruded Noryl templates at each end of the cell. The principal source of error in the wire position ($\approx$ 20 μm) arises from the inherent inaccuracies in the crimping technique. The cell ends are closed by PCBs containing electrodes which cleanly terminate the electrostatic field of the cell. Aluminium foils covering the outer surfaces and connected to the tank provide electromagnetic isolation between the individual planes. A set of precision dowels fix the relative orientation of each plane (to < 0.06 mrad), the orientation of the planar supermodule with respect to the FWPC and the planar chamber/FWPC combination with respect to the tank.

The cell electric field distribution is controlled by seven different voltages: the sense voltage defines the gas amplification, the central strip voltage affects the sense field homogeneity, four drift strips and the cathode voltages determine the field gradient. The grid wires are grounded. All voltages are supplied directly from the HV supplies, after suitable fan out, without the use of resistor chains at the chamber. Field optimization and chamber operation are considerably aided by the fact that the double grid geometry produces a strong decoupling between the sense field (gas amplification) and the drift field. The operating conditions of the chambers for the gas mixture given in Table 7 are listed in Table 3.

The outer end of each sense wire is AC coupled into a current sensitive preamplifier (two drift cells per preamplifier) and the signals transmitted via 40 m of 50 Ω coaxial cable to the FADCs. Pulse profile (Q, t) analysis in the front end data acquisition system yields one drift time coordinate measurement perpendicular to the sense wire and one pulse integral measurement. Resolutions achieved on e–p data are typically 150–170 μm for the single point spatial resolution and < 2 mm for the double track resolution.

2.3.2. *Radial chambers*

The radial wire drift chambers cover 360° in ϕ with 48 separate sectors of 7.5° width. Each sector is a drift cell having 12 sense wires staggered alternately 287 μm each

side of a plane which bisects the sector. The sense wires, which are all parallel within one of these cells, are separated by 10 mm. Between adjacent sense wires, and positioned on the plane which bisects the sector, are field wires parallel to the sense wires and half way between them. All these wires are supported by crimp pins. At the small radius end (r = 152 mm), the crimp pins are mounted in a cylindrical Noryl hub, and at the large radius end (r = 760 mm), in Noryl templates precision bonded into the cylindrical wall of the composite structure which contains the whole 48 cells of the radial chamber as one rigid unit. The structure of these radial drift chambers has been described in Refs. [25–27].

The wedge-shaped drift cells are separated from each other by cathode planes which consist of voltage graded copper strips on each side of thin paper-epoxy material (PCB technology). The electrostatic field cage for each drift cell is completed by voltage graded shaped conducting strips bonded onto the plane inner surface of the composite structure (for the high z end of the wedge), and onto a complex window assembly, described below, which is affixed as a lid to the composite structure (for the low z end of the wedge).

The detailed design of this window, forming the plane surface of the radial chamber towards low z was determined by the requirement to detect the transition radiation (TR) entering the radial drift chamber. The X-ray component of TR produced by an ultrarelativistic charged particle contributes to an enhanced track ionization, hence to enhanced charge collected on one or more of the sense wires, provided that all ionization deposited anywhere in the cell is collected onto the sense wires and not onto field wires. The window of the radial chamber is thus designed to be as X-ray transparent as possible, and to ensure maximum X-ray detection efficiency as close as possible to it inside the drift cell. Because of the imperfect nature of the field grading close to the V shaped strips, ionization deposited within about 2 mm of the window cannot be collected onto the first sense wire. Such a loss of X-ray sensitivity is significant at the TR entry (low z) side of the radial chamber, where most of the X-ray photons photo-ionize the chamber gas. For this reason the V shaped strips to create the drift field are of aluminium on mylar and are supported on Rohacell [14] spacers which position them 5 mm from the thin mylar window which isolates the chamber gas volume. The effect of this window assembly on the electrostatics is to move the drift field inhomogeneities out of the sensitive gas volume. Then at the mylar wall closing the gas volume the drift field is uniform and parallel to the surface, except directly opposite the sense wire. Charging effects on the mylar window are then minimal, and the ionization collection efficiency on the first sense wire is optimal right to the edge of the gas volume.

Because all the sense wires are in the radial direction, a coarse determination of the radial position of a track may be made from charge division if a wire is read out at both ends. However it is not physically possible to have preamplifier cards at the small radius end. For this reason the sense wires of one 7.5° sector drift cell are connected at the inner hub to the sense wires of another 7.5° sector drift cell, actually 105° away in azimuth, so that when sense wires are read out at the outer radius charge division is possible along this double length of radial wire. Current sensitive preamplifiers are at each end of these sense wire pairs, each channel of which drives approximately 40 m of cable to the FADC system. Pulse profile (Q, t) analysis gives the drift coordinate perpendicular to the sense wire plane, and two pulse integral measurements Q_L and Q_R from the two ends give the radial position by charge division.

The spacing in the z direction between the sense wires of the radial chambers, between the three modules, and the sets of planar drift chambers and the radial drift chambers may be seen from Table 3. Concerning the azimuthal position of the radial chambers, the plane which bisects a 7.5° sector cell (and about which the sense wires are staggered) is at ϕ = 3.75° in the first module, at ϕ = 7.5° in the second module and at ϕ = 6.25° in the third module. The resolution achieved with the 50% argon, 50% ethane gas mixture used so far is 150–200 μm. The gas mixture which is intended to use for optimal detection of transition radiation is given in the following section.

2.3.3. *Transition radiators*

A passive array of polypropylene layers provides a sufficient number of dielectric interfaces for useful transition radiation (TR) X-ray emission. The dielectric constant, the layer thickness and the mark to space ratio of the polypropylene sheets determine the X-ray yield and the energy spectrum. For the values chosen the spectrum peaks around 6 keV for 20 GeV electrons. The interface between the TR and the radial wire drift chambers has been optimized for transmission of these X-rays. As described in the previous section the radial wire drift chambers are designed and operated both for optimal track point measurement and efficient X-ray detection. The combination of TR and radial wire drift chamber is designed for electron–pion discrimination, at the level of 90% electron acceptance with less than 10% pion contamination, up to 80 GeV for tracks passing through all three modules of the FTD. To achieve this, it is planned to operate the radial wire chambers with a gas containing xenon which has a high photoionization cross section at 6 keV. A 20% xenon, 40% helium, 40% ethane mixture satisfies the requirements of TR detection with acceptable charged track dE/dx ionization density, and also suitable drift velocity for the requirements of the drift chamber. Data taken with a radial drift chamber in a test beam at CERN have shown that the design discrimination between electrons and pions can be achieved with this gas [28,29].

The assembly of polypropylene sheets is self-supporting but is enclosed in its own gas envelope in order to isolate it from the gases used in the rest of the FTD. The helium–ethane mixture surrounding the polypropylene sheets is chosen to give the same partial pressure of helium as in the radial drift chamber. This is important because the interface

Table 4
Summary of drift chamber readout data.

Chamber	Branch no.	No. of crates	No. of channels	Raw data [kbyte]	(Q,t) data [kbyte]
Radial	5	9	1728	20.5	2.4
Planar	5	6	1152	28.5	4.1
CJC1 and CJC2	4	23	2640	33.2	5.4
COZ	4	1	96	3.41	0.5
CIZ	4	1	60	5.14	0.9
Forward muons θ	6	4	1024		

is the thin mylar TR window of the radial drift chamber section which could be damaged by pressure differences in excess of about 100 μbar.

2.4. Drift chamber electronics, readout, and front end data processing

2.4.1. Introduction

All drift chambers in H1 are connected to one of the three independent branches of the central data acquisition system (CDAQ). The analog signals are digitized and processed in a number of front end crates, the trigger connection is based on the H1 standard subsystem trigger controller crate and interface cards and local logic produces and distributes control signals to the front end crates. A master crate collects the complete data from the branch and sends it to the CDAQ. Crates for local data monitoring can be added. Fig. 11 shows the general layout of each drift chamber branch.

The drift chambers are distributed between the branches according to position in the detector. The inner and outer jet chambers and the inner and outer z chambers form branch 4 (CTD). The forward radial and planar chambers form branch 5 (FTD). The θ- and ϕ-chambers of the forward muon spectrometer form branch 6 (FMu). Table 4 shows the sizes of the various components, and the typical size of the zero suppressed digitizations (raw data) and processed summary data ((Q,t) data).

2.4.2. Operation of the readout

The analog signals from the preamplifiers mounted on the detector are received by 104 MHz FADC cards which continually digitize and store the data – at this point we are recording data at a rate of over 600 Gbyte/s over all drift chambers. On receipt of a first level trigger (L1) signal the digitization is stopped so that the data recorded in the FADC card memory includes, for each detector, all digitizations which could have occurred between the time of the event and the maximum possible drift time for that chamber.

At a second level trigger (L2) signal the full 2.5 Mbytes of raw data for an event is copied by the scanner controller cards into the second level buffer at a speed of 3.3 Gbyte/s. At a third level trigger (L3) signal, the processor card in the FADC crate reads the data from the scanner, and writes an off-line format data bank into an intermediate buffer which contains blocks of significant, zero suppressed data with an event size of approximately 100 kbyte. The output is written into a triple ported buffer memory on the intercrate connection (VIC 8251 [11]). When a complete event is available from all front end crates the master processor collects the data from this buffer memory and writes the complete event to the multi-event buffer of the optical fiber VMEtaxi link (see Section 7.1.2 of Ref. [1]).

2.4.3. Amplifier and FADC

The sense wires of the tracking drift chambers are connected to amplifiers either at one or at both wire ends. The eight-channel amplifier cards are mounted directly on the chamber vessel. The sense wire and the grounded potential wires serve as differential input. The sense wire is at positive HV and therefore it is coupled to the amplifier via a capacitor (1.5 nF). The sense wires (in some chambers) and amplifier are protected by a spark gap, and a pair of crossed diodes to ground. Each amplifier channel consists of two stages of video amplifiers. The amplification is large enough so that no further amplification is needed on the readout card. This gives optimum noise rejection and minimizes the influence of pick-up on the cable to the readout card. The amplifier card has two test inputs which allow the application of test pulse signals to the inputs of odd or even amplifier channels.

The 9520 signals from the drift chamber are digitized by F1001-FADCs [30]. The sampling frequency is 104 MHz, generated by an oscillator phase locked to the bunch crossing clock of the HERA storage ring of 10.4 MHz. The differential outputs of the amplifiers are connected to the FADC cards with a multi-coaxial cable of about 28 m length. This cable also carries the power and test lines to the preamplifiers. The FADC-chips used have a resolution of eight bits [30]. The combined signal is fed to the FADC chip through a transformer eliminating DC offsets and via a resistor network that includes feedback of the input signal to the voltage reference, providing a nonlinear response with 8 bit accuracy for small signal amplitudes and a 10 bit dynamic range. Each FADC-chip is connected to one 256 byte deep memory which serves as circular buffer. During the active sampling phase of the FADC system signals are continuously digitized and stored in the memories. This recording process is stopped by a trigger signal that freezes the history over 2.5 μs in the memory. Sixteen FADC-channels are housed on one F1001-card and up to 16 F1001 cards are housed in a F1000 crate. It has a VME backplane used for fast 32-bit wide readout of the digitized signals from the FADC-memories. The signal risetime at the sense wire is a few ns. It is deliberately degraded by the amplifier band width, cables, and coupling transformer to 18 ns (20% to 80% of pulse amplitude) at the input of the digitizing FADC. This is the optimum for a time measurement with a FADC sampling at 100 MHz.

[11] VICbus, VME Inter-Crate Bus, ISO/IEC JTC 1/SC26.

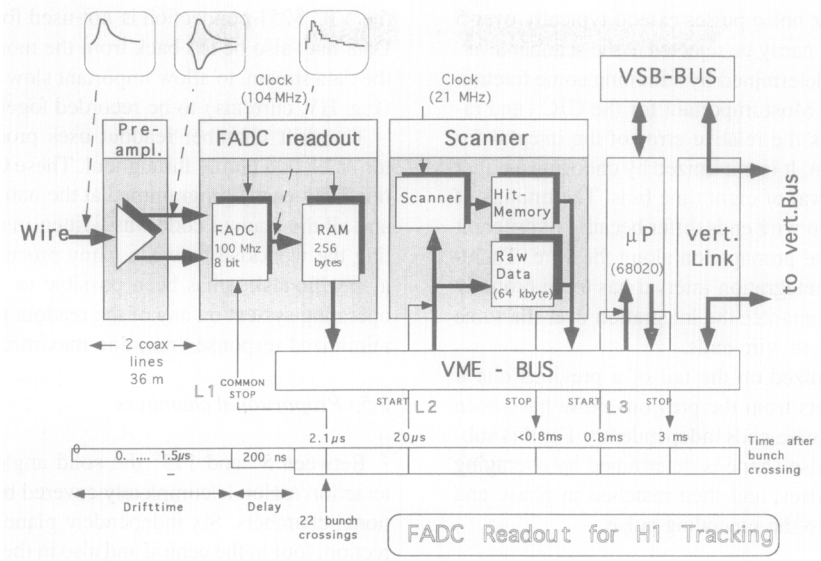

Fig. 11. FADC readout system for drift chambers.

2.4.4. The scanner and the front end processor

In each F1000 front end crate there is an M1070 scanner card that acts as a sample controller for the FADCs, and provides fast readout and zero suppression of the FADC data. The scanner supplies the 104 MHz clock to the FADC cards, and at a L1 trigger gates this clock such that the circular buffers of the F1001 cards contain the required time segment. At a L2 trigger signal it copies the data from the FADCs into a local buffer in a series of synchronous bursts over the VME bus, in this way a transfer speed of 80 Mbyte/s is achieved, and the data for a full crate can be copied within the 800 μs requirement of H1. During the copy the data is compared with programmable thresholds and any significant transition (presently two subsequent time bins above or below threshold) is recorded in the hit table.

At a L3 trigger signal the scanner interrupts the front end processor (24 MHz FIC 8231[12]) present in each F1000 crate. The interrupt handler reads the hit table from the scanner, calculates the required blocks of raw data, and copies these blocks into a multievent raw data buffer in an offline format data bank. Each block includes four pre-samples before the hit starts to allow dynamic calculation of the pedestal, and blocks are merged in cases where a block would influence a subsequent block on the same wire. An output bank is written into a multievent output buffer in the memory of the VIC 8251 interconnect card, using the VSB bus connecting the processor and the interconnect, since the VME bus may be occupied by the scanner reading a subsequent event. The input raw buffer and output buffer both typically hold 30–40 events, and this allows derandomization over many events of the large range in processing times caused by localized high track density.

[12] Creative Electronics Systems SA, Fast intelligent controller FIC 8230/8232, Geneva, CH, 1987/1992.

2.4.5. Determination of charge and time (Q, t)

The relevant parameters of a signal pulse from a drift chamber wire are signal timing (t) and the pulse integral (Q). These signal parameters are determined by a program which runs on the L4 farm (see Section 5.5 of Ref. [1]). In this way the amount of raw data is reduced by a factor of about 5. The zero suppressed data provided by the scanner are treated in several steps. For the CJC, CIZ, COZ and the radial chambers the first three steps consider the data of both wire ends separately, while the further steps use the combined information.

In the (Q, t)-algorithm the FADC data are first linearized. The leading edge of a new pulse is found by a search for a maximum in the difference of successive samples above the threshold. The average of the six digitizations before the pulse start is used to evaluate the pedestal to be subtracted from the pulse. Hits from the two ends of a wire are combined if the leading edges differ by less than or equal to two clock bins.

The essential information for the drift time determination comes from those electrons which arrive first at the sense wire and which are produced along the track in the region tangential to the isochrones. These electrons contribute to the sharp rise of the pulse, which is, however, smeared out by diffusion, chamber capacity, and amplifying electronics. The remaining off-tangential electrons arrive at later times and fluctuations of their ionization density influence only the trailing edge of the pulse, otherwise determined by the differentiating electronics.

The drift time is determined by chamber specific algorithms. For the CJC e.g., the time at half the full amplitude is determined by linear interpolation, averaged over both wire ends and used with the average risetime to extrapolate to the arrival time of the first electrons, taken at 10% of the pulse amplitude. The average pulse consists of about 20 digitiza-

tions, while 10.4 MHz noise pulses extend typically over 5 bins and can therefore partly be rejected at the scanner level. The pulse integral is determined by summing some fraction of these digitizations. Most important for the CJC (and radial drift chambers) is the relative error of the integral for the $z(r)$ determination. It is minimized by choosing a rather short integration interval of eight time bins. The timings of the pulses from the two wire ends differ because of different cable length and signal propagation along the wire. Therefore the phase of the integration interval has to be properly adjusted in order to guarantee the integration over the same part of the pulse on both wire ends.

If a pulse is recognized on the tail of a previous one it is analysed after effects from the previous pulse have been subtracted on the two wire ends independently. For this subtraction a standard pulse shape is determined by averaging a large number of pulses, and then matched in phase and normalised in height to the preceding pulse.

2.4.6. *Implementation*

The subsystem trigger controller crate (STC, [31]) provides a standard interface to the central trigger electronics (see also Section 5.3.5 of Ref. [1]). The STC in the DC readout is supplemented by a 104 MHz phase locked loop (PLL) card providing an accurate (± 1 ns) clock and a logic card acting as sequence controller. Although responses from the scanner could by simple combination be used directly to respond to the central trigger, inclusion of the logic card in the path allows better overall performance by overlapping some stages of processing with refill and other delays of subsequent events. This places much of the response time of the DC systems in second or even third order dead time, and allows the DC systems to be run at almost full throughput with little or no actual dead time.

The master crate contains interfaces to the CDAQ (VMEtaxi link) and to other crates in that branch (VIC 8251) consistent with the common H1 architecture (see Section 7.2.1 of Ref. [1]). On startup, the master processor loads all other processors with code and data stored in nonvolatile ram. Once the other processors are running, all communication is made through the buffer memory of the VIC boards connected to each of the remote processors. During a run the master processor operates asynchronously, waiting for an event to be signalled by the trigger processor, and then polling the front end processors until the complete event is ready to be built. The events are not buffered or processed by the master processor.

A monitoring crate provides access to the readout branch for chamber specific control and monitoring systems. A small fraction of the event data can be passed to the monitoring crate for local monitoring, especially that which requires raw data that might be unavailable in the CDAQ monitoring systems. Data is collected from a dedicated memory in the master crate using a differential VSB extension [13] – the VIC 8251 connection is not used for technical reasons. Data may also be fed back from the monitoring system into the data stream, to allow important slow control information (e.g. HV, currents) to be recorded together with the event.

The drift chamber readout uses processors of the Motorola 68000 family throughout. These CISC processors are relatively easily programmed at the native instruction level, and all the readout code was written in assembler. By splitting the workload between many processors each fulfilling a specific task it has been possible to avoid the use of an operating system on any of the readout processors. This has minimized response times and maximized performance.

2.5. *Proportional chambers*

Between 5° and 175° the solid angle seen from the interaction region is completely covered by multiwire proportional chambers. Six independent planes in the forward direction, four in the central and also in the backward direction serve three different functions: to deliver a fast timing signal with a time resolution better than the separation of two succeeding HERA bunch crossings, to provide moderately accurate space points for charged particle track reconstruction at the first level trigger and lastly to add an accurate track element in the backward direction, where the drift chambers fail to provide enough space points.

The planar forward chambers (FWPC) are interspaced between the drift chambers of the FTD described above and are exposed to high particle rates increasing towards the beam pipe. Hence minimum overall thickness and minimal amount of material traversed, sufficient ageing prospects, and cathode pad size adapted to increasing rates near the beam pipe became the primary design criteria. These points do also apply for the two cylindrical chambers in the central region. The inner one (CIP) is closest to the interaction region and covers the largest solid angle. In order not to degrade the track reconstruction of the surrounding drift chambers, the CIP and its outer partner (COP), were fabricated with low mass materials and a narrow active gap. Since the main purpose of the FWPC, COP and CIP is to provide space points for the first level trigger, a pad segmented cathode readout was chosen with graphited surfaces as in other chambers built for high rates [32,33]. From the reconstructed tracks the event vertex can be deduced and other detector data such as calorimeter and muon information can be validated. Since the trigger logic requests three space points per track, spurious background hits from uncorrelated noise and synchrotron radiation are removed.

In the backward direction the reconstruction of the scattered electron in low momentum transfer events calls for an accurate track segment. This is given by the signals from the four differently oriented anode wire planes of the backward chamber (BWPC). Several wires can be combined for triggering purposes. Standard planar chamber construction techniques sufficed here, since more than one radiation length of electronics and cables from the central tracker separate

[13] The VME Subsystem Bus (VSB) specification, IEEE standard 1096.

the BWPC from the interaction region. The BWPC covers the front surface of the backward electromagnetic calorimeter (BEMC) and hence also serves to discriminate electrons and photons.

The properties of all four chamber types are summarized in Table 5. The front end electronics and readout system is identical for all chambers.

2.5.1. Forward proportional chambers (FWPC)

Each of the three chambers in the forward tracker volume consists of two wire planes interleaved with three cathode planes. The gap between the two adjacent cathode planes is 4 mm wide, as indicated in Fig. 10. All chamber frames are made of glass fiber epoxy. To reduce the mass in the active area a laminated structure consisting of the following layers is used: 100 μm graphited mylar foil serving as cathode plane, 250 μm printed circuit board carrying 10 μm Cu readout pads, 3.3 mm Nomex [24] mesh, another 250 μm printed circuit board covered with 10 μm Cu for the strips leading from each pad to the preamplifiers on the chamber ends, a further 100 μm of graphited mylar foil in the central plane or aluminized mylar foil on the external planes for electromagnetic shielding. The graphite layers are produced by spraying a mixture of DAG 5466/DAG 213 [34] at 5 bar giving an initial surface resistivity of 1 M$\Omega/\square$, which was reduced to 300 k$\Omega/\square$ by polishing. Each chamber is strengthened by a backplane, 12 mm thick, with two layers of 250 μm glass fiber epoxy sandwiching 11.5 mm Nomex. The overall thickness is 1.7% of a radiation length. The mechanical tensions of the wires and the foils are supported by 24 and 8 axial rods on the external and internal frames, respectively. The anode planes contain gold plated tungsten wires ($\oslash$ 25 μm) spaced by 2.5 mm. They are crimped on pins fixed on the frames. Each wire is connected to the following one through 1 MΩ resistors and to ground through 330 nF capacitors. Groups of 15 wires are connected to separate HV lines, which allows degrading of malfunctioning sectors if necessary. The cathode pads are ring shaped and cover an azimuthal angle of $\pi/8$ each, except for the four outermost of the 20 rings where they cover $\pi/16$. The radial pad width increases with radius in geometrical progression from 18 to 37 mm. Two consecutive cathode planes are offset by one half of a ring, such that the effective polar angle resolution is halved: $r_{\min,i+1} = 1.0382 r_{\min,i}$ with $167.5 \leq r \leq 750$ mm. The Pluto gas mixture (see Table 7) was chosen, because the FWPC share their gas volume with the forward drift chambers and transition radiation detectors.

A track crossing all three or at least two modules of the FWPC has to fall into the polar angle range $6.6° \leq \theta \leq 18.0°$ or $5.1° \leq \theta \leq 21.6°$, respectively. For such tracks an effective timing resolution of 20 ns (FWHM) and 47 ns (base width at 10% of the maximum) was measured using H1 data, well below the required resolution to separate two bunches.

2.5.2. Central proportional chambers

CIP The laminar structure of the CIP called for special construction techniques which are described in detail in Ref. [35].

The double layer of chambers consists of three concentric cylinders. During construction each chamber cylinder was formed on a steel mandril milled to a precision of 25 μm over the full length. The innermost layer of the first cylinder, a 25 μm thick Al-foil provides the electromagnetic shielding. The next layer – 2 mm thick Rohacell foam [14] glued onto the Al-foil with 20 g/m^2 epoxy-glue[14] – gives the chambers the necessary rigidity. The Rohacell surface was polished, and a second 25 μm Al-foil glued to it served as the inner cathode. After cutting the cylinder to the right length the Al-foils were connected to Cu-foils, at the ends and the glass fiber epoxy [6] end flanges were added. These carry the printed circuit boards for the anode wires, which are supported further by glass fiber epoxy rings at $\frac{1}{3}$ and $\frac{2}{3}$ of the chamber length. The active gap is 6 mm wide. The anode wires (gold plated tungsten, $\oslash$ 25 μm) were transferred to the axially prestressed cylinder from planar frames.

The middle cylinder forms the outer cathode of the inner chamber and the inner cathode of the outer chamber. Here the innermost layer, a 20 μm Kapton foil is coated with high resistive graphite (400 k$\Omega/\square$) on one side and 0.5 μm Al on the other side. The Al layer is segmented into pads on which the induced charge on the cathode is collected. The graphite layer in front guarantees a fast disappearance of the accumulated ion charge. This has the advantage that the readout wires of the pads can be mounted outside the gas volume. After several tests on prototypes [35] the graphite layer in the final chamber was produced by spraying a mixture of DAG213, DAG305 [34] and isobutylmethylketon (IBMK) in a ratio of 20 : 1 : 7 onto the Kapton foil with 3 bar. The cathode foils are again backed by 2 mm Rohacell. The readout wires (150 μm Al) are embedded into 250 μm deep grooves in the Rohacell running along the z-axis from the chamber end ($-z$ side) to a hole centered over the pads. The wires were contacted onto the pads with silver paint and soldered at the flange end. Another 20 μm thick Kapton foil with Al-coating is glued onto the Rohacell, which forms together with the wires a wave guide of $\sim 70\ \Omega$ impedance. The Kapton foil again backed by 1 mm Rohacell with a polished surface is covered by another 25 μm Al foil serving as the cathode for the outer chamber. End flanges and connections are similar to those of the first cylinder and the sequence of layers for the third cylinder is identical to that of the second.

Gas sealing is provided by two O-rings at the end flanges (2 mm $\oslash$). The overpressure in the chambers has to be kept small and needs to be monitored carefully in order not to distort the gap. The two chambers have independent gas

[14] Araldit: epoxy glue manufactured by CIBA-Geigy AG, Basel, Switzerland.

Table 5
Proportional chamber parameters. The separate columns for CIP and COP refer to the two planes, for the FWPC to the whole module containing two planes.

	Unit	CIP (inner/outer)	COP (inner/outer)	FWPC (no. 1/no. 2/no. 3)	BWPC
Active length $\Delta z/\Delta r$ [a]	mm	2190	2172	583	515
Active zone starts at z/r [a]	mm	−1125	−1107	167	135
Mechanical length $\Delta z/\Delta r$ [a]	mm	2254	2262	665	597
Total length $\Delta z/\Delta r$ [a, b]	mm	2467	2360	665	708
Thickness $\Delta r/\Delta z$ [a, c]	mm	21.5 (25)	30 (34)	40	52 (60)
Chamber starts at z/r [a,b]	mm	−1376	−1270	135	110
Position of first anode r/z [a]	mm	157/166	501/514	1451/1874/2297	−1423
Number of anode planes		1	1	2	4 [d]
Number of wires		480	1574/1615	724	2496
Wire separation	mm	2.1/2.2	2.0	2.5	2.5
Gap width	mm	3.0	4.0	4.0	4.0
Number of cathode pads		480	288	384	
Cathode resistivity	kΩ/□	≈ 400	≈ 200	≈ 300	≈ 400
Length of pad $\Delta z/\Delta r$ [a]	mm	36.6	120	13 to 54 [e]	
Width of pad $\Delta\phi$	deg	45	22.5	45 (22.5) [f]	
Anode wire tension	N	0.63	0.60	1.5	0.98
Plateau length	V	200/250	200	300	200
Plateau starts at	V	2425/2375	2900	1900	2800

[a] First coordinate for CIP and COP, second for FWPC and BWPC.
[b] Inclusive preamplifiers.
[c] In the active zone (and at end flanges).
[d] The anode wires of each successive plane are rotated by 45°.
[e] Width increases with radius, $\Delta r_i = 0.0782 r_i$, where r_i is the inner radius of the pad.
[f] Only for the four outermost of the 20 radial pads.

distributions and are rotated by $\pi/16$ in ϕ with respect to each other, thus halving the eightfold segmentation of each chamber at the trigger level by requiring coincidence of two planes. In z there are 60 pads of 36 mm width in each ϕ sector.

With the gas mixture given in Table 7 the single pad efficiency measured in a test beam was 99%, while at HERA 94 ±2% was measured with extrapolated jet chamber tracks. From the measured pulse height distributions the gap variations for this light chamber were deduced to be less than 0.2 mm. The measured test beam time resolution (FWHM 21 ns) compares well with the results at HERA. This result converts into a 2% probability to register a given pad with the wrong (neighboring) bunch crossing. The probability for crosstalk, i.e. the probability to register signals also in neighboring pads in z and ϕ and the inefficiencies across the pad boundaries are discussed in detail in Ref. [35]. The average number of active pads for crossing angles larger than $\theta = 40°$ in a test beam (1.4) compares well with what is observed at HERA.

COP The construction of the COP follows closely that of CIP in those aspects concerning the sandwich structure (see Fig. 12). Steel mandrils machined to a precision of 60 μm and appropriate to the larger chamber radii were used. To improve the stability of the sandwich structure, the thickness of the core material (Rohacell) was increased to 4 mm. The graphite cathodes (7 m^2 area per chamber) are produced with a screenprinting technique using a resistor ink solution, rather than spraying. The ink [15] has a resistivity of 170 kΩ/□ for a 15 μm layer and was diluted with a solvent monobutylic ether of ethylene glycol in a ratio of 1 : 3. A surface resistivity of 200 kΩ/□ was obtained after polymerization at 120°C during 1 h. The cathode pad structure is provided by gluing patches of 25 μm Kapton coated with 1 μm Cu to the back side of the graphite cathodes, giving an 18-fold segmentation in z and 16-fold segmentation in ϕ. The cathode layer is backed by 3 mm Rohacell, in which 50 μm diameter Cu wires are embedded. A 25 μm Kapton foil coated with 1 μm Cu put on top of the previous layer constitutes with the copper wires the transmission line that carries the chamber signals to the $-z$ end of the chamber. This layer is then backed by 2 mm Rohacell. The Vetronite (G10) end flanges of the chamber support the printed circuit boards to which the anode wires (≈ 1600 per chamber) are soldered and assure the 8 mm chamber gap size. They form the only rigid structure to which the gas distribution and preamplifiers are connected. The three cylinder sandwiches are assembled in vertical position. Pulse height measurements showed that the gapsize variation is of the order of 0.3 mm [36].

Despite its three times larger radius the COP is only moderately thicker than CIP (0.18% radiation length instead of 0.14%). The efficiency plateau is reached at 500 V above the

[15] R-4825 Johnson Mathey, Conductive Adhesives and Coatings.

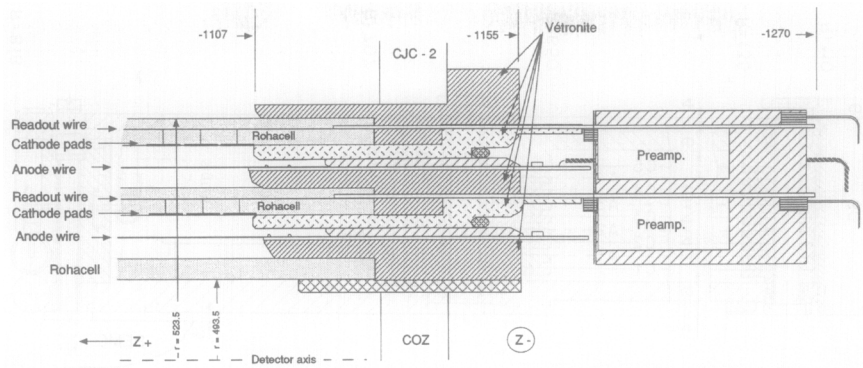

Fig. 12. Longitudinal cross section and details of the COP.

CIP plateau with the same gas mixture, a consequence of the larger gap. While in test beams CIP and COP behaved similarly, at HERA the noise level in COP is slightly higher due to more difficult grounding. This requires a higher threshold setting and leads to a typical efficiency of $92 \pm 2\%$. The timing resolution is similar to that of the other chambers.

2.5.3. Backward proportional chamber (BWPC)

The BWPC is equipped with five graphited cathode planes ($50\ \mu$m Mylar foil) and four anode wire planes. It is the only chamber in H1 in which the cathodes are not segmented and the anodes are read out. The graphite coating was fabricated with the same technique as described for CIP. The wires and the foils are stretched between a 23 mm wide inner and a 67 mm wide outer ring of glass fiber epoxy (G10). These rings are 4 mm thick and sustain the active gap of 8 mm per chamber, as indicated in Fig. 13. The wires are strung every 2.5 mm, but signals from two neighboring wires are fed to one preamplifier. The wire orientations are vertical, horizontal and $\pm 45°$ for the four layers. Gas sealing and structural support for the assembly is provided by G10 front and back planes of 10 mm thickness milled down to 6 mm in the active zone. The latter starts at an inner radius of 135 mm and ends at 650 mm, while the whole chamber occupies the region between $r = 110$ mm and $r = 818$ mm. The BWPC therefore covers polar angles of $174.5 \geq \theta \geq 155.5°$. The space points given by the BWPC contribute 0.5 mrad to the angular resolution, of the same order as the multiple scattering in the material in front of it. For high energy electrons an efficiency of 87% per plane was measured from extrapolated CJC chamber tracks. When requiring three out of four planes to be hit in coincidence with the BEMC an efficiency of 98% is obtained.

2.5.4. Proportional chamber electronics and readout

A schematic picture of the frontend electronics is shown in Fig. 14. The cathode pad signals (CIP, COP, FWPC) and anode wires (BWPC), respectively are preamplified directly on the chambers. A differential signal is then transmitted through a 35 m long cable to the electronic trailer. Each cable contains 16 signal pairs and is connected to a receiver card containing shaping amplifiers, followed by discriminators with computer controllable thresholds. The characteristics of the preamplifier–shaper chain are listed in Table 6. The overall gain can be adjusted to chamber pulse height between $1.3\ \mu V/e$ and $26\ \mu V/e$ by means of a resistor on the receiver card. A typical equivalent noise charge is about $3800e$, for a chamber capacity of 60 pF.

The digitized signals are synchronized with the HERA clock and stored in a pipeline constructed from the same gate arrays as used in the muon system (see Section 4.1.4). Upon a first level trigger decision (L1-Keep), the pipeline clock is stopped. A second level trigger decision (L2-Keep) then initiates the data readout. The synchronized pad signals are furthermore made directly accessible to the z-vertex and forward ray trigger (see Section 5.3.1 of Ref. [1]). Test registers allow controlling the readout and trigger chains.

The MWPC readout system, an independent branch (no. 7) of the H1 data acquisition system (see Fig. 22 of Ref. [1]), is responsible for reading 3936 channels, originating from 270 receiver cards in 15 crates, and some decision data from the two first level triggers. In addition to the frontend crates, the system consists of two standard VMEbus crates and one STC crate [31] in a configuration common to all H1 subsystems (see Section 7.2.1 of Ref. [1]).

The frontend crates are equipped with a customized "EasyBUS", which is essentially a simplified 16 bit wide VME bus with a 64 kWord address space lacking any interrupt capabilities but with added analog and ECL signal lines. The latter are used to distribute the clock and L1-Keep signals. The analog lines allow measuring the digitization thresholds loaded to the discriminators through an ADC located on a crate controller (CC) card. The primary task of the CCs is however to connect the crate to a branch driver card (BDC) residing in the master VME crate. The BDC-CC combination maps the EasyBUS address space into the VME frame [37].

Each BDC is directly connected to the STC and contains a DMA (direct memory access) controller and a 4 kbyte deep FIFO (first in, first out) buffer. An L2-Keep signal can thus initiate a frontend data transfer to the master crate

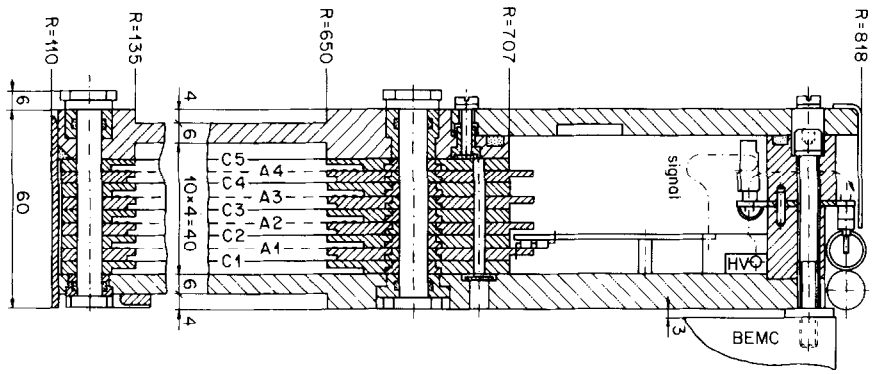

Fig. 13. Cross section through the backward proportional chamber.

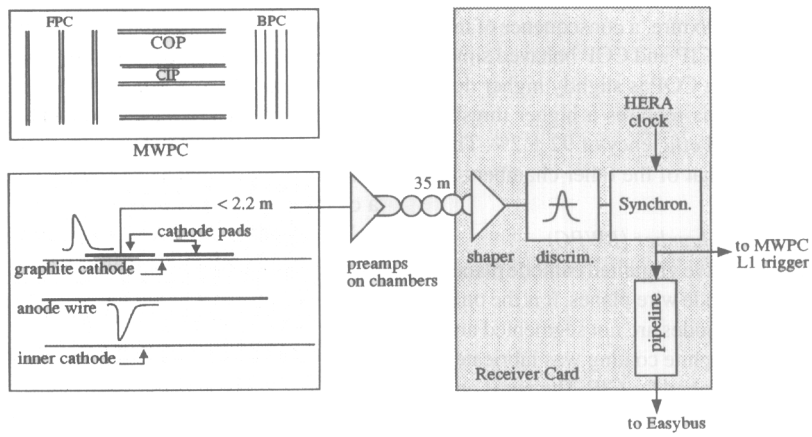

Fig. 14. MWPC front end electronics and read-out system.

Table 6
Characteristics of the MWPC preamplifier and amplifier-shaper.

Preamplifier		Amplifier-shaper	
Differential gain	65 nV/e	Maximum differential gain	400
Rise time (10–90)%	2 ns	Rise time	9 ns
Fall time (10–90)%	20 ns	Pulse width (FWHM)	16 ns
Input impedance	64 Ω	Maximum output voltage	3.2 V
Output load	2 × 50 Ω	Overload recovery	
Dynamic range	±300 mV ($\approx 10^7 e$)	$V_{in} < 5V_{in,sat}$	70 ns
Power supply	±3.5 V (22 mW)	$V_{in} = 30V_{in,sat}$	170 ns
Size	25 × 10 × 2 mm^3	Power supply	+5, −5.2 V (320 mW)
		Size	36 × 3 × 6 mm^3

without processor intervention. The maximum transfer speed is 4.5 Mbyte/s. Each of the six BDCs installed in the MWPC area can control eight frontend crates. The latter are grouped into pairs to make use of the 32 bit wide data path of the VME bus. To optimize readout speed, between two and six crates are connected to one BDC.

The first order dead time is determined by the front-end transfer to the BDC as long as the BDC FIFO are not saturated. The saturation rate is given by the average time spent by the data acquisition processor per event. Details of the data acquisition program are available in Ref. [37]. An average time of 4.2 ms per event is needed. This corresponds to an average of 237 hits in 10 bunch crossings.

2.6. Gas systems

To operate the nine different tracking detectors nine separate gas circuits are necessary, with different gas mixtures, flows, and demands on purity and overpressure control. For the forward chambers and CJC closed circuits are used while

Table 7
The different circuits of the gas systems.

Detector	Gas volume [l]	Gas mixture +additives: volume ratio [%]	Pressure relative to atmosphere [hPa] typ.	max.	Flow rate [l/min] typ.	max.	System circuit type
Planars+ FWPC	~ 900	$Ar/C_3H_8+C_2H_5OH$ (90/10)+1	0.15 ± 0.10	1	1.3	3	I closed
Radials	~ 700	phase I: Ar/C_2H_6 (48/52) phase II: $Xe/C_2H_6/He$ $+C_3H_7OH$ (20/40/40)+1	0.15 ± 0.10	1	1.0	2	
Radiators	~ 500	He/C_2H_6 (60/40)	0.25 ± 0.10	1	0.1	1.5	open
CJC1	~ 1140	phase I: $Ar/CO_2/CH_4$ (89.5/9.5/1)	1.5 ± 0.5	5	1.5	3	II closed
CJC2	~ 3080	phase II: $Ar/C_2H_6+H_2O$ (50/50)+0.5	1.5 ± 0.5	5	4.5	9	
CIZ	~ 55	$Ar/C_2H_6+H_2O$ (70/30)+0.2	0.15 ± 0.10	1	0.1	0.6	III open
COZ	~ 240	$Ar/C_2H_6+C_3H_7OH$ (48/52)+1	0.15 ± 0.10	1	0.2	0.8	
CIP	~ 30	Ar/C_2H_6/freon12+H_2O (49.9/49.9/0.2)+0.2	0.15 ± 0.10	1	0.07	0.6	
COP	~ 150	Ar/C_2H_6/freon12 (49.9/49.9/0.2)	0.15 ± 0.10	1	0.1	0.6	
BWPC	~ 120	Ar/C_2H_6/freon12 (49.9/49.9/0.2)	0.15 ± 0.10	1	0.1	0.6	

CIZ, COZ, CIP, COP and BWPC are flushed with premixed gases in open circuits. The main parameters of the gas systems are given in Table 7.

2.6.1. Gas circuits

The simplified diagram of the gas circuit of the planar chambers shown in Fig. 15 illustrates the typical features of the gas systems. The system is distributed over three levels, the supply outside the H1 hall, the control room on the first underground floor and finally the distribution rack on top of the electronics trailer near the detector. At the latter point the gas inlet flow for each detector is adjusted by mechanical flow meters and for some chambers split into several streams for further distribution as shown in Fig. 15. The static pressure of chambers relative to atmosphere is measured with sensors in the μbar range. In order to avoid too large hydrostatic pressure differences between chambers and sensors, the latter are also located at this point.

From the inlet manifold either pure or premixed gases can be fed into the circuit. Flushing is done by gently filling helium or argon via the two flow meters FL1-1 and FL1-2 into the chambers, while the chamber gas at the same time is sucked out by the membrane pump CP1-1. To hold the chamber pressure during the whole operation within adjustable tolerances of about ± 100 μbar, the solenoid valves SV1-2 and SV1-3 will be either opened or closed depending on the actual pressure inside the detector. As seen from Fig. 15, the ingoing and outgoing flows of the chamber gas are split into two paths, one of them containing instruments

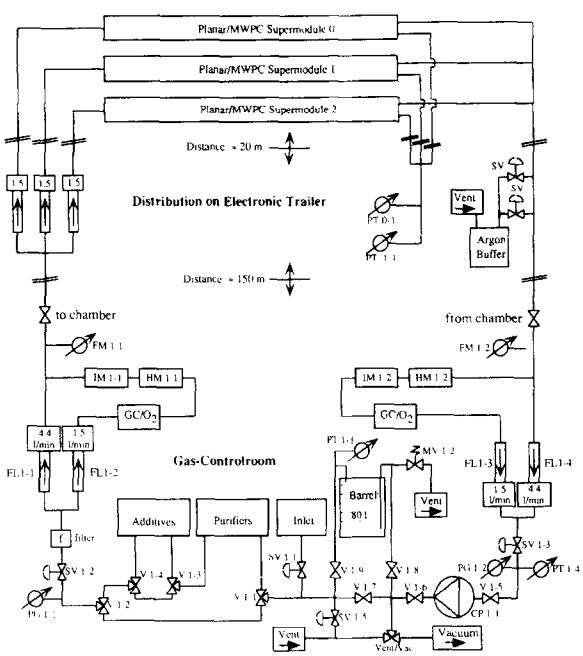

Fig. 15. Layout of the closed circuit gas system for the planar drift chambers. CP: circuit membrane pump, FL: mechanical flow meter, FM: electronic flow meter, GC: gas chromatograph, HM: hygrometer, IM: infrared meter, MV: mechanical safety valve, O_2: O_2-meter, PG: mechanical pressure gauge, PT: electronic pressure transducer, SV: solenoid valve, V: mechanical two- or three-way valve.

for continuous gas analysis like infrared meters, a hygrometer and a gas chromatograph in combination with an oxygen trace analyzer. The filling of the chambers proceeds in a similar way as the purging either with premixed gas or by introducing approximately the right proportions of first the non-flammable and later the flammable gases. Then inlet and vent valve are closed and the circuit is switched from the open to the closed mode. The gas circulates through the barrel, the purification units, if needed, through an alcohol or water bath, and through the chambers. Since the purification units absorb part of the gas components, particularly hydrocarbons, a readjustment of the mixture is necessary after typically one day of circulation. To maintain the correct mixture gas can be added to the barrel manually. Repeated circulation for several days, especially when additives like water or alcohol are used, leads then to a homogeneous gas mixture constant in time.

So far three types of additives are used. Some mixtures contain 0.2% freon 12 as one of the components of the premixed gas. To other delivered mixtures alcohol (typically 1%) or water (typically 1000 ppm) is added by passing the gas over a bath of the cooled or frozen liquid stored in a refrigerator in temperature controlled reservoirs. The admixture is adjusted by varying the bath temperature.

2.6.2. Purification and analysis

The closed loop circuits are supplied with purification units for removing oxygen, water and low concentrations of higher organic compounds. For oxygen removal 2 kg BTS-catalyst R3-11 [16] in the reduced state is used as an absorption agent and oxygen levels as low as 20 to 40 ppm have been reached over long time periods. Optimal oxygen removal is obtained with catalyst temperatures of 100°C to 150°C. However in the case of ethanol admixture, as is foreseen for the planar chambers, the alcohol will be cracked [38,39]. Working at temperatures below 80°C circumvents this problem at the cost of a lower oxygen capacity for the purifier of only about 6 to 15 l [O_2/kg (catalyst)]. A similar problem arises when isopropanol is added to the chamber gas, which is recommended for Stablohm wires and the radial chambers [25,40]. Since the isopropanol molecule is more fragile than the ethanol molecule, it is cracked even at room temperature into hydrogen and acetone by the catalyst [41]. Use of other O_2-purifiers working at low temperature like Oxisorb [17] and palladium-catalyst [18] give similar problems with alcohol-additives, especially with isopropanol, so that up to now isopropanol could not be used in the closed circuit of the radial chambers.

At room temperature water and higher organic compounds are removed by a mixture of 1.5 kg 3 Å and 0.5 kg 5 Å molecular sieves. In case of water or ethanol additives the molecular sieve eventually saturates, but it is still capable of removing other impurities. Both, molecular sieve and BTS-catalyst are regenerated twice per year or whenever necessary.

Continuous control of gas composition is necessary for constant operation. Infrared meters, dedicated to a certain gas type, but with some sensitivity left for the gas additives give permanent information on changes. Hygrometers in the ppm-range and an O_2-trace analyser allow an early detection of leaks. Complete analysis of the gas composition is performed by an automatic gas chromatograph station, routinely switched into the different circuits. Independently of the use of calibrated gases this instrument gives the different gas portions to an accuracy of ±2% of the measured value with an overall sensitivity of about 300 ppm [42,43].

2.6.3. Electronic control and safety

The concept of the H1 gas system control follows the solution chosen for L3 time expansion chamber (TEC) [44,45]. A Motorola 68000 CPU serves as a crate master, integrated into a VME-system with the necessary resources for monitoring, logging and control equipment. The instantaneous values of all analog outputs of the measuring devices, especially those for pressure and temperature, but also those for supply voltages are controlled within preset limits. Warnings or alarms are generated if one of the relevant parameter values is exceeded. In case of an alarm the gas circulation is stopped and the HV supplies of the detectors concerned are switched off. A computer independent hard wired logic with a more generous alarm setting protects the chambers against destruction in case of program failures or other accidents. In this case also an alarm is generated and the powerless open solenoid valves in the distribution rack on top of the electronic trailer connect the chambers with an argon flushed reservoir at atmospheric pressure as indicated in Fig. 15. A set of four independent serial links per gas system monitors all gas parameters and distributes this information to the slow control system (see Section 6 of Ref. [1]).

Gas sensors are distributed in the H1 detector region, on the electronic trailer with the distribution rack and in the volume occupied by the trackers, as well as in the rooms where flammable gases are handled.

The tracker volume is flushed with $\simeq$ 12 m^3 of nitrogen gas per hour to prevent accumulation of flammable gases in case of a leak. Since the operational pressure of most chambers is as low as 0.15 hPa relative to atmosphere and only 1.5 hPa in case of CJC, the amount of gas which may escape through a sudden leak in the chamber region is at most only a few l. Small continuous leaks are best controlled in the closed loop circuits by measuring the pressure drop in the barrel over several days. The maximum working pressure in these circuits is limited to 1.6 bar absolute. A typical leakage of about 4 l/day corresponds to a pressure drop of $\sim$ 40 hPa/day. In the open circuits additional electronic flow controls, in series with FL1-1 and FL1-2, restrict the input flow. In case of a major leak the operational chamber

[16] BASF AG, Ludwigshafen, Germany.
[17] Messer Griessheim AG, Griessheim, Germany.
[18] Bayer AG, Leverkusen (Vertrieb Hamburg), Germany.

pressure cannot be reached with the low flux adjusted by these controls.

2.7. Scintillators

Both scintillator arrays discussed in this section are located in the backward region (see Fig. 3 of Ref. [1]) and have been installed to reject proton beam associated background at the first trigger level. The present life time of the stored proton beam in HERA during collisions varies between 10 and 48 h. The stored proton current design value is 160 mA with 2×10^{13} circulating protons in total. These protons are lost by beam gas and beam wall interactions producing background showers of energetic penetrating hadrons and halo muons. With a beam life time of 10 h the H1 sensitive detector volume is hit by this background with a frequency of 2.6 MHz.

2.7.1. Time-of-flight counters

The time of flight hodoscope (ToF) consists of two planes of 3 cm thick NE102A scintillator mounted perpendicular to the beam pipe upstream of the interaction region. Particles from proton induced background and from e–p collisions are separated in time at this point by $\sim$ 13 ns. The electron bunches have negligible size whereas the proton bunches are spread over 2 to 3 ns FWHM. The plane nearest to the interaction point (ToF1) lies at $z = -1.95$ m and has 16 butted counters, measuring 317×317 mm^2 thus matching the size of four BEMC stacks. The outer plane at $z = -2.25$ m consists of eight larger counters (317×634 mm^2).

In order to operate inside the 1.14 T field, ToF utilizes 24 Hamamatsu R2490-01 high field photomultiplier tubes (PM). It is necessary to mount them perpendicular to the planes of ToF, requiring a light collection countersink to be machined into one of the large faces. A corresponding perspex truncated cone is glued to the other side to match the PM sensitive area. The PMs themselves are housed in non-magnetic holders and held in contact with the small light guide by springs.

Each wall of ToF is made up of a sandwich of scintillator and lead (Fig. 16), mounted on a backing plate of non-magnetic steel to minimise stresses from the large magnetic field. The lead is 6.5 mm thick to absorb synchrotron radiation. Steel is used rather than aluminium to minimise eddy currents produced during a magnet quench.

The six inner counters (four on ToF1, two on ToF0) can be moved horizontally up to 20 cm from the beam pipe using computer controlled pneumatic rams. This removes them from the high radiation fluxes around the beam pipe during injection. With the counters in the open position, ToF can be split in half about the horizontal axis, allowing removal without breaking the vacuum in the beam pipe.

Signals produced by the PMs are amplified ($\times 40$), up to $\sim$ 1 V before travelling down 29 m of cable to a NIM logic located in the electronics trailer. Here the signals are discriminated and strobed in three time windows: background, interaction and global, which are used in the first level trigger decision (see Section 5.3.1 of Ref. [1]) available after 250 ns. The device as a whole has a resolution of 4 ns, while individual counters have a resolution of the order of 2 ns. The timing information of all counters is available in the event readout chain.

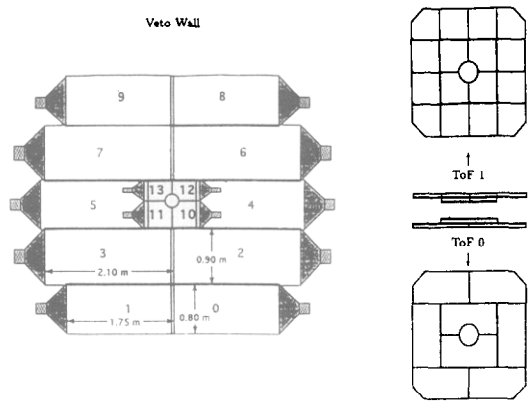

Fig. 16. Schematic cross section of the inner and outer veto wall (left) and the ToF counters.

The setting and width of the time windows greatly affects the performance of ToF, and they are continually updated as offline analysis proceeds. The background window currently

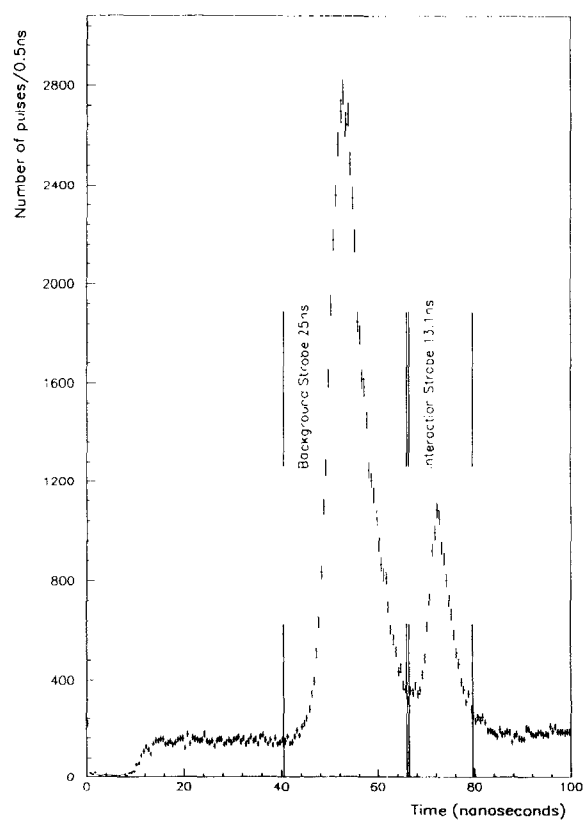

Fig. 17. Time distribution of hits in a ToF counter.

starts 18 ns before the centre of the background distribution, and is 25 ns long. The interaction window starts 1 ns after the background window ends and is 13.1 ns long (Fig. 17). A constant background of cosmic ray hits is present, about 200 entries per bin. Triggers in the interaction window are in fact much dominated by synchrotron radiation.

2.7.2. *The veto wall*

In addition to the ToF device two double scintillator veto walls are installed at a distance of 6.5 and 8.1 m, respectively upstream from the interaction point (see Fig. 3 of Ref. [1]).

The smaller inner veto wall covers the near beam area (100×90 cm^2) down to a radius of 11 cm (Fig. 16). The four scintillator pairs (NE 114, thickness 6 mm) are read via two photomultipliers (56 AVP, VALVO) each. The pairs are shielded against electromagnetic showers by lead walls of 4 cm thickness. Penetrating particles are then identified by coincidences between two scintillators with a time resolution of ± 3 ns. The large outer veto wall with an area of ca. 5×4 m^2 overlaps the inner veto wall and nearly all of the liquid argon calorimeter. The array of 10 counter pairs of up to 2.1×0.90 m^2 area each (Fig. 16) is grouped around the last upstream HERA quadrupole with a 0.8×0.8 m^2 sized hole. The scintillators (NE 110, 1 cm thick) are coupled to 20 5 in. phototubes of type VALVO XP 2041. These tubes are shielded with thick iron tubes and μ-metal cylinders against the magnetic fringe field (≈ 10 mT).

An iron wall of 5 cm thickness separates the scintillator pairs of the outer wall. The coincidence resolution of such pairs is ± 8 ns. It is dominated by the light path differences over the large area. The light attenuation length is measured to be larger than 1.5 m and leads to inefficiencies for the detection of minimum ionizing particles of $< 10^{-5}$. (see also Refs. [46–48]). The time resolution achieved allows a clear time separation between the background of the passing proton beam and event correlated hits during e-bunch passing. A 3 m concrete wall separates the outer veto wall from the main detector and protects it against low energy showers from upstream.

Amplitudes, signal arrival times, rates and efficiencies of all counters are monitored online, and this information is used to study the background condition after each filling and during runs. The time of flight information allows to measure the z position of the e–p interaction point online with a precision of ca. 30 cm. It is used in the first level trigger (see Section 5.3.1 of Ref. [1]), and is sent to the central data acquisition system for off-line analysis.

3. Calorimetry

The H1 detector was designed to provide clear identification and precise measurement of electrons, muons and penetrating neutral particles together with good performance in the measurement of jets with high particle densities. These requirements were best met by a calorimeter inside a large

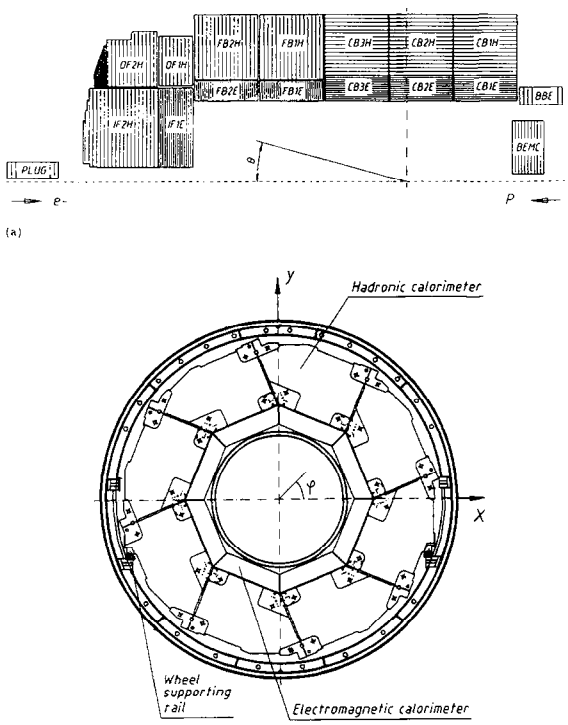

Fig. 18. (a) Longitudinal view of calorimeters. (b) Radial view of a LAr calorimeter wheel.

coil to minimise both the amount of dead material in front of the electromagnetic calorimeter and the overall size and weight of the calorimeter [49].

The main reasons for choosing the liquid argon technique were good stability and ease of calibration, fine granularity for e/π separation and energy flow measurements as well as homogeneity of response.

Fig. 18a shows the longitudinal view of the calorimeters along the beam axis and Fig. 18b shows a transverse view of the LAr calorimeter with the wheel structure that is described below. The LAr calorimeter covers the polar angular range between $\theta = 4°$ and $\theta \approx 154°$. The calorimetric coverage is completed with a small calorimeter in the proton direction (PLUG) with copper absorber and silicon pad readout, covering the region between the beam-pipe and the liquid argon cryostat ($\theta \leq 4°$) and a lead scintillator backward electromagnetic calorimeter (BEMC) located in the electron direction after the tracker and covering angles $151° \leq \theta \leq 176°$. The tail-catcher system (TC) is used to provide a rough calorimetric measurement of hadronic particles leaking out of the LAr calorimeter and is based on the analog readout of the pads of the limited streamer tubes that instrument the iron yoke.

In the next section the LAr calorimeter is described; descriptions of the BEMC, the PLUG and the TC can be found in Sections 3.2, 3.3 and 3.4 respectively. Further details on the instrumentation of the iron yoke are given in the sec-

tion on the muon detector (see Section 6). For a more detailed description of the LAr calorimeter system we refer to Ref. [50].

3.1. The liquid argon (LAr) calorimeter

3.1.1. Cryostat and cryogenic system

All walls are made of stainless steel except for the inner ones of the warm and cold vessels around the beam pipe and the tracker which are made of aluminium alloy, to minimise the dead material in front of the electromagnetic calorimeter (EMC). The cold vessel is able to withstand a maximum pressure of 3 bar and to support the weight of the calorimeter modules (450 t) and of the liquid argon load (53 m^3). Cooling down to LAr temperature is achieved by circulation of helium gas cooled through an external heat exchanger which is removed when no longer needed. The LAr load is transferred from a 70 m^3 storage tank located at ground level (about 20 m above the detector) into the cryostat through the bottom of the cold vessel. A regulated flow of liquid N_2 through heat exchangers located within the cold and expansion vessels ensures temperature and pressure regulation (1.35 bar). Control of all processes, including cool-down/warm-up and filling/emptying is done by a system controlled by VME processors. Since operations started in early 1991 the calorimeter has remained at liquid argon temperature and most of the time full of liquid argon except for the few days needed to move the detector in or out of the beam. For more details to this system we refer to Ref. [50].

3.1.2. Liquid argon purity

A liquid argon purity monitoring system has been integrated into the LAr cryostat to check the stability of the ratio of energy loss to collected charge to the level of $< 1\%$. The basic sensor is a liquid argon ionization chamber to which an electric field of 625 V/mm is applied, corresponding to the nominal field applied to the calorimeter stacks. Its cathode is coated with a ^{207}Bi source of 10^4 Bq activity. The energy spectrum of the radioactive decays is continuously monitored. The data from 11 such probes distributed around the cryostat show that the signal attenuation due to pollution from the stacks is less than 0.5% per year.

3.1.3. Stack design and construction

The segmentation along the beam axis is done in eight self supporting "wheels" as shown in Fig. 18, each of them segmented in ϕ into eight identical stacks or octants. The two forward wheels are somewhat similar in the principle but mechanically assembled as two half rings. An effort was made to minimise dead regions due to cracks.

Common features for all active cells are pad readout on the ground side and a high resistive coated high voltage plane (except for the CBH stacks) with integrated decoupling capacitance as described below.

The hadronic stacks are made of stainless steel absorber plates with independent readout cells inserted between the plates. They define the rigid structure onto which the corresponding electromagnetic stacks are mounted. The orientation of the absorber plates is such that particles are incident on the calorimeter with angles not smaller than 45°. The structure of each electromagnetic stack consists in a pile of G10(epoxy+glass fiber)–Pb–G10 sandwiches separated by spacers defining the LAr gaps. The basic sampling cell is shown in Fig. 19a. It consists of 2.4 mm Pb absorber and 2.35 mm liquid argon as active material with, per gap, one readout plane with pads and one high voltage plane coated with high resistive paint (HRC). The latter is a mixture of carbon and glue with a surface resistance of 1–30 MΩ/□, sieveprinted on a Kapton foil. The high resistivity coating provides the HV protection and serves as a distributed decoupling capacity to keep negative cross-talk small. The hadronic sampling cells, as shown in Fig. 19b, consist of a total of 19 mm stainless steel, (16 mm absorber from the welded structure and twice 1.5 mm from the plates of the independent readout cells defining the active liquid argon gap) and of a double gap of 2.4 mm liquid argon. They have, in the middle of the active gap, a G10 board with pads on both sides to collect the charges deposited in the gaps. A Kapton foil coated by a layer of HRC (IF2H, FBH, OF stacks) or with copper (CBH) is glued to the inner side of the stainless steel plates, with the same functions as for the electromagnetic modules. The HV is applied to the HRC (or copper for CBH, in which case neon spark gaps mounted close to the gaps act as active protection). For more details we refer to Refs. [49,50]).

The basic calorimetric material constants are given in Table 1 of Ref. [51]. The granularity of the read-out cells stems from the requirements of a good separation of electromagnetic and of hadronic showers. Longitudinal segmentation is 3- and 4-fold for the EMC over 20 to 30 radiation lengths (X_0) and 4- to 6-fold for the hadronic calorimeter (HAC) over 5 to 8 interaction lengths (λ). Furthermore the tower sizes are such that the channel capacities are kept below 14 nF so that the electronic noise is at a reasonable level, with the additional constraint from the calorimeter trigger that channels belonging to the same trigger tower should have similar capacities within ±5% for good timing adjustment.

The high voltage distribution is done by 1504 independent lines. Each line feeds a group of nonconsecutive planes in a stack, interleaved with planes linked to another HV line to reduce the probability that a complete tower segment be dead in case of a high voltage problem in one line. The present operating voltage of the calorimeter is 1.5 kV which corresponds to an electric field of 625 V/mm. The very good purity observed allows high charge collection efficiency (about 94% [50,52]) at this low field value, thus minimizing HV problems. After 3 year of operation less than 3% of the high voltage lines do not reach the full voltage.

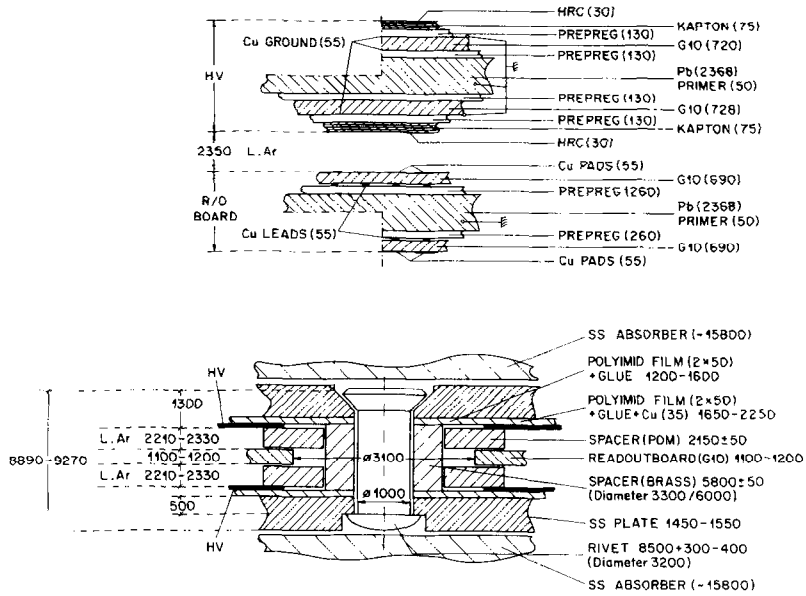

Fig. 19. Schematic structure of the readout cell: (a) e.m. cell, (b) hadronic cell. All dimensions given in μm.

3.1.4. Electronic system

A major constraint in the design of the system, is that large energies may be deposited at short time intervals (96 ns at HERA) into detectors with large capacities and long collection times, and the information has to be stored until the arrival of the trigger signal (≈ 2.5 μs). The basic layout of the electronic chain is described in more detail elsewhere [49,50]. The preamplifiers, each with two shapers, a slow one and a fast one, are located just outside of the cryostat and feed on one hand the analog readout system where the signals of the slow shapers are read out via two multiplexers giving an overall multiplexing factor of 128, and on the other hand the trigger read out system where the outputs of the fast shapers are processed (see Section 5.3.2 of Ref. [1]). To extend the dynamic range to 14 bits while using a 12-bit ADC, a double transmission system with two different gains for about 50% of the channels is used thus increasing the number of channels to be read-out to about 65 000 (electronic channels). The signals are sent twice via $\approx$ 30 m twisted pair lines to differential line receivers located in the analog receiving unit (ANRU) which performs analog baseline subtraction [53]. Each ANRU serves 512 calorimeter channels and is connected to an ADC board serving 1024 electronic channels that is controlled and read out by a digital signal processor (DSP) module performing data correction. This read-out system is described below (Section 3.1.6). The total amount of channels where no signal reaches the preamplifier because of bad contacts within the cryostat is 0.15% and has remained stable for about three years after closing the cryostat.

3.1.5. Electronic calibration system

To ensure that the calibration of the electronic chain is known and stable to within a few 10^{-3}, calibration capacitors of 47 pF, selected to be within ± 1%, are used. They are charged with voltage pulses of precisely ($\approx 10^{-3}$) known amplitude.

Two systems have been built into the calorimeter: the first one (cold calibration) with the calibration capacitors in the liquid argon, as close as possible ($\approx$ 1 m) to the gaps, pulses individual channels (one out of 16) allowing detailed cross talk studies. The second system, with calibration capacitors at the preamplifier level (warm calibration), is used mainly as a backup for calibrating channels with a problem in the calibration line within the cryostat. In this case an extrapolation technique developed during the runs in test beams at CERN is used, and a precision of the order of 1% in the determination of the calibration constants is achieved. This method is presently applied to less than 1% of the 45 000 calorimeter channels.

A third order fit to the calibration data is performed for each channel [50] from which the constants to be downloaded into the DSPs are determined. At H1 such operations are done once every few weeks. Fig. 20 shows the stability of the calibration constants over one month.

The calibration constants need no correction for diagonal cross-talk as they are determined by pulsing the cells individually using the high granularity cold calibration system. Nondiagonal cross-talk has been determined from the test beam data and was found to be small (≤ 0.5%), mainly affecting the CBH modules.

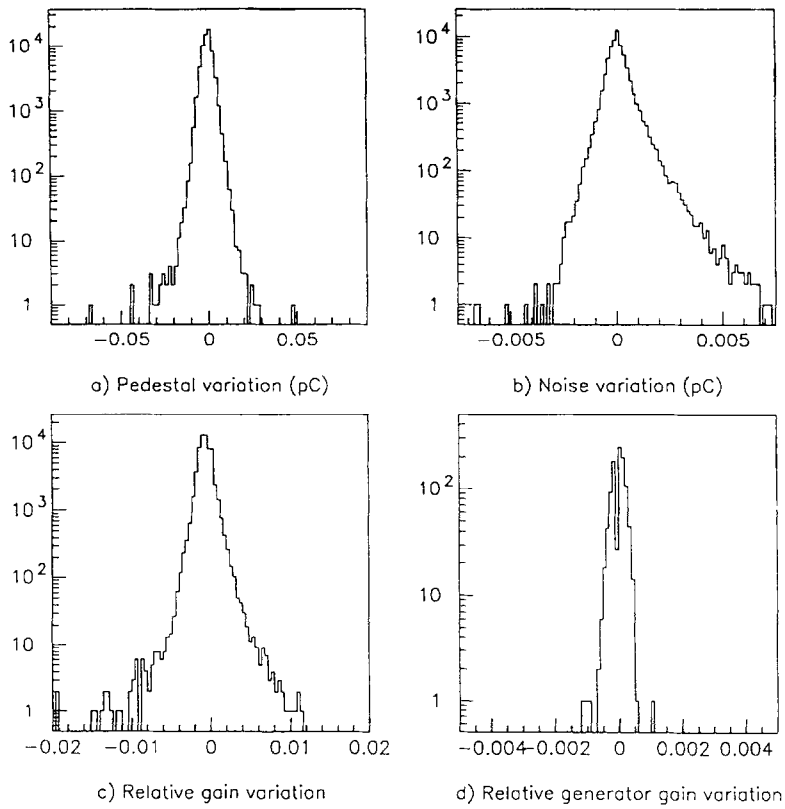

Fig. 20. Relative stability of the electronic chain over one month.

3.1.6. Calorimeter data acquisition

The calorimeter data acquisition system reads out data from the LAr calorimeter, the BEMC, the PLUG calorimeter and the analog part of the instrumented iron (TC). These detectors have the same readout electronics starting from the ANRU. The LAr calorimeter yields most of the data and its readout is described here. At the preamplifier level the data are split into two paths as mentioned in Section 3.1.4. In the analog data path the first level trigger decision samples the slow shaper pulse at its maximum. At the level 2 trigger (L2), 20 μs after the collision, the analog to digital conversion of the 65 000 electronic channels is started (total encoding time is 1.2 ms). The ADC counts of all electronic channels are then converted into calibrated charges by 69 DSPs working in parallel. The DSP boards [54] used here are based on the Motorola DSP56001 and perform for each cell a noise suppression done in parallel to the encoding and an order three polynomial correction. These DSPs provide calibrated charges formatted with the offline numbering of the calorimeter cells. On-board memories are downloaded with the current set of calibration constants (for each channel four parameters and the 1σ noise value are needed). The code contains less than 200 instructions. It is written in assembler language and was optimized to fit into timing specifications and the available program memory space in the DSP chip.

In the trigger data path, the pipelined trigger chain produces digital sums for each of the 22 bunch crossings following the collision. A first level trigger decision (L1) based on total and transversal energies is derived within 2.5 μs. Ten dedicated DSPs read the data of the fast shapers (see Section 5.3.2 of Ref. [1]). They verify the timing and the shape integrity of the trigger tower signals, calculate pileup estimators based on charge and time analysis, and report any malfunctionings [55]. They store the signal history of a total of 474 trigger towers over 256 bunch crossings around the trigger time (t_0). From these data, every second sample in the interval ranging from -25 to $+25$ bunch crossings is read out for pileup studies. The DSP boards used in this path are based on the same DSP chip as for the analog data read out but are of a different design, with a special interface to the trigger data.

The formatted data for both paths, within independent VME branches, are collected by two event builders based on the RISC processor AM29000 running the real time kernel VRTX. The AM29000 event builders, one for the analog data and the other for the trigger data, run on top of the real time kernel VRTX, with minimal system overhead. The data are passed to the event logging task through a circular buffer. The event is then formatted and sent to the central data acquisition through an optical fiber link (see Section 7.1.2 of Ref. [1]).

Table 8
Approximate energies and minimum ionizing particle equivalents (mips) corresponding to 1σ noise in the electromagnetic and hadronic sections of the central barrel and inner forward modules respectively.

	CB	IF
EMC	30 MeV/0.25 mips	15 MeV/0.15 mips
HAC	30 MeV/0.15 mips	24 MeV/0.15 mips

Presently with an event size for the calorimeter branch of about 20 kbyte and a first order dead time of 1.2 ms the maximum data taking rate has been measured to be 200 Hz (100% dead time). At a rate of 100 Hz the dead-time is 15%.

A processor based on the Motorola 68030 chip and operating under an OS9 system is used for run control and as a stand alone facility.

3.1.7. Reconstruction techniques

Input to LAr calorimeter reconstruction are calibrated charges for each calorimeter cell, as provided by the DSPs. The calorimeter reconstruction program converts charges to energies in the calorimeter cells for both hadronic and electromagnetic showers, corrected for the effects of dead material, eliminates electronic noise and forms clusters from groups of cells.

The scaling from charge to energy (electromagnetic scale (see Section 3.1.8)) involves a charge to energy calibration factor (determined for each stack geometry in calibration runs at CERN, see Section 3.1.8), a correction for the charge collection efficiency for operating at 1500 V (derived from HV curves obtained with cosmic muons [50]) and correction factors for local variations of gap and absorber thicknesses (measured during stack construction).

The noise is measured for each channel during electronic calibration. It varies between 15 and 30 MeV equivalent energy depending on the calorimeter region (see Table 8). In events recorded with a random trigger 1100 cells out of a total of 45000 cells pass a $+2\sigma$ noise threshold on average. Adding up this energy for the full calorimeter yields an average value of 48 GeV with a standard deviation of 3 GeV (Fig. 21a). To suppress the noise further we use the negative noise, present in the Gaussian distributed noise signals after pedestal subtraction, to compensate the positive noise contribution to the measured signal. We keep cells above $+4\sigma$ (signal seed) and all neighbors in a $3 \times 3 \times 3$ cube around a seed cell ($> +4\sigma$) also to keep small signals at the fringe of showers. In order to compensate for noise picked up in the previous step also cells below -2σ around a signal seed are kept. Cells below -4σ are kept in order to compensate for noise contribution to $+4\sigma$ seed cells. No neighbors are collected around these -4σ cells which are purely noise. After this procedure, the residual noise contribution is 0.1 GeV with a $\sigma = 0.5$ GeV (Fig. 21b).

The signal loss introduced by the above noise suppression procedure has been studied with simulated low Q^2 DIS events. In these events the hadronic energies are low, with average deposited energies in the barrel region of the calorimeter of about 4.5 GeV, 800 MeV for hadrons and 400 MeV for photons. In this (most difficult) case 17% of the energy is lost due to this noise suppression. For high Q^2 events ($\langle Q^2 \rangle \approx 500$ GeV^2) the loss is smaller (5%). These losses are corrected for in the reconstruction of hadronic energy (see below).

For simulations, noise is included for each cell by using events recorded with random triggers in special runs with no online noise suppression.

Clustering All cells passing the cell level reconstruction are subject to clustering. The algorithms used are tuned so that the cells containing energy depositions from an electromagnetic shower initiated by a photon or electron are most probably merged into one cluster. Hadronic showers on the other hand, with their large spatial fluctuations are in general split into several clusters.

Further noise suppression Clustering allows further reduction of the noise in the hadronic part of the calorimeter. A hadron penetrating deeply inside the calorimeter usually deposits enough energy to form at least one cluster with a signal well above the noise level. Other small isolated energy depositions which are not distinguishable from noise are correlated in space with this prominent cluster.

Small signals are suppressed if they are in the last layer of EMC or in HAC and far away (> 50 cm) from the direction given by the centre of gravity of any prominent cluster (significance, $(\sum (E_i/\sigma_{\text{noise}})^2)^{1/2}$ above 8) and the nominal interaction point.

This suppression does not increase the signal loss mentioned in Section 3.1.7. The energy distribution of noise remaining in empty events after the suppression peaks at zero with a sigma of 0.25 GeV, as can be seen in Fig. 21b.

Correction for energy loss in dead material The energy losses in dead material in front of the calorimeter (the beam pipe, the central tracker and the inner cryostat wall) and in cracks between the calorimeter stacks are quite substantial. In low Q^2 DIS events they amount to $\approx 10\%$ of the energy deposited in the calorimeter, dead materials in front of the calorimeter accounting for about 90% of these.

Corrections for the energy loss were derived using Monte Carlo simulations. The event by event corrections are based on the measured calorimetric energies. To reduce the influence of noise on the correction, only cells with energy above $3\sigma_{\text{noise}}$ for cells in prominent clusters (see above) and above $5\sigma_{\text{noise}}$, otherwise, are considered.

Energy losses in front of the LAr calorimeter are corrected by using the first (inner) layer of cells in the LAr calorimeter. For each cell in the first layer with a signal above the threshold mentioned above, an energy is added according to:

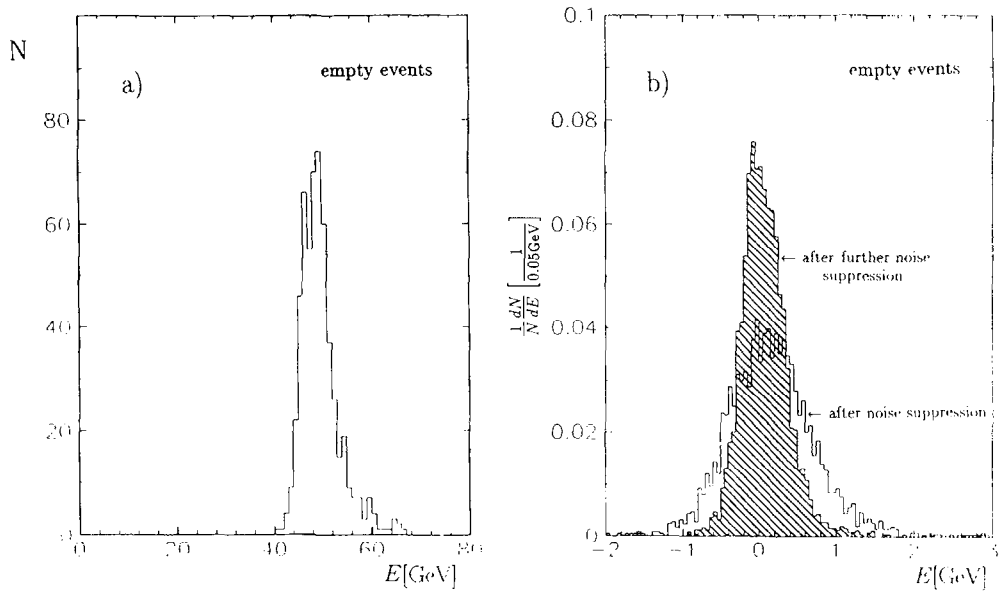

Fig. 21. Noise contribution summed over all channels of the LAr calorimeter: (a) after applying a $+2\sigma$ noise threshold, (b) after noise suppression.

$E^i_{\text{loss}} = \alpha_{\text{fr}} f^i_{\text{dead}}$.

Here f^i_{dead} is the energy loss of a minimum ionizing particle in the material in front of cell i in projective geometry with respect to the nominal interaction point. A global factor α_{fr} was determined for each half wheel along the beam direction by simulation. For the above energy estimate we use only the fact of the presence of an energetic cell, but not its energy. This approach allows a common correction procedure for losses caused by electrons and hadrons.

The correlation between the estimate of the energy losses in the reconstruction and the true energy lost in front of the calorimeter for simulated low Q^2 DIS events is given in Fig. 22. An example of the effect of the dead material correction for experimental data is shown in Fig. 23, where the π^0 peak in the effective mass of two photons (e.m. clusters) is moved by the correction into the region of the π^0 mass.

The correction procedure for energy losses in a crack uses cells in the layers nearest to the crack and on either side of it. Cells on one side of a crack are coupled with cells on the other side and for each such pair an energy loss between them is estimated by

$$E^j_{\text{loss}} = \beta f^j_{\text{dead}} E^j_{\text{l}} E^j_{\text{r}} / (E^j_{\text{l}} + E^j_{\text{r}}),$$

distributed between the two cells of a pair in proportion to the cell energy. Here E^j_{l} and E^j_{r} are energies in a pair j deposited at left and right sides of the crack. The function f^j_{dead} takes into account local inhomogeneities of dead materials. A global factor β was determined for each type of crack. These factors differ considerably for pions and electrons. For the moment, only corrections of the hadronic type are used in the reconstruction because of difficulties in the separation of hadronic and electromagnetic components in ϕ and z crack regions.

Fig. 24 shows the performance of the dead material correction as function of θ and ϕ for simulated pions of 20 GeV. The crack structure which is clearly seen before the correction nearly vanishes after the correction. The CB2/CB3 z-crack almost pointing to the interaction point was scanned by a pion test beam of 30 GeV at CERN. Results are given

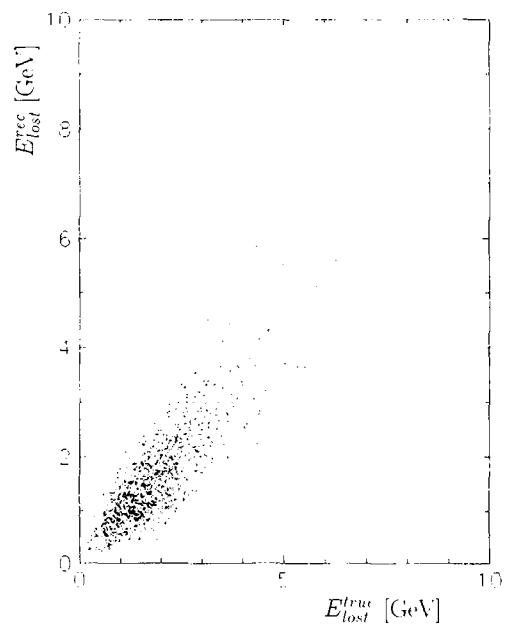

Fig. 22. Correlation between the true energy lost in front of the calorimeter ($E^{\text{true}}_{\text{lost}}$) and its estimation in the reconstruction ($E^{\text{rec}}_{\text{lost}}$) for simulated low Q^2 DIS.

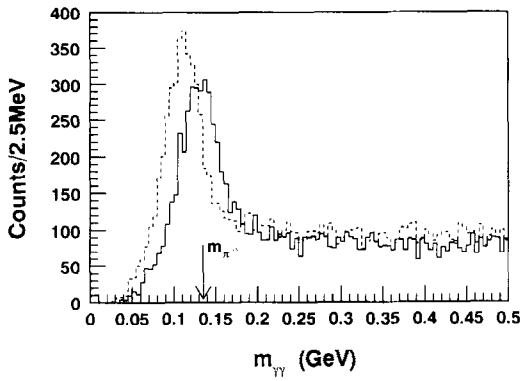

Fig. 23. The effective mass of two photons before (dashed histogram) and after (hatched one) the dead material correction.

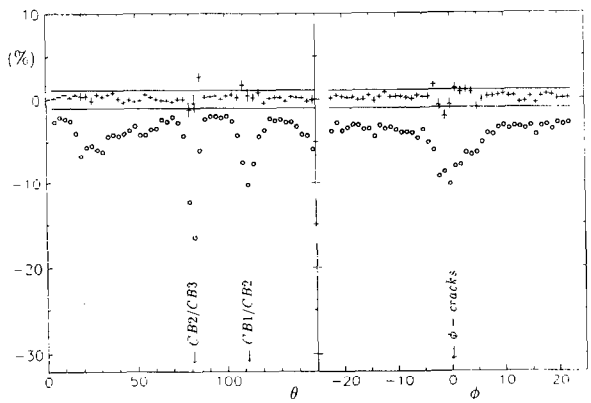

Fig. 24. Performance of the dead material correction for simulated pions at 20 GeV. Ratios $(-E^{true}_{lost})/E^{true}_{tot}$ (circles) and $(E^{rec}_{lost} - E^{true}_{lost})/E^{true}_{tot}$ (crosses) are shown as function of θ and ϕ (both given in degrees). Before the correction a crack structure is clearly seen. Solid lines correspond to ±1% deviations from the true energy.

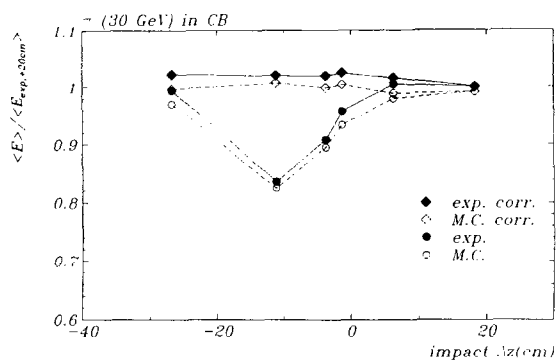

Fig. 25. Response across the CB2/CB3 z crack in a pion test beam of 30 GeV at CERN.

in Fig. 25. The response across the crack is well described in the simulation.

The hadronic energy scale The LAr calorimeter is non-compensating. The charge output for hadrons is about 30% smaller than for electrons. Therefore an additional correction has to be applied to the signal obtained on the electromagnetic scale.

The fine segmentation of the LAr calorimeter allows to distinguish the primary electromagnetic component of a jet which is already on the correct (electromagnetic) energy scale. It also allows a high level of compensation within hadronic showers to be reached by weighting signals from individual calorimeter cells (see below).

The primary electromagnetic clusters are filtered using such characteristics as the fraction of cluster energy deposited in EMC (containment in EMC), in the first layer of EMC (early shower development), and in the four most energetic cells of a cluster (compactness); see Ref. [51]. The filtering is done for clusters with an energy above 1 GeV.

The hadronic objects in the reconstruction are formed by cells which are not included in an electromagnetic cluster and are located within a radius r around the direction given by the nominal interaction point and the centre of gravity of the hadronic cluster ($r < 25$ cm in EMC and $r < 50$ cm in HAC). Here, a cluster is called hadronic if it is prominent (see above) and if it is not recognized in the filtering as an electromagnetic one or, at lower energies, if it is developing deeply inside the calorimeter.

To get the proper hadronic scale for hadrons, a software weighting technique is applied, which was initially proposed by the CCFR Collaboration and used in the CDHS experiment [56]. This method was further developed by H1 on the basis of CERN test runs [57–61]. The aim is to equalize the response to the electromagnetic and hadronic components of a hadronic shower and, therefore, to suppress the influence of the large fluctuations in the hadronic shower composition on the reconstructed energy. The technique exploits the fact that local energy deposits of high density are mainly of electromagnetic origin while the hadronic component is much more spread out. Thus, in a well segmented calorimeter the amount of energy deposited in the cells can be used for statistical separation of electromagnetic and hadronic energy depositions.

In the reconstruction the weighted energy in a cell i, E^i_{rec}, is calculated from the cell energy on the electromagnetic energy scale, E^i_0, by:

$$E^i_{rec} = \{a_0 + a_1 \exp(-\alpha E^i_0/V^i)\}E^i_0,$$

where a_0, a_1, and α are the parameters of the weighting function (different for EMC and for HAC) and V^i is the volume of the cell. These parameters were determined as function of the reconstructed jet energy (calculated inside cones of 10°) using a Monte Carlo simulation of jets [62]. For hadrons with energy below 7 GeV this ansatz is replaced by simple multiplicative factors corresponding to effective e/π ratios in EMC and HAC. In the region 7 to 10 GeV both methods contribute to the correction in order to get a smooth transition from the simple correction factors to the weighting.

The remaining cells not included into electromagnetic

clusters or hadronic objects are due to low energy particles depositing energy in the first two (three in the forward region) inner layers of the calorimeter. These leftovers are affected by noise, and the energy correction to be applied depends on particle composition and energy spectra. The corresponding correction factors were defined using simulated low Q^2 DIS events.

3.1.8. Calibration and performance

The most important task in understanding the calorimeter modules is the energy calibration. This was done by putting full scale calorimeter modules in a test beam at CERN. Checks of the calibration quality were done once the H1 detector was fully operational by using various techniques as described below, such as determining the response of the electromagnetic calorimeter to electrons generated by cosmic muons crossing the detector or verifying the P_t balance between the electromagnetic and the hadronic energy in deep inelastic events at HERA.

Overview of the test runs at CERN An extensive calibration program with e-, π- and μ-beams was performed in the H6 test beam at the CERN SPS with prototypes [57,58,63] and with modules installed later in the H1 cryostat at HERA [64,65]. These beam tests supplied the basic calibration constants of the calorimeter.

Only one of each type of the calorimeter stacks was tested as the very strict mechanical constraints (see Refs. [49,50]) needed to reach a homogeneity at the 1% level were achieved during the construction phase, allowing to transfer calibration constants from one module to another.

Eight characteristic stack configurations were tested separately using the same beam setup, calorimeter readout and calibration electronics. These configurations include a full coverage of θ and all important crack configurations [64,65]. Special modules consisting of half stacks assembled to reproduce a CB2–CB3 ϕ crack (see Ref. [66] and an FB1–FB2 ϕ crack (see Refs. [67,68]) were built and put into the test beam in 1992.

The purity of the liquid argon was constantly monitored by probes identical to those used in the detector described in Section 3.1.2. The decrease of the signal with time was much faster than in the H1 detector because of polluting agents brought by the stacks. It was not possible to use the same flushing and cool-down procedures for the test set-up as in the final detector. Big variations in the pollution rate from one configuration to the next were attributed to the different cleaning agents used during the construction of the stacks which were built at various institutes.

The same front end electronics scheme and calibration system as at HERA was used as much as possible. Data were taken with beam energies in the range 3.7 to 80 GeV for electrons and 3.7 to 205 GeV for pions.

In some of the data taking periods a tail catcher module was added behind the hadronic calorimeter allowing combined analyses [58,64]. The tail catcher modules were also calibrated in standalone tests [69].

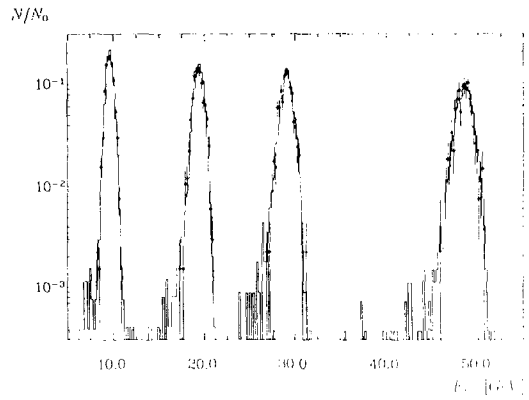

Fig. 26. Reconstructed energy for data (histogram) and MC (points) for electron energies of 10, 20, 30 and 50 GeV (BBE wheel).

Test beam results For the electromagnetic energy scale two calibration constants ($c^{\mathrm{exp}}_{\mathrm{EMC}}$, $c^{\mathrm{exp}}_{\mathrm{HAC}}$) were determined for each wheel, which transform the measured electric charge Q_i per cell into energy deposited by electron showers. Corresponding constants ($c^{\mathrm{MC}}_{\mathrm{EMC}}$, $c^{\mathrm{MC}}_{\mathrm{HAC}}$), transforming visible energy into deposited energy are obtained in Monte Carlo simulations (MC) for electrons (of 30 GeV). These constants are defined to be independent of effects of dead materials in front of the calorimeter, any leakage and analysis cuts.

The corresponding experimental constant $c^{\mathrm{exp}}_{\mathrm{EMC}}$ is obtained by a comparison (see Fig. 26) of experimental data with detailed simulation of the test setup and requiring the reconstructed energies to agree:

$$E^{\mathrm{exp}}_{\mathrm{rec}} = c^{\mathrm{exp}}_{\mathrm{EMC}} \sum_{i}^{EMC} Q_i = E^{\mathrm{MC}}_{\mathrm{rec}} = c^{\mathrm{MC}}_{\mathrm{EMC}} \sum_{j}^{EMC} E^{\mathrm{vis}}_j . \qquad (1)$$

For the calibration constant a value of $c^{\mathrm{exp}}_{\mathrm{EMC}} = 3.55$ GeV/pC is obtained on average. For the hadronic stacks no electron data were available and $c^{\mathrm{exp}}_{\mathrm{HAC}} = 7.1$ GeV/pC was obtained by scaling the value of the EMC by MC.

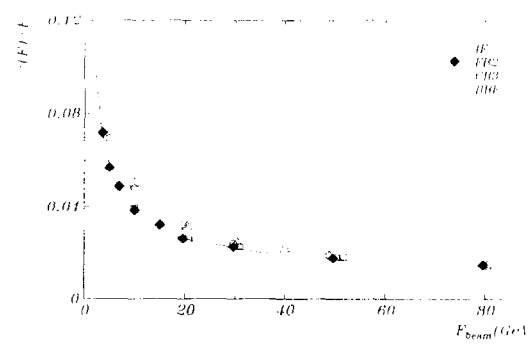

Fig. 27. Energy resolution as function of electron energy for wheels BBE, CB, FB2 and IF. Solid line: parametrization for FB2.

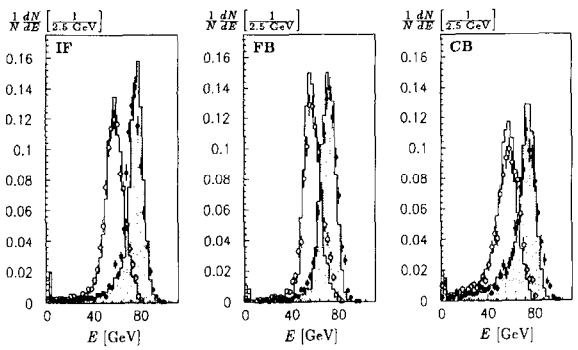

Fig. 28. Energy reconstruction for pions at 80 GeV for wheels CB, FB and IF on the electromagnetic (open) and hadronic energy scale (closed, shadowed) for data (histogram) and MC (points).

The resolutions σ/E obtained for various stacks are in the range 10% to $13\%/\sqrt{E}$ with constant terms below 1%. Fig. 27 shows the results for four different stacks and the parametrization for FB2 according to

$$\sigma/E = \sqrt{A^2/E + B^2/E^2 + C^2}, \qquad (2)$$

with $A = 11\%\sqrt{E}$, $B = 154$ MeV and $C = 0.6\%$. The measured resolutions differ at low energies due to different handling and influence of electronic noise for the various stacks. The observed nonlinearities are below 1% after corrections for effects of dead material and noise by Monte Carlo.

The calibration constants of the various stacks were found to vary by about 2.5%. This is larger than expected from the known mechanical differences of different wheels. The main error source were impurities in the liquid argon during the CERN test. The variation is consistent with the systematic error of the extrapolations of the high voltage plateau curves by which the charge collection efficiency was determined. Further tests of the energy scale are possible at HERA (see below). For further results on the calibration by test beam electrons and simulations we refer to Ref. [65] and for more details to Refs. [61,70–75].

The response to pions has been extensively studied for the different calorimeter wheels and compared to detailed simulations (compare Refs. [64,61,76,73,77–79]). An application of the standard H1 reconstruction code (Section 3.1.7) is shown in Fig. 28, where data and GHEISHA simulation [80,81] for pions at 80 GeV are compared in 3 different wheels on the electromagnetic scale and after reconstruction of hadronic energies. No attempt is made here to correct for leakage. The effect of the inclusion of the streamer tube tail catcher (see Section 3.4 and Ref. [82]) which adds at the test beam another 4.5 interaction lengths (λ_{abs}) to the 6 of the IF wheel, can be seen in Fig. 29. It shows the reconstruction at a pion energy of 205 GeV for all events and for those fully contained in liquid argon. The obtained resolutions are about $\sigma/E = 50\%/\sqrt{E}$ with an energy independent term of 2% as shown in Fig. 30.

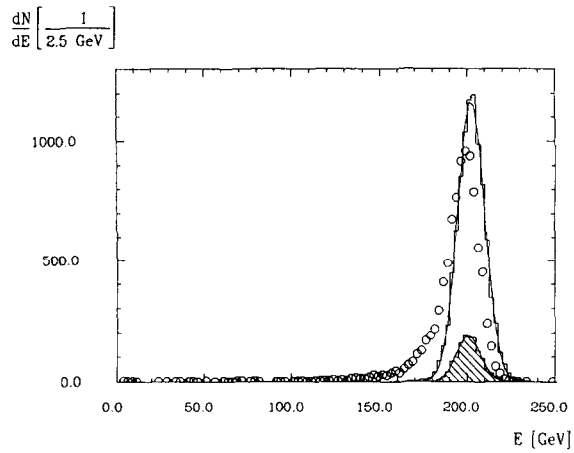

Fig. 29. Energy reconstruction for pions at 205 GeV for wheel IF with tail catcher (open histogram), only IF (circles) and for events fully contained in IF. Solid lines: fitted Gaussian distributions.

Performance at HERA Data taken at HERA, since April 1991 with cosmic muons, and since June 1992 with beams, allowed for checks of both the overall electromagnetic and hadronic energy scales.

The orientation of the three CB wheels is especially favorable for the study of the signals from cosmic muons and allowed to check the charge collection, the overall calibration and the time stability. The charge collection efficiency at the operating voltage of 1.5 kV was determined by high voltage plateau curves to be 0.944 ± 0.014. The electromagnetic energy scale as determined at the CERN beam tests (see above) could be verified to $\pm 8\%$ (Ref. [52]). More precise tests are possible with electrons (see below).

The overall response to muons of the individual electromagnetic and hadronic sections of the three CB wheels varied from October 91 to November 94 by less than $\pm 3\%$.

A fraction of the cosmic muons traversing the detector generates electrons. Their momentum p can be measured in the central tracker CJC and can be compared with the energy E measured mainly in the CB wheels. A typical event is shown in Fig. 31 together with the measured E/p distribution for selected electrons with $p > 1$ GeV/c and incident angles below 25° with respect to the normal of the calorimeter plates. The mean (0.96 ± 0.01) and width ($\sigma =$

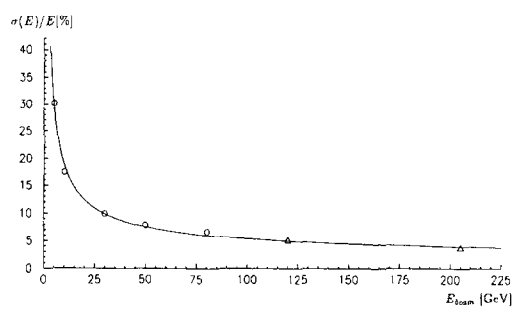

Fig. 30. Energy resolution as function of pion energy for wheel IF. Circles: IF only, triangles: IF + iron tail catcher. Parametrization according to equation (2) with $A = (50.7 \pm 0.1)\%$ [$\sqrt{\text{GeV}}$], $B = 0.9$ GeV and $C = 1.6 \pm 0.1\%$.

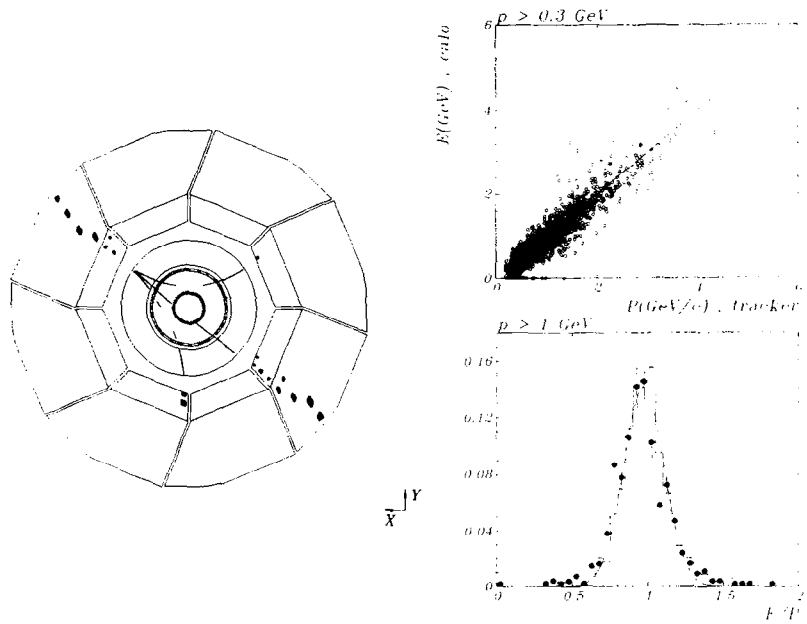

Fig. 31. Energy/momentum match of electrons generated by cosmic muons measured in the CJC and LAr CB wheels.

0.15) agree with the simulation within errors. The width corresponds to a resolution of $\sigma/E \approx 0.20/\sqrt{E}$, but this value is still influenced at these energies ($\langle p \rangle = 1.6\,\mathrm{GeV}/c$) by noise and dead material corrections (Section 3.1.7) of about 10%.

With these techniques the forward wheels cannot be reached, but the performance of IF and FB wheels can be checked by two photon mass spectra as demonstrated in Fig. 23 which shows a clear π^0 mass peak.

Deep inelastic scattering events where the scattered electron and the hadronic jet are detected both in the LAr calorimeter can be used for a direct comparison of the hadronic and electromagnetic energy measurement exploiting p_t balance. The transverse components p_{te} and p_{th} are calculated by summing vectorially the calorimeter cell energies. Fig. 32 shows that the measured energy balance is compatible with simulation.

3.2. The backward electromagnetic calorimeter (BEMC)

The backward ($-z$) region of the H1 detector is instrumented with a conventional electromagnetic lead-scintillator sandwich calorimeter.

The primary task of this backward electromagnetic calorimeter is to measure energies and directions of electrons scattered under small angles from DIS processes. In addition the BEMC contributes to the measurement of hadrons emerging from photoproduction and medium to low-x, high-y hadronic final states from DIS.

The kinematics of DIS accessible with this calorimeter is characterised by moderate four-momentum transfers $5\ \mathrm{GeV}^2 < Q^2 < 100\ \mathrm{GeV}^2$. Such processes dominate by far the DIS cross section observed in the H1 detector and provide the only access to the low-x part of the proton structure ($x \approx 10^{-4}$). At the same time the calorimeter has to operate in a very high rate environment caused by the illumination of the rear side with secondary hadrons originating from beam-gas and beam-wall interactions of the 820 GeV proton beam. Due to its location within the large solenoid the BEMC is exposed to the full magnetic field of 1.15 T.

A full description of the BEMC and its associated trigger, the backward single electron trigger (BSET) can be found in Ref. [83].

3.2.1. Mechanical layout

The calorimeter elements (stacks) of the BEMC are mounted in an aluminium barrel with a diameter of 162 cm. The front face is located at a distance of 144 cm from the nominal interaction point. Scattering angles θ from 151° to 176° are covered with full azimuthal acceptance. This corresponds to $\approx$ 1.4 units of pseudorapidity η ranging from -2.9 to -1.6.

The granularity of the calorimeter is provided by segmentation into 88 calorimeter stacks aligned parallel to the beam line. The transverse structure can be seen in Fig. 33a. 56 stacks have a square cross section. The remaining ones are of trapezoidal and triangular shapes in order to provide an approximation to the circular shape of the support barrel.

The stacks are multilayer lead-scintillator sandwich structures with 50 active sampling layers made of SCSN-38 plastic scintillator [84] of 4 mm thickness. The entire structure (Figs. 33b and 33c) corresponds to a total of 21.7 radiation lengths or $\approx 1\lambda$. The Moliere radius is 3.4 cm. The scintillation light is coupled via a 0.3 mm air gap to Y-7 wavelength

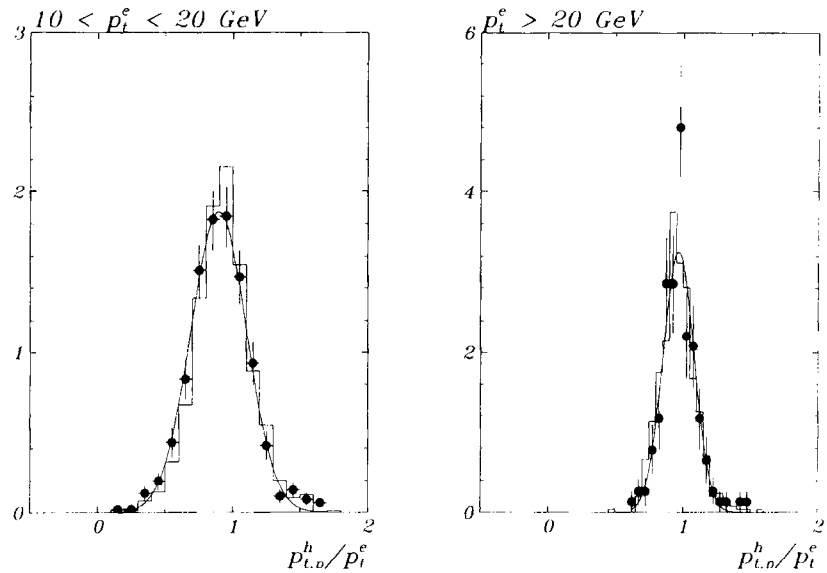

Fig. 32. Transverse momentum balance p_{th}/p_{te} for both scattered electron and hadronic shower detected in the LAr calorimeter for data (open symbols) and Monte Carlo (histogram).

shifter bars [84]. Two pairs of 8 cm wide bars cover two opposite sides of a square stack extending over the full active length. The remaining two sides are covered with 16 cm wide bars extending only over the last 15 sampling layers in the stack, thus providing a twofold segmentation in depth.

The light emitted in the wavelength shifter bars is detected by PIN photodiodes (S2575[19]). Each long bar is equipped with one diode. The short bars are connected to a pair of diodes due to their double width. Special arrangements of wavelength shifters have been made for the non-square stacks. Some of them have a reduced number of read-out channels. In total there are 472 read-out channels in the BEMC.

3.2.2. *Readout electronics and trigger*

The electronics associated with the BEMC must fulfill two main functions. It processes the analog signals from the PIN photodiodes and converts them into digital form with the required speed, precision and stability. It further provides trigger signals.

The signals from the PIN photodiodes are fed into charge sensitive pre-amplifiers mounted directly on the back of each calorimeter stack. The preamplifiers produce fast signals of 100 ns rise time and a fall time of 150 μs. A differential pulse is sent from a line driver through 30 m twisted pair cables to a receiver located in an electronics hut. Here the signals are split to provide input for the calorimetric triggers and for the readout.

Two trigger signals are produced. Firstly the analog signals of the four long wavelength shifter bars within one stack are summed in order to provide input for the high granularity backward single electron trigger (BSET; see Section 5.3.2 in Ref. [1]). A second set of stack sums is being formed to feed the overall calorimeter trigger sums with low granularity. The timing and the gain of the BSET stack sums are individually adjusted in order to assign events uniquely to one bunch crossing and to compensate for stack-to-stack variations in energy calibration already on the first trigger level.

The readout of BEMC energies proceeds through a chain of shapers, sample-and-hold circuits and multiplexing similar to the one of the LAr calorimeter described previously. Due to the large cross section of calorimeter stacks and the high proton beam related background rates the concept of slow shaping to match the trigger level L1 decision after 25 bunch crossings cannot be applied for the BEMC. The probability for a distortion of the energy measurement through pile-up would exceed 50% for a background rate of 100 kHz. To overcome this problem an analog electronics chain consisting of a fast, unipolar shaper and a subsequent analog delay line is used. The shaper has a time constant of 450 ns (FWHM) in order to reduce the pile-up window to about five bunch crossings. To match the trigger decision time the shaped signal is delayed by an analog delay line with a length of 2.4 μs[20]. The fast shaping requires a precise relative adjustment of all 472 delay lines in order to avoid channel-to-channel gain variations of the signal. Equalization of the delay lines to 60 ns is required to keep the gain variations within 1%. The equalization achieved is better than 10 ns so that there is no contribution to the energy scale uncertainty from this source.

[19] Hamamatsu Photonics K.K., Ichino-cho, Hamamatsu City, Japan.

[20] Floeth Electronic, Landsberg a. Lech, Germany.

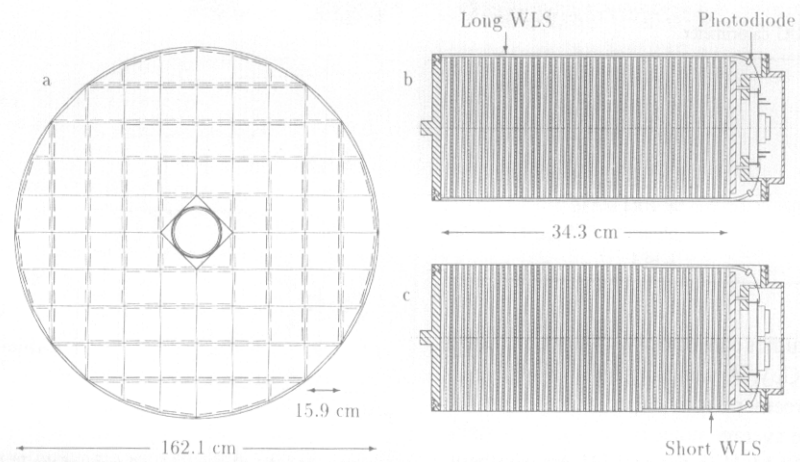

Fig. 33. Transverse view of the BEMC barrel and longitudinal cross sections of BEMC stacks. The positions of all long WLS in the BEMC are marked in (a). The scintillating light is read out transversely via long WLS covering the full length of the BEMC stacks (b). In the square and trapezoid stacks the last 15 sampling layers are read out via short WLS (c).

3.2.3. Calibration

The calibration of the BEMC is based on two contributions. Electronics gain and light collection in the stacks are factorized and monitored independently.

The gain of the electronics chain is determined with a pulser system identical to the one used for the LAr calorimeter. The pulser system measures the response of the entire electronics chain including all cables. It has also been used to transfer the initial absolute calibration from test beams to the final experiment. During data taking periods the entire electronics is calibrated once per week. The stability achieved is better than 0.1%. This is far below other sources of calibration uncertainties.

The second contribution to BEMC calibration is light collection and detection in the calorime-ter stacks. Here the concept is to obtain the initial absolute energy scale from test-beam measurements and to confirm and improve the scale in situ using electrons scattered under small angles from medium/high x_{Bj} partons, i.e. in the kinematic peak.

The initial absolute calibration of individual square stacks has been obtained from measurements with a 5 GeV electron beam at the DESY synchrotron. The individual calibration constants of channels in quadratic stacks differ only slightly with a spread of 6%. This demonstrates the stable and well reproducible construction procedure for the optical part of the calorimeter.

In the environment of HERA e–p collisions the BEMC is exposed to a cross section of 100 nb from DIS. Deep inelastic scattering at small angles from medium/high x_{Bj} partons gives rise to a peak in the distribution of scattered electron energies at the value of the electron beam energy. A method has been devised to use this peak for a precise determination of the calorimeter energy scale for electrons. The method has been successfully applied to the high statistics data sample collected in the 1993 and 1994 running periods [85]. The calibrated energy distribution observed in the BEMC is shown in Fig. 34. The data points are compared to a simulation program taking into account energy losses in dead material as well as spatial inhomogeneities and all known contributions to the energy resolution.

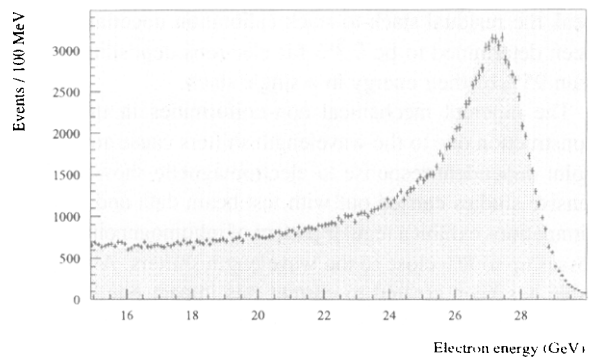

Fig. 34. Energy spectrum of low Q^2 DIS electrons scattered in the region of square BEMC stacks. For simulation (shaded area) the structure function GRV is used.

3.2.4. Performance

The overall electromagnetic energy scale of the BEMC has been determined using the data taken in the 1994 run period. In Fig. 34 a comparison of the measured energy distribution of the leading cluster with a simulated one (shaded area) using the GRV structure function is shown after adjustment of the calibration for each individual stack using the kinematic peak method. Good matching of the data and the simulation proves the quality of the BEMC calibration and of the understanding of the detector response. In the 1994 luminosity period the global energy scale for electrons in DIS was adjusted using the kinematic peak method with a precision corresponding to 1% dominated by systematical errors.

The energy resolution of the BEMC has initially been de-

Table 9
Global parameters of the PLUG calorimeter.

Position	$+476 \leq z \leq +545$ cm
Overall radius	$6 \leq r \leq 32$ cm
Radius of detector planes	$6 \leq r \leq 25$ cm
Polar angular range	$12.5 \leq \theta \leq 58$ mrad
Number of detectors	$8 \times 84 = 672$
Number of electronic channels	$4 \times 84 = 336$
Total length	69 cm $\equiv 4.25\lambda_{abs} \equiv 44.6X_0$
Weight	1.48 t

termined in test beam studies carried out with electron beams ranging from 1 to 60 GeV. A sampling term of $10\%/\sqrt{E}$ has been found in agreement with expectations from the mechanical design. The average noise per calorimeter stack was measured to be 130 MeV in the real H1 environment. Energy clustering is carried out over stack nonets giving rise to a contribution of 390 MeV from noise for each cluster. The constant term in energy resolution for a single stack was found to be 1.7%. Using the observed shape of the kinematic peak the residual stack-to-stack calibration uncertainty has been determined to be 0.3% for electrons depositing more than 95% of their energy in a single stack.

The inherent mechanical non-uniformities in the stack construction due to the wavelength shifters cause an impact point dependent response to electromagnetic showers. Extensive studies carried out with test beam data and shower simulations exhibit a regular pattern of inhomogeneities with losses up to 8% close to the wavelength shifters. A look-up table has been created to correct this impact point dependence. Electrons sharing their energy among many stacks receive an additional contribution of 3% to their effective resolution caused by imperfections in the correction procedure.

The matching of electron tracks measured in the tracking detectors to the cluster position reconstructed in the BEMC has been determined from DIS events with the electron scattered into the BEMC. Based on the known attenuation properties of light in the scintillator plates a position resolution of 7 mm transverse to the beam has been achieved.

Interacting hadrons deposit typically 45% of their energy in the BEMC. A satisfactory hadronic resolution of $\approx 80\%/\sqrt{E}$ has been estimated in detector simulations by combining the measurements in the BEMC and in the instrumented iron structure behind it with proper weighting.

3.3. The plug calorimeter

The plug calorimeter (PLUG) has been designed to close the gap of acceptance for the energy flow measurements between the beam pipe ($\theta \approx 0.6°$) and the forward part of the LAr calorimeter ($\theta \approx 3.5°$). Its main task is to minimise the missing part of the total transverse momentum due to hadrons emitted close to the beam pipe. In addition the energy, emitted into a narrow cone around the beam pipe can be used to separate the proton jet as well as to veto beam

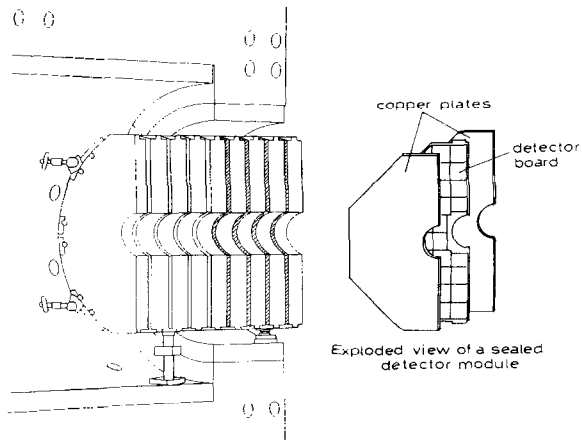

Fig. 35. Cross sectional view of the PLUG calorimeter.

gas and beam wall background.

Owing to the geometrical constraints – the available space inside the return yoke of the H1 magnet was restricted to a cylindrical hole of ≈ 0.7 m length and a diameter of ≈ 0.7 m around the beam axis – only a most compact calorimeter could fit. Facing the physical requirements of good angular resolution, nearly full containment and linearity, the solution was a sampling calorimeter consisting of nine copper absorber plates interleaved with eight sensitive layers of large area silicon detectors [49]. The most important construction parameters are given in Table 9.

Fig. 35 shows a schematic view of one of the two half-cylindrical parts of the PLUG calorimeter, each mounted in one half of the return yoke. The detector modules are placed within 15 mm wide slots between the absorber plates. These are sealed and easy to replace entities, which contain one half of a detector plane each. Between two 5 mm copper plates a G10 readout board, equipped with 42 silicon detectors of 400 μm thickness, is placed (Fig. 35, left part). A detailed description of the detector technology can be found in Ref. [86]. Typical characteristics of single silicon detectors, as measured in the laboratory, are given in Fig. 36. Due to a special edge-protection procedure 32 quadratic (5×5 cm^2), six triangular and four rectangular detectors cover one half of the detector plane in a mosaic structure nearly completely, leaving only 4% of the total area inactive. A total of 672 detectors have been installed.

The readout electronics of the PLUG are included in the analog chain of the H1 calorimeters and use the same components (see Section 3.1.6). The 672 detectors are read out in 336 pairs of channels. Trigger towers are built by merging the signals from subsequent channels in the z-direction.

The calibration of the ADC output in units of visible energy rests on an absolute energy measurement using α-particles. Its conversion into total absorbed energy is based on detailed MC-simulation studies of electromagnetic and hadronic shower developments in silicon instrumented calorimeters in comparison with test measurements [87–91].

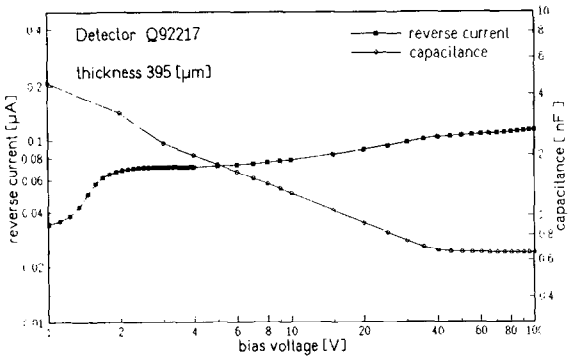

Fig. 36. Typical I/V- and C/V-characteristics of the PLUG Si-detectors.

Since March 1994 the PLUG was operated with 8 instrumented detector planes. During luminosity operation sharp increases of detector dark currents up to 15% were observed which could be correlated with failures of HERA machine components and consequential increase in proton-related backgrounds (see Refs. [92,93]).

The energy resolution of the PLUG calorimeter suffers from both the amount of dead material in front of the device and the energy leakage. Nevertheless its value of about $150\%/\sqrt{E}$, evaluated from experiment supported MC-calculations [90], turns out to be sufficient for the tasks within the H1 experiment. As an illustration of the PLUG-calorimeter response to selected low-Q^2 events the distribution of the total energy is shown in Fig. 37. It compares remarkably well with MC-simulations produced using the Colour Dipole Model (LEPTO 6.1 MEAR, see Ref. [94]).

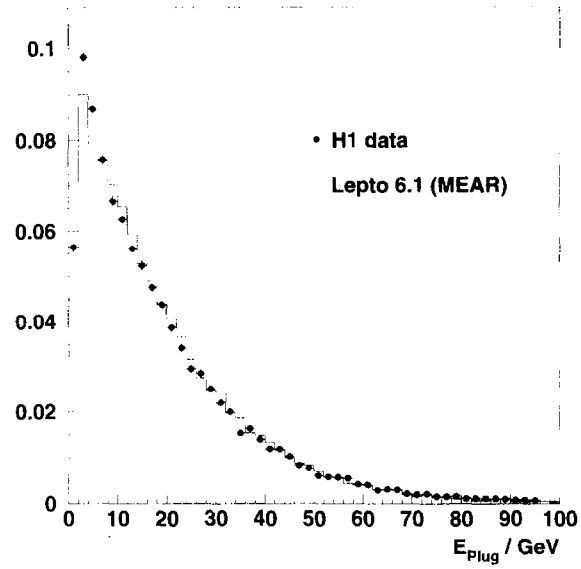

Fig. 37. PLUG response to e-p events compared to a MC simulation (solid line) produced using the colour dipole model.

3.4. The tail catcher (TC)

In order to measure the hadronic energy leaking out of the LAr calorimeter and BEMC, eleven of the sixteen limited streamer tube (LST) layers of the instrumented iron are equipped with readout electrodes (pads, see also Section 4). Here we describe the features of the LST tail catcher (TC) relevant for the energy measurement which is based on the analog readout of the pad signals. For more details see Ref. [95].

The pad sizes vary from $28 \times 28\,cm^2$ in the endcaps up to about $50 \times 40\,cm^2$ in the barrel region. The pad signals from the five inner (six outer) layers are summed up by tower builders (TB) to form the front (back) tower signals. The differential analog signals from the TBs are then relayed in groups of 12 to the cable stations (CS) which reorganize the signals from the towers into groups of 16. From there the signals are sent to the analog superboards (SB) whose function is to amplify, integrate and store the analog signals in groups of 128 channels each. The geometry of the tower structure is briefly described in Table 10.

Table 10
Layout of the pad readout of the iron instrumentation.

Region	θ range	Segmentation	No. of channels
Forward end cap	$6° \leq \theta \leq 33°$	x and y	552
Central barrel	$33° \leq \theta \leq 137°$	ϕ and z	2784
Backward end cap	$137° \leq \theta \leq 172°$	x and y	552

3.4.1. Electronics

The amplifier used on the TB-boards allows for the measurement of single muons as well as hadronic showers without saturation. The signals have a dynamic range of 0.75 mV to 1 V. Each superboard accepts the input of 128 channels which are individually processed by a line receiver, shaper and sample & hold. The line receiver and shaper are modified versions of the LAr calorimeter system cards, while the sample & hold cards are identical to those used in the LAr readout system. The signals are multiplexed and held in the output buffer to be read by the analog receiving unit (ANRU). The data are then zero suppressed and corrected in the DSP and read out (see Section 3.1.6).

The calibration of the superboards is done by sending calibration pulses through the analog readout chain beginning at the tower builder board. The calibration constants are downloaded into the DSPs to correct for the channel to channel variations and non-linearities. Channel to channel variations are less than 2% for 3888 channels.

During data taking and calibration, acquisition is controlled by the LAr calorimeter OS9 system. Normal data and calibration results can also be collected in stand-alone mode, in which case the local TC test station is used.

3.4.2. Energy calibration

The conversion of the signal charge Q_i, as measured in a tower i, to hadronic energy $E_{\mathrm{had},i}$ is given by [96]:

$$E_{\mathrm{had},i} = c_1 c_{3,i} Q_{\mathrm{had},i} / c_2 .$$

The general hadronic energy calibration constant c_1 has been determined in test measurements at CERN using pion and muon beams [97]. The parameter c_2 gives the tower charge of an average minimum ionizing particle, i.e. a muon, at an angle of incidence of 0° with respect to the normal of the LST chambers. The intercalibration factor for each tower, $c_{3,i}$, describes the tower to tower variations of the measured charge.

The constant c_1 is derived from the linear relationship between the incident pion energy and the ratio Q_π/Q_μ of the measured charge for pions and muons. Defined in this way c_1 is essentially determined by the sampling fraction of the calorimeter and the gas used in the chambers. It does not depend on the angle of incidence of the hadrons and is also insensitive (in wide limits) to the operating conditions [97]. The parameter c_2 and the charge $Q_{\mathrm{had},i}$ on the other hand vary with high voltage, pressure, gas composition and temperature. Since the atmospheric pressure is the only one of these operating parameters which can change rather quickly, we compensate for this effect by regulating the high voltage (see Section 4.1.3 of the muon system).

The transformation of ADC counts into charge is done online during the readout process according to

$$Q_i = p_{1,i}(\mathrm{ADC}_i - p_{0,i}) .$$

The pedestals $p_{0,i}$ are obtained from random triggers and the gains $p_{1,i}$ are given by the slope of the test pulser response curves of the electronic calibration. Both varied by $< 2\%$ over the whole data taking period. Zero suppression allows to read out only pads above a certain threshold.

The parameters c_2 and $c_{3,i}$ are determined from cosmic muons [98], triggered by opposite pairs of barrel or endcap modules in special cosmic runs. The data have to be corrected for non-normal incidence with respect to the chamber plane. In order to keep the corrections small, only tracks with $\tan\theta < 0.8$ are considered in the calibration procedure. The intercalibration constants $c_{3,i}$ vary by $\sim$ 10% within one module. There are larger module to module variations depending on the module location in the iron yoke, mainly due to different gas temperatures and pad sizes.

3.4.3. Performance

The performance of the tail catcher has been studied in test measurements at CERN with π and μ beams of 10 to 80 GeV [97]. The energy response for single pions is linear up to at least 40 GeV and the energy resolution is $\sigma/E \simeq 100\%/\sqrt{E}$.

The calibration of the tail catcher at HERA is done by cosmic muons as described above and taking the energy scale from the CERN test results as $c_1 = (0.233 \pm 0.002)$ GeV. Fig. 38 shows representative muon spectra of a complete module for the inner and outer towers. Clean muon signals can be seen with mean values far beyond the pedestals. The widths relative to the most probable values are $\sim$ 35%. The ratio of the mean values of inner and outer towers corresponds to the expected value of 0.8. We do not observe any effect of the magnetic field in the iron yoke on the muon signal. The intercalibration constants vary among the detector by $\sim$ 20% (mostly due to a vertical temperature gradient within H1) with a long term stability of $\sim$ 10%. They are regularly measured with cosmic muons.

Important for energy measurements with the H1 detector is the combination of the tail catcher with the LAr calorimeter. The energy response can be symmetrized and the energy resolution can be improved by including the information of the tail catcher [58,82,64]. Corrections for energy losses in dead materials have to be done for each event. Inside the tail catcher dead material appears as cracks between towers, in particular in the transition region between the end cap and barrel yoke. Corrections between adjacent towers are calculated using the ratio of the tower areas with and without the crack as correction factor. More involved corrections are necessary for the material between the calorimeters, e.g. the cryostat wall and coil between the LAr calorimeter and the TC. For this purpose a hadronic object in the LAr calorimeter is geometrically linked with a TC cluster into a generalized cluster. The energy losses are estimated [82] by a linear interpolation of the energy deposit in the last layer of the LAr calorimeter $E_{\mathrm{LAr,last}}$, and the first layer of the tail catcher, $E_{\mathrm{TC,first}}$:

$$E_{\mathrm{loss}} = \alpha(\theta)(E_{\mathrm{LAr,last}} + 0.5 E_{\mathrm{TC,first}}) .$$

The calculated energy loss is distributed among the cells in proportion to their energy contents. The function α depends on the polar angle θ of the shower or, more precisely, on the thickness Δt_{dead} of the material between the two calorimeters and are almost independent of the energy over a large range. It has been determined as a function of Δt_{dead} from dedicated test measurements at CERN [82]. At H1 Δt_{dead} varies from 0.5 up to 2.4 interaction lengths depending on the polar angle θ. The corresponding values for α range from 0.1 up to 1.1. The uncertainty of the energy correction was estimated to $\sim$ 20%. Fig. 29 shows the effect of the combined LAr and TC measurements with energy loss corrections from test beam results.

Calibration and correction procedures have been successfully transferred from the test beam measurements to the H1 detector at HERA, where the balance of the transverse hadronic energy p_{th} and the transverse electron energy p_{te} in neutral current events can be used to check the overall hadronic calibration. Fig. 39 shows the ratio $p_{\mathrm{th}}/p_{\mathrm{te}}$ of p_{th} as measured with the hadronic section of the LAr calorimeter and the TC (including the above mentioned corrections) and p_{te} as measured with the electromagnetic section of the LAr (or BEMC) versus the energy fraction deposited in the

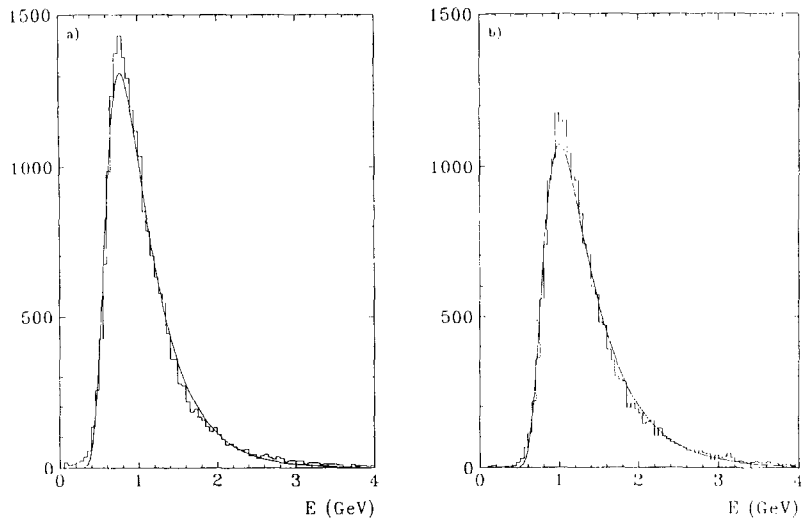

Fig. 38. Muon spectra summed over a complete module for (a) inner towers normalized to 4 planes, and (b) outer towers normalized to 5 planes. The curves are fits to a Landau distribution.

TC. The distribution is flat, demonstrating that calibration and corrections have been treated properly.

4. Muon system

4.1. Iron instrumentation

4.1.1. The limited streamer tubes

The iron yoke of the main solenoid magnet surrounds all major detector components of H1. It is interleaved with slits which are equipped with limited streamer tubes (LST). They serve as hadronic tail catcher and for the measurement of penetrating tracks. Luranyl [99] was used to build the chambers since PVC tubes [100] were excluded for safety reasons [101]. Luranyl is a halogen free plastic material which can be extruded with sufficient precision. It can also be coated with the graphite paint needed to obtain the required surface resistivity. Some features are listed in Table 11.

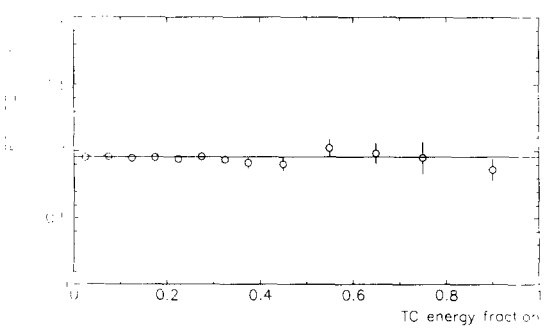

Fig. 39. Ratio of the total transverse hadronic energy – including the corrected TC energy – and the transverse electron energy versus the energy fraction in the TC, for NC events. The line is a fit to the data.

The basic chamber elements are extruded eightfold profiles with a cell surface size of 10×10 mm^2. The mechanical precision achieved is 0.1 mm, the straightness of the profiles is better than 1 mm per m. The profiles are coated with graphite paint to yield a low surface resistivity of $\approx$ 10–30 k$\Omega/\square$. The HV is applied to this surface. A silver coated Cu–Be wire of 100 μm diameter is at ground potential. The wire is kept in place by spacers every 50 cm. The profiles are closed with a Luranyl cover with high resistivity of $\approx$ 10 M$\Omega/\square$. The profiles are grouped by pairs in a gas tight box of Luranyl. All connections to the chamber are provided on one end of the box. Several boxes are put together to form a complete streamer tube layer. On the high resistivity side planes of either strips or pads are glued onto the boxes containing 16 active elements. The layers are put onto an aluminium plate and wrapped into a nonconducting foil to guarantee electrical insulation.

A schematic view of the basic structure is given in Fig. 40, while Fig. 41 displays the configuration of the planes within the iron together with an indication where strips and pads are located. As an example, the instrumentation of a barrel octant is shown. Starting from the interaction point there is first a so-called muon-box installed in front of the iron containing three layers (two layers with strips perpendicular to the wire direction and a third layer with pads). Pad layers are also installed in the first three iron slits. The fourth slit is twice as wide as the others and houses a strip and a pad layer.

Table 11
Basic properties of Luranyl [99].

Density	1.06 g cm^{-3}
Thermal expansion (23–80°C)	0.6–0.7 $\times$ 10^{-4}
Surface resistivity	10^{14} Ω
Softening point	100°C

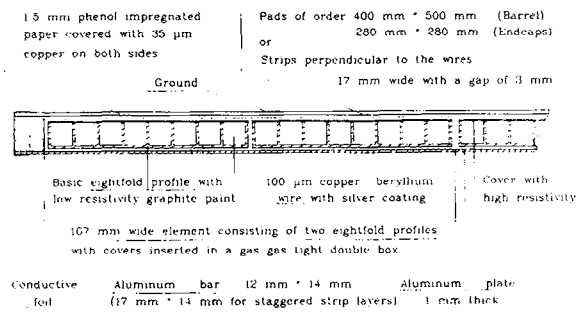

Fig. 40. Structure of LST chambers.

Pad layers are inserted in the remaining five slits. Behind the iron is a second muon-box with three planes.

The signals of consecutive pads are added (5 inner + 6 outer layers) providing two-fold energy sampling in depth. All wire- and strip-signals are read out digitally. Three dimensional space-points from tracks can be obtained in the three chambers equipped with strips. Table 12 lists some parameters of the LST detector.

4.1.2. Gas system

Due to safety requirements the chambers are operated with a non-inflammable three component gas mixture of CO_2, argon and isobutane with relative volume fractions of 88%, 2.5%, and 9.5%. The total gas volume amounts to 36 m^3. Different parallel circuits supply the detector with gas. The flow in each branch can be adjusted with needle valves and is measured with computer readable flow meters. 192 branches are used including some spare and test branches. The number of chambers connected serially was chosen such that the total gas volume per branch does not exceed $\approx$ 200 l. The gas composition, in particular the isobutane content, is controlled by two monitors. The gas flow is stopped and the HV is switched off if the fraction of isobutane is outside the range 8.5% to 9.9%

The gas quality is also monitored by two LST chambers equipped with a ^{90}Sr source, one in the incoming and one in the outgoing gas flow. The pulse height spectra of these chambers allow the monitoring of the gas composition and the HV regulation.

4.1.3. High voltage system

Five high voltage crates [102] with a total of 200 independent HV channels are used. Each channel supplies between 20 and 110 profiles. Chambers within one gas circuit are connected to the same HV channel. A passive distribution system allows to disconnect each single profile from HV in case of problems. All switches are computer readable, such that the HV configuration of each single 8-fold profile can be stored in a database.

Table 12
The LST detector.

Total size	4000 m^2
No. of profiles	13000
No. of wires	103000
No. of strips	28700
No. of analog channels	3888
Angular coverage	$6° \leq \theta \leq 172°$

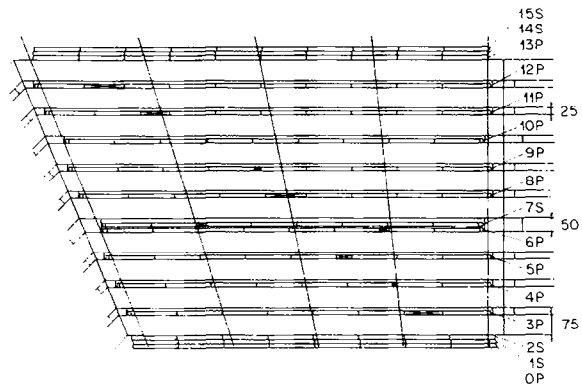

Fig. 41. Iron instrumentation showing the pointing pad structure of the barrel region. The crossed elements represent dummy modules which fill the space not occupied by the chambers in a way to ensure that the dead areas are not aligned for tracks from the vertex region (P = pads; S = strips).

Two different reference voltages can be applied to the detector. One is selected to be well below working conditions at V_1 = 3000 V. This setting is activated during unstable beam and injection conditions. The normal operating voltage is set to V_0 = 4500 V at normal pressure. Since the charge gain of streamer chambers depends on the pressure we adjust the high voltage accordingly. The gain variation amounts to $dQ/Q = -1.73\% dP/\text{hPa}$. The high voltage V_0 is automatically adjusted by +2.75 V/hPa. In Hamburg one observes pressure changes of up to $\approx$ 6 hPa/h, and total variations of 80 hPa are possible.

Other relevant parameters such as temperature are monitored. They remain constant over long periods. The currents of all HV channels are constantly monitored. If a channel draws more than 5 μA, the corresponding voltage is automatically reduced until this current is below 5 μA. Channels are switched off, if this limit is exceeded for more than one minute.

4.1.4. Readout system

The readout of the analog information is incorporated as part of the LAr calorimeter and is discussed in Section 3.4. A digital readout system was developed for the wire- and strip-readout. Each wire (strip) is connected to a comparator, a synchronization circuit and a digital pipeline. The wire signal is digitized according to a computer adjustable threshold, synchronized with the HERA bunch crossing frequency and fed into a digital pipeline which has a depth of 32 steps corresponding to a total storage time of $\approx$ 3.1 μs.

The front-end logic for eight data channels has been integrated in a gate array [103]. The leading edge of the input signal clocks the first flip-flop of a dead time-free synchronization circuit. The synchronized data patterns are buffered

in a pipeline register. As soon as a trigger is accepted, the filling of pipelines is stopped. By means of a remotely controlled signal it can be decided whether the data pattern of one time slice, or the logical OR of two adjacent time slices is read out. This is necessary since the signal propagation within the chambers can exceed 96 ns, the time between two bunch crossings. In addition the eightfold OR of the stored data pattern is clocked into a separate flip-flop of the readout chain providing a signal for trigger purposes.

The electronics for 16 channels is housed on a readout card which is directly mounted onto the streamer chamber layers. This allows for early digitization and thus provides high noise resistance and a significant reduction in the number of cables needed. Multiple readout cards can be daisy chained. A layer of chambers is read out serially. The readout chains of a maximum of 24 layers are connected to special VME-based readout controllers (ROC) which provide zero suppression, data encoding, and submit all relevant steering signals to the readout cards.

Upon arrival of the first level trigger (L1), the ROCs start to collect the data from the electronics. The absolute position of the data corresponding to the triggered event within the front-end pipelines depends on the decision time of the trigger and the distance between the central trigger logic and the respective chambers. Due to the physical dimensions of the detector the delay is different for different areas.

One ROC serves up to 12 300 digital channels corresponding to 24 chamber planes with 512 channels each. Since we operate 64 of these ROCs simultaneously less than 300 μs are needed to collect all data.

The architecture of the local DAQ environment is given in Fig. 42. The VME crates are distributed in five clusters around the detector. The readout of these units starts after a second level trigger (L2). VME processors collect the data which are then stored locally. The data of up to 20 events can be stored before they are delivered to the central H1 data acquisition system.

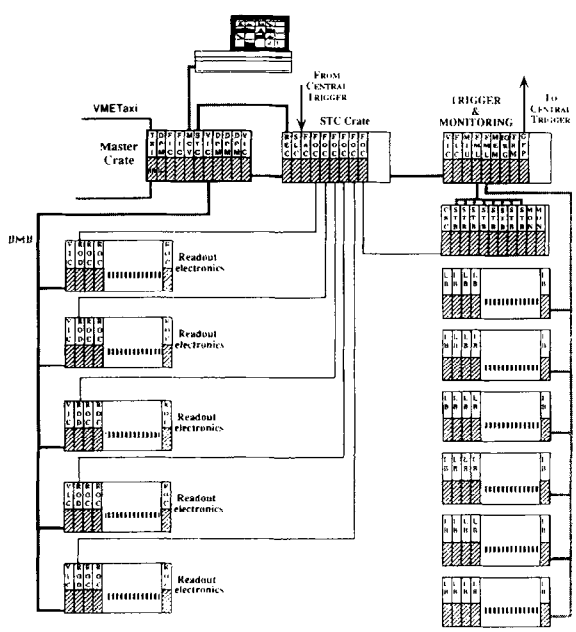

Fig. 42. The local data acquisition system.

4.1.5. Track reconstruction

The track reconstruction uses 16 wire, 5 strip and 11 pad layers, the latter being combined into 2 towers. The wires measure up to 16 points in the so-called "wire plane" and the strips up to 3 points in the perpendicular "strip plane". The resolution for wire and strip hits is 3–4 mm and 10–15 mm respectively. The pads define coarse areas in space with a precision of about 10 cm.

The pattern recognition starts with the 16 wire layers. Track segments are parametrized by straight lines. To get curved track candidates several segments are connected. Then the pattern recognition selects track segments in the strips which have a matching wire track candidate. These matching wires and strips are then combined to a three dimensional track. In case of ambiguities the pad information is used to resolve them. The combination which fits best to the pads in space and amplitude (analog pad charge divided by number of wires hit) is chosen. The towers are then assigned to their matching wire and strip combination.

Due to crosstalk along the wires usually more than one pad gets a signal. With the centre of gravity of the pad charge the coordinate along the wires can be measured for both towers with an accuracy better than 10% of the pad size. With these two additional points a direction in the strip plane can be determined even for very short tracks.

The magnetic field $\boldsymbol{B}(\boldsymbol{r})$ varies strongly inside the iron plates and in the gaps. The energy loss in one plate is on average 80 MeV for muons at perpendicular incidence. The track fit uses an average magnetic field for each plate and gap and performs a least squares fit simultaneously to wire, strip and tower readings. The effect of the energy loss is accounted for by an iteration procedure.

4.1.6. Performance

During operation typically 0.1% of the digital channels (wires, strips) are noisy and 1–2% are dead.

Calibration data were taken during cosmic runs. One re-

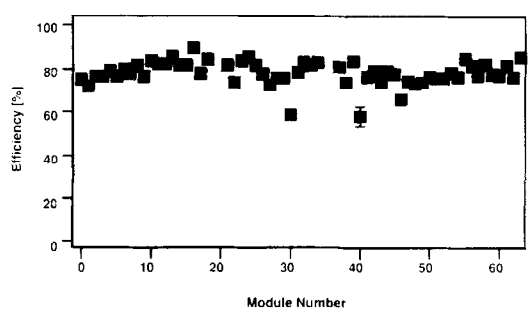

Fig. 43. Efficiency of chamber planes. The following numbering scheme is used: 0–15 backward endcap (from bottom to top), 16–31 backward barrel, 32–47 forward barrel, 48–63 forward endcap (from bottom to top).

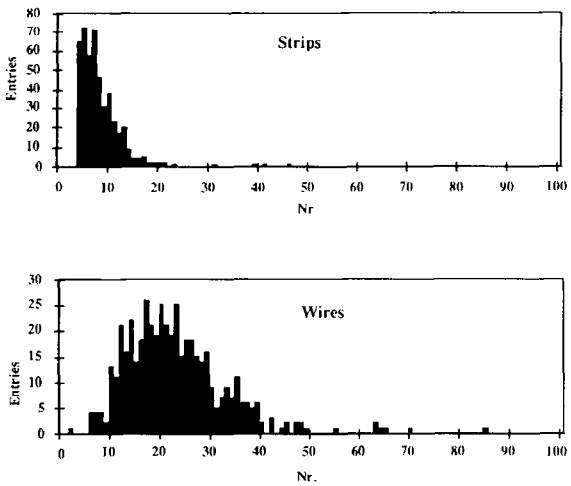

Fig. 44. Wire and strip multiplicity per event.

sult is the efficiency of the chambers, which is shown in Fig. 43. It agrees well with the expected values. Fig. 44 shows the number of wires and strips per event for events triggered by the muon system. The wire data show a signal starting at a multiplicity of 13 which is roughly the mean number of wires expected for single penetrating muons with a plane efficiency of 80%.

With cosmic muons the chambers of all modules have been aligned to each other with an accuracy of a few mm. In the barrel region cosmic muons can be used to determine the reconstruction efficiency by extrapolating jet chamber tracks. The geometrical acceptance limits this efficiency to 89% in the plateau region above the threshold of 2 GeV as shown in Fig. 45.

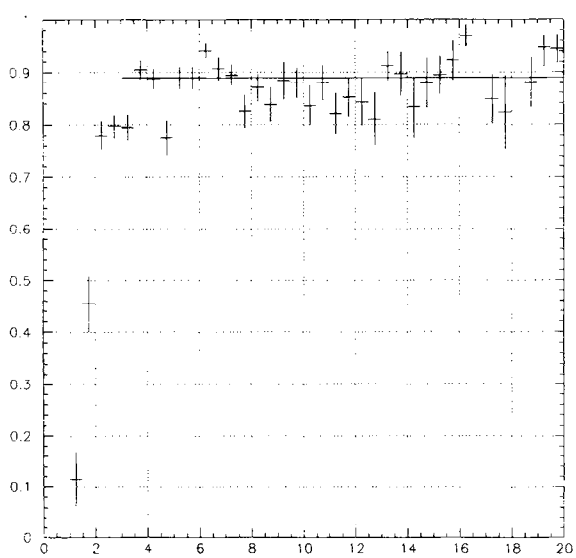

Fig. 45. Muon reconstruction efficiency in the barrel region as function of the muon energy [GeV] determined from cosmic muons. The average efficiency in the plateau region is 89% and is determined by the geometrical acceptance.

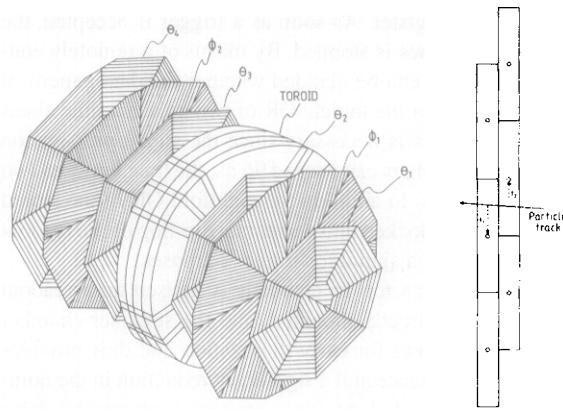

Fig. 46. (a) A schematic view of the forward muon spectrometer and (b) the cell structure of a double layer.

4.2. Forward muon spectrometer

4.2.1. General description

The purpose of the forward muon spectrometer is to measure high energy muons in the range of polar angles $3° \leq \theta \leq 17°$. The detector consists of drift chamber planes mounted on either side of a toroidal magnet. The design aim was to measure the momenta of muons in the range between 5 GeV/c and 200 GeV/c, the lower limit being given by the amount of material the muons have to penetrate and the influence on the momentum resolution of the multiple Coulomb scattering in the magnet iron. The upper limit is set by the magnetic field strength of the toroid together with the spatial resolution of the drift chambers. The expected momentum resolution at 5 GeV/c is 24% and deteriorates slowly to 36% at 200 GeV/c. Muon momenta below 5 GeV/c are measured in the forward tracker.

Fig. 46a shows schematically the detector arrangement and the toroid magnet. The latter is described in Section 3.4 of Ref. [1]. The drift chamber planes, which increase in size from about 4 m diameter for the first detector plane to 6 m diameter for the last, are all divided into octants of individual drift cells mounted on Al-frames. The orientation of the drift cells is such that four of the planes essentially measure the polar angle (θ) and thereby provide the momentum of the traversing muon while the remaining two measure the azimuthal angle (ϕ). Each plane consists of a double layer of drift cells staggered by half a cell width (Fig. 46b). This arrangement enables the resolution of left-right ambiguities and also the determination of t_0 as will be explained below. The total number of drift cells is 1520.

4.2.2. Chamber design

All drift cells have a rectangular cross section with a depth of 2 cm, a width of 12 cm and lengths between 40 cm and 240 cm. With a central sense wire the maximum drift distance is 6 cm. The cells have 50 μm thick Nichrome wires except for the inner short cells where the diameter is 40 μm. For cells longer than 1.5 m there is a wire support

in the middle. More details can be found in Ref. [104].

The chamber signals are amplified, digitized and read out using the same components as all other drift chambers within the H1 detector (see Section 2.4).

4.2.3. The chamber gas and high voltage system

The choice of gas for the drift chambers was determined by several requirements. One is the desire to work in a drift voltage range where the drift velocity is constant. Further the gas has to be fast enough for the pulse to arrive in time for the trigger and finally it should be non-flammable for safety reasons. Currently a mixture of 92.5% argon, 5% CO_2 and 2.5% methane (FMS gas) has been chosen for the chambers. The gas is mixed and purified in a recirculator. The chambers have a total gas volume of 4 m^3, and with a small overpressure of about 0.2 hPa measured at the output, the return gas flow is typically 90% of the input and the oxygen content is of order 100 ppm. More details can be found in Ref. [104].

A 120-channel high voltage system [102] supplies distribution boxes on the detector with high voltage via 50 m long coaxial cables. Two different modules are used, one (6 kV, 1 mA) supplies the drift voltage and the other (8 kV, 200 μA) supplies the sense voltage. One drift channel supplies voltage to an entire octant, feeding 20–40 individual resistor chains. One sense channel supplies voltage to all but the 12 innermost cells of a θ-octant and the central section of the ϕ-octants. These cells have another sense channel, which can be set to a lower voltage in case of bad beam conditions. Additionally, for the ϕ-octants, the central section which is close to the beam tube can be moved outwards mechanically, if necessary.

There is a continuous monitoring of the gas composition and flow rates as well as of the high voltage and the toroid magnet, communicated via an Apple Macintosh II ci in the control room. From this work station it is also possible to control the high voltage of the detector.

4.2.4. The charge-time analysis

Only the rising edge and peak region of a pulse are used to get the time and charge information. A pulse is said to start when there are two successively rising digitizings above threshold (see also Section 2.4.5).

The end of a pulse is taken as the second successive digitizing after the peak which is below threshold, or eight 9.6 ns time bins from the start of the pulse, whichever occurs first. The arrival time of the pulse is obtained by extrapolating a line fitted to the steepest part of the leading edge back to the intercept with the background level. With a test set up, looking at cosmic muons, this method gave a resolution of < 200 μm. This result was obtained with a gas mixture of 90% argon and 10% propane providing a drift velocity of 4 cm/μs [104]. However, to satisfy the gas requirements specified in Section 4.2.3 we have chosen the FMS-gas with a drift velocity of ~ 5 cm/μs, resulting in an expected resolution of ~ 250 μm. Pairs of pulses which originate from the same hit are associated by requiring the difference of their arrival times to be less than the full propagation time through the two sense wires and the linking resistor.

The collected charge is found by integrating the digitizings of the pulses from the two wire ends over intervals of the same length, with subtraction of a constant background. A correction for fractional time bins was found to be important since the start times for the two pulses are subject to variable propagation delays. With cosmic muons in the test set up we found a charge-division versus distance characteristic linear to about 1%, which is well matched to the resolution.

4.2.5. Track reconstruction

The space points obtained from the charge-time analysis of the chamber hits are used in a three step procedure for track reconstruction which starts with the pairing of hits in each double layer followed by association of pairs into straight track segments and finally the linking of track segments through the toroid to form full tracks and thus provide a momentum measurement. Pair finding in the double layers is decisive due to the displacements of cells which results in the sum of drift times being a constant (compare Fig. 46b). A vertex pointing requirement is applied as selection criteria, but also unpaired hits are kept to be considered in the track segment finding where we demand 3 out of 4 hits in the θ-layers. The measuring errors of the space points for a pair define a cone which is extrapolated to the other θ-layer on the same side of the toroid. In the area defined by the cone, hits are tried for segment fits and are selected by a χ^2-cut.

For the linking procedure each pre-toroid segment is tracked through the magnetic field of the toroid, taking into account energy loss and multiple Coulomb scattering in the magnet iron. By doing this for a minimal reconstructible momentum of 2.5 GeV/c in the spectrometer and for either of the two muon charges possible, regions in the θ-layers after the toroid are defined inside which segment candidates for linking are considered. From the crossing angle of two linked segments an estimate of the momentum is made. Starting from the pre-toroid segment and the estimated momentum the tracking is repeated as the momentum is changed in small steps around the estimated value. Each post-toroid segment obtained from the tracking is compared to the actual segment found and a χ^2 is calculated. The minimum of the χ^2 variation with momentum defines the momentum corresponding to the best fit.

4.2.6. Drift velocity and t_0-determination

Beam halo muons are used to determine the drift velocity. From the uniform population of the total number of tracks (N) over the full drift distance (Δy), recorded in a run, a rectangular distribution is expected if the drift velocity is constant. However, due to field variations close to the sense wire, the dependence on the angle of the track, the

possibility of tracks traversing only the corner of a cell etc., the drift velocity will be altered and causes a smearing of the distribution.

t_0 is determined from the specific geometry of the detector, making true specific check sums for each track, as detailed in Ref. [104]. The widths of the check sum distributions can be used to find the spatial resolution of the chambers.

4.2.7. Chamber alignment

The drift chambers must be aligned with respect to each other and to the rest of the detector. The cells of a θ-layer are positioned on its supporting Al-frame to a precision of $\sim 50\ \mu$m along the drift direction and to ~ 1 mm in the two other directions. This is better than the achievable resolution and therefore we only have to consider the alignment of the full octants.

Simulation studies and analysis of a small sample of real data have shown that beam halo tracks are suitable for providing the two translational and one rotational quantities which are needed to specify the position of the octant in the plane transverse to the beam direction. Further studies with angle tracks together with the survey will determine the relative positions of the octants along the direction of the beam.

Acknowledgements

We appreciate the immense effort of the engineers and technicians of the participating laboratories who designed, constructed and maintain the detector. We are grateful to the HERA machine group whose outstanding efforts contribute to making this experiment possible. We thank the funding agencies for financial support. The non-DESY members of the collaboration also express their thanks the DESY directorate for the hospitality extended to them. We acknowledge the help of DESY and CERN in providing test beam time for the many calibration runs. The help of the computing centres at DESY and at CERN in the test and running phases is highly appreciated.

References

[1] I. Abt et al., this issue, Nucl. Instr. and Meth. A 386 (1997) 310.
[2] I. Abt et al., The H1 Detector at HERA, Internal Report DESY H1-96-01, Hamburg (1996), unpublished.
[3] J. Bürger et al., Nucl. Instr. and Meth. A 279 (1989) 217.
[4] J. Bürger, Tracking at H1 in the environment of HERA, Proc. 4th Topical Sem. on Exp. Apparatus in High Energy Particle Physics and Astrophysics, San Miniato, Italy, 1990, eds. P. Giusti et al. (World Scientific, Singapore, 1991) p. 272.
[5] H. Drumm et al., Nucl. Instr. and Meth. 176 (1980) 333.
[6] Glass fiber reinforced epoxy: Stesalit AG, Zullwil, Switzerland; and Permali, F 54320 Marseille, France.
[7] S. Prell, Z-Kalibration und dE/dx-Kalibration der zentralen Spurkammer des H1 Detektors, Diploma thesis, University of Hamburg (1992), H1 report FH1T-92-04, DESY, Hamburg, 1992, unpublished.
[8] V. Karimäki, Fast code to fit circular arcs, Helsinki University report HU-SEFT-1991-10, 1991, unpublished.
[9] V. Lioubimov, Particle separation by likelihood analysis of dE/dX measurements in H1 tracking chambers, H1 report 11/93-329, DESY, Hamburg, 1993, unpublished.
[10] C. Ley, Untersuchungen zur Rekonstruktion des radiativen D^{*0} Zerfalls im H1 Detektor, Ph.D. thesis, RWTH Aachen, 1994, unpublished; RWTH Aachen report PITHA-91-10 (1991).
[11] N. Sahlmann, Reconstruction of Λ and K^0_S with the H1 detector, H1 report 04/93-281, DESY, Hamburg, 1993, unpublished.
[12] R. Luchsinger and C. Grab, Comput. Phys. Commun. 76 (1993) 263.
[13] H.J. Behrend and W. Zimmermann, A hardwired trigger processor using logic cell arrays (XILINX), Ref. [105], p. 237.
[14] Rohacell 51: Roehm GmbH, Darmstadt, Germany.
[15] S. Egli et al., Nucl. Instr. and Meth. A 283 (1989) 487.
[16] P. Robmann et al., Nucl. Instr. and Meth. A 277 (1989) 368.
[17] P. Robmann, The central inner z-chamber of the H1-experiment at HERA, Ph.D. thesis, University of Zürich (1994).
[18] California Fine Wire Company, Grover City, CA 93433, USA.
[19] K. Esslinger and P. Robmann, A sensitive current monitor for drift chambers, Nucl. Instr. and Meth. A 334 (1993) 649.
[20] H. Bärwolff et al., Proc. 4th San Miniato Topical Seminar on Experimental Apparatus for High-Energy Physics and Astrophysics, 1990, eds. P. Giusti et al. (World Scientific, Singapore, 1990) p. 284.
[21] H. Bärwolff et al., Nucl. Instr. and Meth. A 283 (1989) 467.
[22] H. Bärwolff et al., Nucl. Instr. and Meth. A 294 (1990) 117.
[23] S. Burke et al., Nucl. Instr. and Meth. A 373 (1996) 227.
[24] NOMEX: Eurocomposites, L 6401 Echternach, Luxembourg.
[25] G.A. Beck et al., Nucl. Instr. and Meth. A 283 (1989) 471.
[26] H. Graessler et al., Nucl. Instr. and Meth. A 283 (1989) 622.
[27] H. Graessler et al., Nucl. Instr. and Meth. A 310 (1991) 535.
[28] J.M. Bailey et al., Nucl. Instr. and Meth. A 323 (1992) 184.
[29] H. Graessler et al., Nucl. Instr. and Meth. A 323 (1992) 401.
[30] W. Zimmermann et al., A 16 channel VME flash ADC system (F1001-FADC), H1 internal report, DESY, Hamburg, 1989, unpublished; manufacturer: Struck, Tangstedt/Hamburg.
[31] H. Krehbiel, H1 trigger control system, H1 report 12/88-101, DESY, Hamburg, 1988, unpublished.
[32] M. de Palma et al., Nucl. Instr. and Meth. 216 (1983) 393.
[33] J. Boucrot et al., Nucl. Instr. and Meth. 176 (1980) 291.
[34] DAG and Electrodag graphite solutions: Acheson Colloiden, Scheemda, Netherlands; Deutsche Acheson Colloids, Ulm, Germany.
[35] K. Müller et al., Nucl. Instr. and Meth. A 312 (1992) 457.
[36] G. Bertrand-Coremans et al., Nucl. Phys. B (Proc. Suppl.) 16 (1990) 518.
[37] P. Huet, A VMEbus-based Data Acquisition System for the MWPCs of the H1 Detector at the HERA Collider, Ph.D. thesis, Université Libre de Bruxelles, 1993, unpublished.
[38] G. Kemmerling, Untersuchungen zur Beimischung von Alkoholdampf in geschlossene Gaskreisläufe für den Betrieb von Drift- und Proportionalkammern, Diploma thesis, RWTH Aachen, 1990, unpublished.
[39] S. Masson, Ph.D. thesis, RWTH Aachen, 1993, unpublished.
[40] J.A. Kadyk, Nucl. Instr. and Meth. A 300 (1991) 436.
[41] R. Etienne, Diploma thesis, RWTH Aachen, 1993, unpublished.
[42] H.B. Dreis, Bau einer automatisierten Gaschromatographie Messtation für den H1 Detektor, Diploma thesis, RWTH Aachen, 1991, unpublished.
[43] W.A. Dietz, Response factors for gas chromatography, Esso Res. and Eng. Co., Analytical Res. Div., Linden, New Jersey, 68 (1967).
[44] V. Commichau, RWTH Aachen III. Physik. Inst. Lehrstuhl B, internal report, unpublished.
[45] P. Göttlicher, Entwicklung und Bau eines rechnergesteuerten Gassystems für eine Präzisionsdriftkammer, Ph.D. thesis, RWTH Aachen, 1993, unpublished.
[46] C. Leverenz, Aufbau und Test eines Szintillationszählersystems zur Bestimmung des Strahluntergrundes am H1 Experiment sowie erste

Strahlstudien an HERA, Diploma thesis, University of Hamburg, 1991, unpublished.
[47] V. Korbel, Erste HERA-Strahluntergrundstudien in der H1 Wechselwirkungszone im November 1991, DESY preprint HERA 92-07, Hamburg, 1992, unpublished.
[48] K. Flamm, Messungen von Strahluntergrund bei HERA für den Betrieb von H1, H1 report FH1K-92-03, DESY, Hamburg, 1992, unpublished.
[49] H1 Collaboration, C. Berger et al., Technical proposal for the H1 detector, DESY report PRC 86-02, Hamburg, 1986, unpublished.
[50] H1 Calorimeter group, B. Andrieu et al., Nucl. Instr. and Meth. A 336 (1993) 460.
[51] H1 Calorimeter group, B. Andrieu et al., Nucl. Instr. and Meth. A 344 (1994) 492.
[52] J. Stier, Kalibration des H1 Flüssig-Argon Kalorimeters mit kosmischen Myonen, DESY FH1K-92-04, Diploma thesis, University of Hamburg, 1992, unpublished.
[53] R. Bernier et al., IEEE. Trans. Nucl. Sci. NS-34 (1988) 131.
[54] K. Djidi, Proc. 2nd Int. Conf. on Advanced Technology and Particle Physics, Como, 1990, eds. E. Borchi et al., Nucl. Phys. B (Proc. Suppl.) 23A (1991) 186.
[55] N. Huot, Estimation et Réjection de l'Empilement pour la Mesure des Fonctions de Structure par les Calorimètres de H1, Ph.D. thesis, University of Paris 7, 1992, unpublished.
[56] H. Abramowicz et al., Nucl. Instr. and Meth. 180 (1981) 429.
[57] H1 Collaboration, W. Braunschweig et al., Nucl. Instr. and Meth. A 265 (1988) 419.
[58] H1 Collaboration, W. Braunschweig et al., Nucl. Instr. and Meth. A 275 (1989) 246.
[59] H. Greif, Untersuchung zur kalorimetrischen Messung von Jeteigenschaften in hochenergetischen Elektron–Proton Speicherring – Experimenten, Ph.D. thesis, Technical University of München, 1990, unpublished.
[60] H1 Calorimeter group, H. Oberlack, Proc. 25th Int. Conf. on High Energy Physics, Singapore, (1990) Vol. 2, p. 1377.
[61] P. Loch, Kalibration des H1 Flüssig-Argon Kalorimeters unter Berücksichtigung der Gewichtungsmethode für Teilchen-Jets, H1 report FH1K-92-02, DESY, Hamburg (1992);
Ph.D. thesis, University of Hamburg, 1992, unpublished.
[62] H.P. Wellisch et al., MPI-PhE/94-03 (1994).
[63] W. Braunschweig et al., Results from a test of a Pb–Fe liquid argon calorimeter, DESY preprint 89-022, Hamburg (1989).
[64] H1 Calorimeter group, B. Andrieu et al., Nucl. Instr. and Meth. A 336 (1993) 499.
[65] H1 Calorimeter group, B. Andrieu et al., Nucl. Instr. and Meth. A 350 (1994) 57.
[66] F. Zomer, Energy Correction Procedure for Electrons in CB2–CB3 ϕ-crack region, H1 report 09/93-316, DESY, Hamburg, 1993, unpublished.
[67] M. Korn, Untersuchungen zur Messung der Energie von Elektronen und geladenen Pionen mit dem Flüssig Argon Kalorimeter des Detektors H1, Ph.D. thesis, University of Dortmund, 1994, unpublished.
[68] M. Hütte and M. Korn, Energy Correction Procedure for Electrons in FBE ϕ-crack region, H1 report 11/94-400, DESY, Hamburg, 1994, unpublished.
[69] H1 Collaboration, W. Braunschweig et al., Nucl. Instr. and Meth. A 270 (1988) 334.
[70] R. Grässler, Kalibration eines elektromagnetischen Kalorimetermoduls für den H1 Detektor, Diploma thesis, RWTH Aachen, 1991, unpublished.
[71] J.-F. Laporte, Diffusion Profondément Inélastique à HERA et Calibration Absolue de la Mesure en Energie d'un Electron dans le Calorimètre à Argon Liquide de l'Expérience H1, Ph.D. thesis, University of Paris-Sud, 1991, unpublished.
[72] K. Borras, Aufbau und Kalibration eines Flüssig-Argon Kalorimeters im H1 Detektor, Ph.D. thesis, University of Dortmund, 1992, unpublished.
[73] M. Flieser, Untersuchungen zur Energieauflösung eines Flüssig-Argon-Kalorimeters für Elektronen und Pionen im Energiebereich von 3.7–170 GeV, MPI-Phe/92-08, H1 report 07/92-231, DESY, Hamburg, 1992, unpublished;
Diploma thesis, Technical University of München, 1992, unpublished.
[74] S. Peters, Die parametrisierte Simulation elektromagnetischer Schauer, MPI-PhE/92-13, Ph.D. thesis, University of Hamburg, 1992, unpublished.
[75] P. Hartz, Kalibration eines Blei-Flüssigargon Kalorimeters mit Elektronen für das H1 Experiment, Ph.D. thesis, University of Dortmund, 1993, unpublished.
[76] R. Haydar, Test et Calibration du Calorimètre Hadronique de l'Expérience H1 à HERA, Ph.D. thesis, University of Paris-Sud, 1991, unpublished.
[77] J. Gayler, Proc. Workshop on Detector and Event Simulation, eds. K. Bos and B. van Eijk, NIKHEF-H report, Amsterdam (1991) p. 312.
[78] B. Delcourt et al., Comparison of pion calorimeter test data with simulation for CB2/CB3 period, H1 report 04/92-220, DESY, Hamburg, 1992, unpublished.
[79] M. Rudowicz, Hadronische Schauersimulation fuer den H1 Detektor, MPI-PhE/92-14, Ph.D. thesis, University of Hamburg, 1992, unpublished.
[80] H. Fesefeldt, Nucl. Instr. and Meth. A 263 (1988) 114.
[81] R. Brun et al. GEANT long write-up, CERN Program Library, W5103, 1989.
[82] H. Bergstein, Eichung des H1 Tail Catchers als stand-alone Kalorimeter und in der Kombination mit dem H1 Flüssig Argon Kalorimeter, Ph.D. thesis, RWTH Aachen, 1993, unpublished.
[83] H1 BEMC group, J. Ban et al., Nucl. Instr. and Meth. A 372 (1996) 399.
[84] Kyowa Gas Chemical ind. Co. Ltd., Nihonbashi, 3-8-2, Chuo-ku, Tokyo 103, Japan.
[85] C. Brune et al., BEMC Calibration in 1993, H1 report 04/94-352, DESY, Hamburg, 1994, unpublished.
[86] E. Fretwurst et al., Nucl. Instr. and Meth. A 288 (1990) 1.
[87] M. Eberle et al., Electromagnetic MC-simulations with EGS4 and GEANT – How to make them work for thin detectors, H1 report 05/89-113, DESY preprint 89-104, Hamburg (1989).
[88] M. Eberle et al., Test Experiment und Monte-Carlo-Simulationen für Silizium-Instrumentierte Kalorimeter, Annual report 1990/1991, I. Inst. Phys., University of Hamburg, 1991, unpublished;
M. Eberle, Ph.D. thesis, University of Hamburg, in preparation.
[89] I. Fedder, Untersuchungen an Silizium-instrumentierten Test-Kalorimetern für elektromagnetische und hadronische Schauer, Ph.D. thesis, University of Hamburg, 1991, unpublished.
[90] M. Ruffer, Implementierung des Silizium-instrumentierten PLUG-Kalorimeters in den H1-Detektor, Ph.D. thesis, University of Hamburg, 1992, unpublished.
[91] E. Panaro, M. Krüger and M. Seidel, Calibration of the H1 Plug calorimeter and comparison of data with Monte Carlo simulations, H1 report 09/95-455, DESY, Hamburg, 1995, unpublished.
[92] R. Wunstorf, Systematische Untersuchungen zur Strahlenresistenz von Silizium-Detektoren für die Verwendung in Hochenergiephysik-Experimenten, Ph.D. thesis, University of, Hamburg, 1992, unpublished; H1 report FH1K-92-01, DESY, Hamburg, 1992, unpublished.
[93] W. Hildesheim and M. Seidel, An investigation into the radiation damage of the silicon detectors of the H1 Plug calorimeter within the HERA environment, DESY preprint 95-139, Hamburg, 1995, unpublished.
[94] G. Ingelman, Proc. Workshop on Physics at HERA, Hamburg, 1991, eds. W. Buchmüller and G. Ingelman, DESY, Hamburg (1992), vol. III, p. 1366.
[95] J. Ebert, The H1 Tail Catcher hardware and software performance, H1 report 08/95-448, DESY, Hamburg, 1995, unpublished.
[96] F. Niebergall, Calibration and data correction for the TC calorimeter, H1 report 02/91-163, DESY, Hamburg, 1991, unpublished.

[97] H. Bergstein et al., Beam calibration of the H1 tail catcher at CERN, H1 report 10/91-197, DESY, Hamburg, 1991, unpublished.
[98] L. Büngener, Interkalibration der Türme des H1 Tailcatchers, Diploma thesis, University of Hamburg, 1992, unpublished.
[99] Luranyl: BASF, Ludwigshafen, Germany.
[100] G. Battistoni et al., Nucl. Instr. and Meth. 152 (1978) 423; ibid. 176 (1980) 297.
[101] F. Ferrarotto, R. Kotthaus and B. Stella, Study of alternative materials for streamer tubes, H1 report TR-406, DESY, Hamburg, 1987, unpublished.
[102] CAEN High Voltage System SY 127, Costruzioni Apparecchiature Elettroniche Nucleari S.p.A., I-55049 Viareggio.
[103] K. Geske, H. Riege and R. van Staa, The digital electronics of the H1 streamer tube detector, H1 report H1LSTEC 90-8, DESY, Hamburg, 1990, unpublished.
[104] I. Cronström et al., Nucl. Instr. and Meth. A 340 (1994) 304.
[105] Proc. Int. Conf. on Computing in High Energy Physics, Tsukuba, Japan, 1991, eds. Y. Watase and F. Abe (Universal Academy Press, 1991).